

行政院國家科學委員會專題研究計畫 成果報告

化學與光能轉換的基礎研究

計畫類別：個別型計畫

計畫編號：NSC93-2119-M-009-001-

執行期間：93年01月01日至93年12月31日

執行單位：國立交通大學應用化學系(所)

計畫主持人：林明璋

報告類型：完整報告

報告附件：出席國際會議研究心得報告及發表論文

處理方式：本計畫可公開查詢

中 華 民 國 94 年 3 月 18 日

中文摘要

國科會於 2004 年以「國科會講座」延聘美國 Emory 大學講座教授林明璋院士自美返台主持交通大學分子科學研究中心以致力發展最先進的研究計劃。除了在互益的基礎上，與台灣物理、化學方面的學者就相關聯的研究主題進行數個合作研究計劃之外，為將分子科學研究中心的研究發展維持在一定的水準上，近期內已提交以再生能源以及奈米粒子輔以超快電子動力學與電子在系統中轉換方面之生物化學研究為主題的三個大型研究計劃。這些以理論計算為輔的合作研究實驗包括：

- (1) 由王念夏教授與兩位研究生研製以 pump-probe 雷射來發射螢光的 NCN 與 NO 反應動力學實驗。
- (2) 由李遠鵬教授與一個博士生在清大進行並輔以 Emory 大學理論計算結果的氧原子與 CH_3OH 在巨烈衝擊波反應的動力學實驗。
- (3) 由李遠哲與原分所同仁進行 $\text{C}_6\text{H}_5\text{NO}$ 的光分裂動力學。
- (4) 建立一套低壓有機金屬化學蒸鍍設備與以研究 InN/TiO_2 奈米粒子薄膜系統中反覆轉換特性為主的飛秒與奈秒雷射探測系統。

截至目前為止，本計劃已有四篇論文在科學期刊上發表或即將出刊，除此之外，並有十篇在交通大學準備或撰寫的論文將會陸續以國科會贊助的名義在國際期刊上發表。

關鑑詞：NCN 與 NO 反應、 $\text{O}+\text{CH}_3\text{OH}$ 反應、 $\text{C}_6\text{H}_5\text{NO}$ 光分解、 InN/TiO_2 太陽能研究。

英文摘要

The 2004 visit of M. C. Lin from Emory University, supported by National Science Council for the full year, had been devoted to the development of a forefront research program for the Center for Interdisciplinary Molecular Science (CIMS) at National Chiao Tung University, and to studies of several collaborative research projects with chemical physicists in Taiwan on selected topics of mutual interest. For the development of a sustainable research program for CIMS in the near future, 3 major proposals have been submitted for the Center with focus on renewable energy research and on biochemical systems on nanoparticles aided by studies on the dynamics of fast electron and energy transfer in those systems. In the collaborative studies, experiments aided by theoretical simulations have been carried out on (1) the kinetics of NCN reaction with NO by pump-probe laser-induced fluorescence with N. S. Wang and two graduate students; (2) the kinetics of O-atom reaction with CH₃OH in shock waves with Y.-P. Lee and a PhD student at NTHU, aided by theoretical calculations carried out at Emory University; (3) the photo-fragmentation dynamics of C₆H₅NO with Y. T. Lee and coworkers at IAMS; and (4) the establishment of a low pressure organometallic chemical vapor deposition apparatus and femtosecond and nanosecond laser probing systems for forward and back electron transfer characterization in the InN/TiO₂ nanoparticle film systems. Four papers have been published or accepted for publication in SCI journals. In addition, 10 papers which were prepared or edited at NCTU by the PI have been credited to NSC for the support of the effort.

關鍵詞：CIMS's program、NCN+NO kinetics、O+CH₃OH kinetics、C₆H₅NO fragmentation dynamics、InN/TiO₂ deposition

一、前言：

The objectives of this project for the period Jan. 1 – Dec. 31, 2004 centered on: (1) Establishment of a forefront research program at the Center for Interdisciplinary Molecular Science (CIMS) with emphasis on studies of electron and energy transfer dynamics in nanoparticles and biological systems and (2) Collaboration with scientists in Taiwan on kinetics and dynamics of chemical reactions of interest to atmospheric chemistry, combustion and photo fragmentation dynamics, as well as the establishment of a research laboratory for preparation of InN/TiO₂ nanoparticle films for solar energy conversion applications.

CIMS, established officially at NCTU in July 2003, has now over 10 faculty members with a broad spectrum of research fields. The Center's major focus is placed on the applications of ultra-fast spectroscopy to study energy and electron transfer dynamics over a wide range of the spectrum (covering from the infrared to the UV). On account of the national need in renewable energy research to alleviate the acute shortage in Taiwan's energy resources, the Center's near-term research objectives will be placed on solar energy conversion and the catalytic studies of ethanol to H₂ conversion for fuel cell applications.

In the proposed collaborative research projects, 4 full papers have been completed and submitted for publications (2 published and 2 accepted for publication), with additional 10 papers credited to NSC for works carried out at Emory University but written or edited by the PI during the past year visiting NCTU.

二、報告內容：

(一) Establishment of research programs at the Center for Interdisciplinary Molecular Science (CIMS) in National Chiao Tung University

CIMS was officially established at NCTU in July 2003. It has now over 10 faculty members from the campus and neighboring research institutions such as NSRRC with a broad spectrum of research fields. The most recent addition was Prof. Yuan-Pern Lee who moved to NCTU to be University Distinguished Professor on August 1, 2004. The Center's major focus is placed on the applications of ultra-fast spectroscopy to study energy and electron transfer dynamics over a wide range of the spectrum (covering from the infrared to the UV). In order to train physical chemists with a broad range of expertise, fundamental gas phase spectroscopy and chemical kinetics with a solid training in quantum chemistry and statistical mechanics are essential. This area of research will be continually emphasized also.

On account of the national need in renewable energy research to alleviate the acute shortage in Taiwan's energy resources (we import as much as 98% of our energy supplies) the Center's research focus in the near future will be placed on solar energy conversion and the catalytic studies of H₂ conversion from ethanol, a truly "green fuel" which may be derived from sugar and other biomasses including celluloses with advanced fermentation processes, for H₂ fuel cell applications.

In the past year, three major proposals have been submitted from CIMS which, if funded, should strengthen our current interdisciplinary collaborative projects funded by NCTU in the areas of bio- and nano-materials research.

(二) Progress in collaborative studies

The proposed research milestones for Jan. – Dec. 2004 as put forth in the original proposal include:

- a. Kinetics of NCN reaction with NO studied by pump-probe LIF measurements with N. S. Wang and two PhD students at CIMS/NCTU to carry out experiment and theoretical calculations.
- b. Kinetics of O-atom reaction with CH₃OH in shock waves with Y.-P. Lee and a PhD student at NTHU, aided by theoretical calculations to be carried out at CIMS/NCTU.
- c. Photo-fragmentation study of C₆H₅NO with C.-K. Ni and Y. T. Lee at IAMS, aided by theoretical calculations to be carried out at CIMS/NCTU.
- d. Photoluminescence measurement for the bandgap and electron mobility of InN/TiO₂ nano-structures deposited at Emory using a femtosecond laser at CIMS /NCTU with E. W. G. Diau and a PhD student.

The progress in these collaborative research projects are briefly summarized below:

1. Atmospheric chemistry

a. NCN + NO kinetics

In collaboration with N.S. Wang's group at NCTU, the kinetics for the reaction of NO with the NCN radical, a key prompt NO precursor reaction intermediate in the new CH + N₂ mechanism put forth by Lin and coworkers,^[1,2] has been investigated. The rate constants for the reaction have been measured by laser photolysis/laser induced fluorescence technique in the temperature range 254 – 353 K in the presence of He (40 – 600 Torr) and N₂ (30 – 528 Torr) buffer gases. The NCN radical was produced from the photodissociation of NCN₃ at 193 nm and monitored with a dye laser at 329.01 nm. The reaction was found to be strongly positive-pressure dependent with negative-temperature dependence, as was reported previously. The experimental data could be reasonably accounted for by dual channel RRKM calculations based on the predicted potential energy surface using the G2M method (see Figs. 1 and 2). The reaction is predicted to occur via weak intermediates, cis- and trans-NCNNO, in the ²A'' state which crosses with the ²A' state containing more stable cis- and trans-NCNNO isomers. The high barriers for the fragmentation of these isomers and their trapping in the ²A' state by collisional stabilization give rise to the observed positive pressure dependence and negative temperature effect. The predicted energy barrier for the fragmentation of the cis-NCNNO (²A') to CN + N₂O also allows us to quantitatively account for the rate constant previously measured for the reverse process CN + N₂O → NCN + NO.^[3]

b. Kinetics of the S + O₂ reaction

In collaboration with Y-P Lee's group, we have investigated the kinetics of the S + O₂ reaction, which has not been well characterized to date. The rate coefficients of the reaction at 50 Torr Ar pressure in the temperature range 298–878 K were determined with the laser photolysis technique. S atoms were generated by photolysis of OCS with a KrF excimer laser at 248 nm; their concentration was monitored via resonance fluorescence excited by atomic emission of S produced from microwave-discharged SO₂. Our measurements show that $k(298\text{ K}) = (1.92 \pm 0.29) \times 10^{-12} \text{ cm}^3 \text{ molecule}^{-1} \text{ s}^{-1}$, in satisfactory agreement with previous reports. New data determined for 505–878 K show non-Arrhenius behavior; combining our results with data reported at high temperatures, we derive an expression $k(T) = (9.02 \pm 0.27) \times 10^{-19} T^{2.11 \pm 0.15} \exp[(730 \pm 120)/T] \text{ cm}^3 \text{ molecule}^{-1} \text{ s}^{-1}$ for $298 \leq T/\text{K} \leq 3460$. Theoretical calculations at the G2M(RCC2) level, using geometries optimized with the B3LYP/6-311+G(3df) method, yield energies of transition states and

products relative to those of the reactants (see Fig. 3). Rate coefficients predicted with multichannel RRKM calculations agree satisfactorily with experimental observations (see Fig. 4); the reaction channel via $\text{SOO}({}^1\text{A}')$ dominates at $T < 500$ K, whereas channels involving formation of $\text{SOO}({}^3\text{A}'')$ followed by isomerization to SO_2 before dissociation, and formation of $\text{SOO}({}^1\text{A}'')$ followed by direct dissociation, become important at high temperatures, accounting for the observed rapid increase in rate coefficient.

Fig. 1. The potential energy surface of the $\text{NCN} + \text{NO}$ system

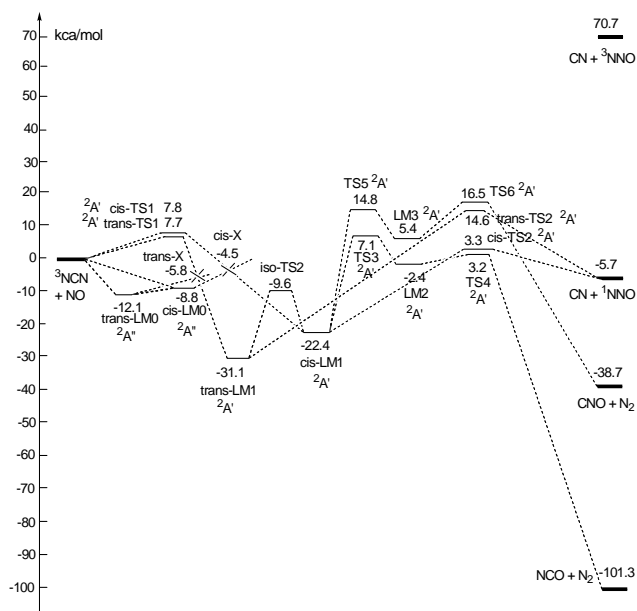


Fig. 2. Comparison of the predicted and measured rate constant for $\text{NCN} + \text{NO}$

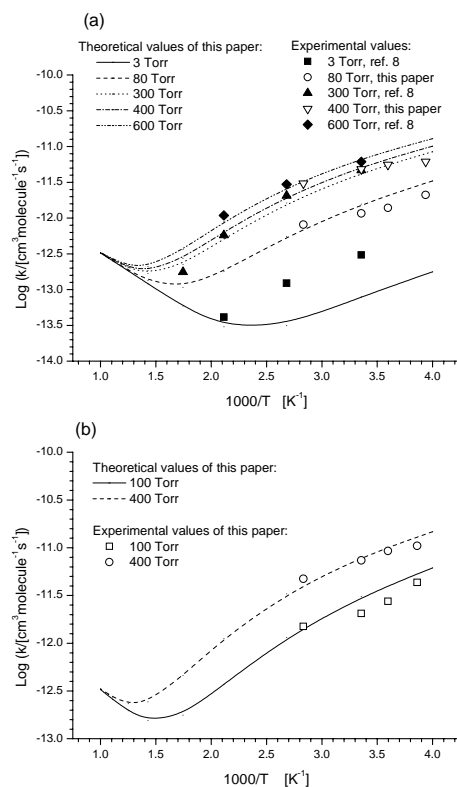
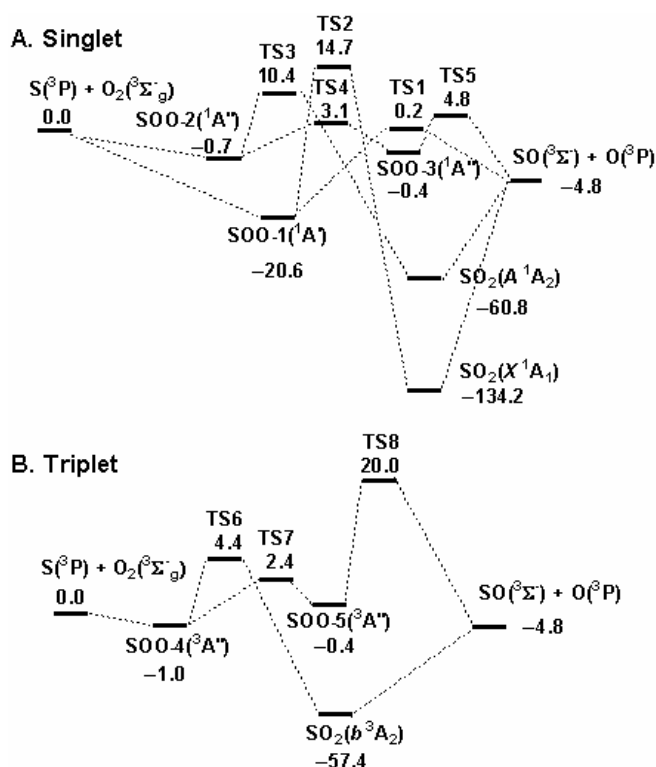


Fig. 3. Potential energy diagrams of the S-O₂ system



2. Combustion reactions—High temperature kinetics of the O + CH₃OH reaction.

CH₃OH is an important alternate fuel to gasoline. In collaboration with Y-P Lee's group, we have studied the kinetics of the O + CH₃OH reaction, which is not available under the combustion conditions. The rate coefficients of the reaction in the temperature range 835–1777 K were determined using a diaphragmless shock tube. O atoms were generated by photolysis of SO₂ with a KrF excimer laser at 248 nm or an ArF excimer laser at 193 nm; their concentrations were monitored via atomic resonance absorption excited by emission from a microwave-discharged mixture of O₂ and He. Rate coefficients determined for the temperature range can be represented by the Arrhenius equation: $k(T) = (2.29 \pm 0.18) \times 10^{-10} \exp [-(4210 \pm 100)/T] \text{ cm}^3 \text{ molecule}^{-1} \text{ s}^{-1}$; unless otherwise noted, all listed errors represent one standard deviation in fitting. Combination of these and previous data at lower temperature shows a non-Arrhenius behavior described as the three-parameter equation $k(T) = (2.74 \pm 0.07) \times 10^{-18} T^{2.25 \pm 0.13} \exp [-(1500 \pm 90)/T] \text{ cm}^3 \text{ molecule}^{-1} \text{ s}^{-1}$. Theoretical calculations at the B3LYP/6-311+G(3df, 2p) level locate three transition states (see Fig. 5). Based on the energies computed with CCSD(T)/6-311+G(3df, 2p)//B3LYP/6-311+G(3df, 2p), rate coefficients predicted with canonical variational transition state theory with small curvature tunneling corrections agree satisfactorily with experimental observations (see Fig. 6). The branching ratios of two accessible reaction channels forming CH₂OH + OH (1a) and CH₃O + OH (1b) are predicted to vary strongly with temperature. At 300 K, reaction (1a) dominates, whereas reaction (1b) becomes more important than reaction (1a) above 1700 K.

Fig. 4. Comparison of the predicted and measured rate constant for the S + O₂ reaction

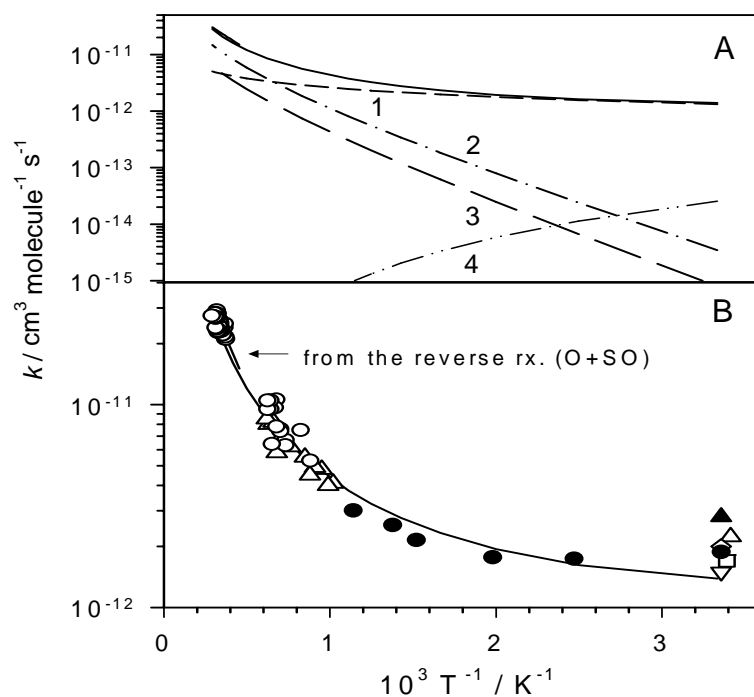


Fig. 5. Energy diagram of the O-CH₃OH system

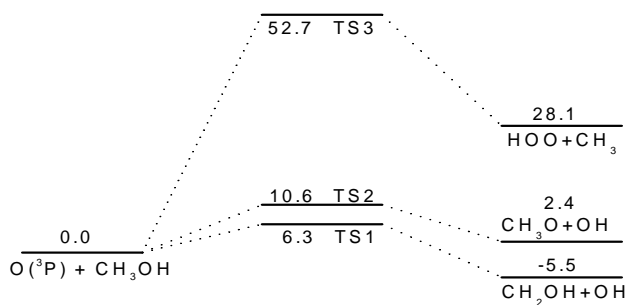
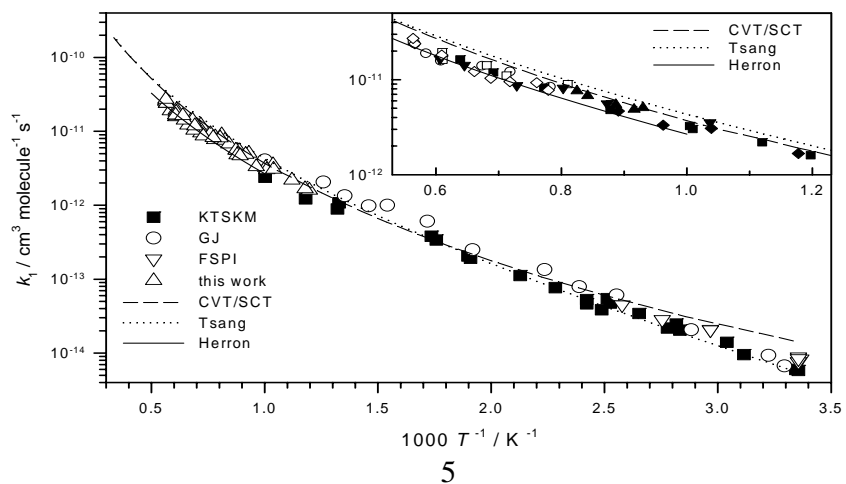


Fig. 6. Comparison of the predicted with measured rate constant for O + CH₃OH reaction



3. Photofragmentation of C₆H₅NO

Nitrosobenzene is a key photolytical source of the phenyl radical. In collaboration with Y. T. Lee, C. K. Ni et al. at IAMS, the dynamics of the photofragmentation of C₆H₅NO has been studied using multimass ion imaging techniques. Photodissociation at 248 nm shows that there is only one dissociation channel, i.e., C₆H₅NO → C₆H₅ + NO, regardless of the fact that the other channel C₆H₅NO → C₆H₄ + HNO is energetically accessible in agreement with theoretically predicted result (see Fig. 7). Photodissociation at 193 nm also shows the same dissociation channel. However, about 10% of the C₆H₅ radicals produced at this wavelength further decomposed into benzyne and H atom, and the dissociation rates of phenyl radical as a function of internal energies were measured. The averaged photofragment translational energies released from the dissociation of nitrosobenzene at 193 nm and 248 nm are 10.2 and 6.9 kcal/mol, respectively, and fragment distributions are almost isotropic at both wavelengths (see Fig. 8) In addition, the thermal rate constant for dissociation of C₆H₅NO has been computed and compared with experimental data; the agreement between theory and experiment is excellent, confirming the most recently reported unusually high A-factor (see Fig. 9).^[4]

Fig. 7. Energy diagram of the C₆H₅NO system

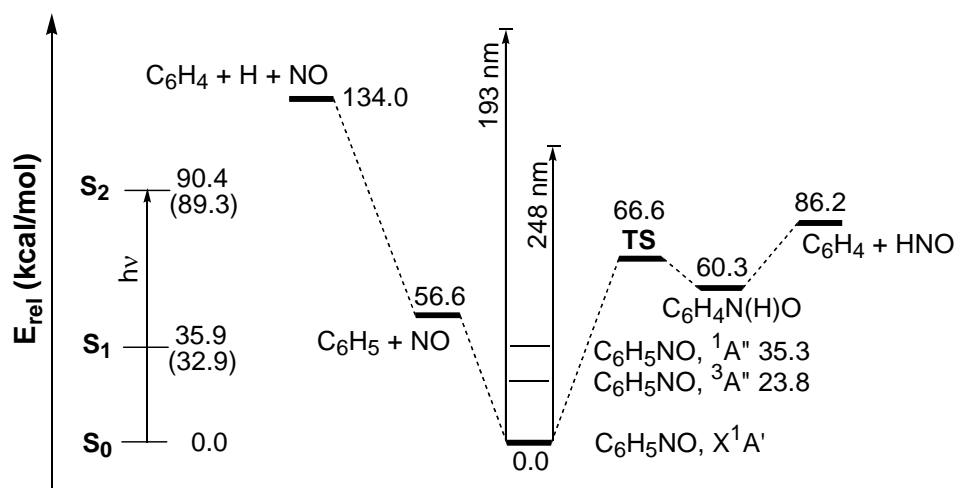


Fig. 8. (a) Photofragment ion image intensity profiles of $m/e = 77$ from two different photolysis laser polarizations at 248 nm. Thick and thin lines represent the polarization of UV laser perpendicular and parallel to the VUV laser beam, respectively. (b) Anisotropy parameter β as a function of fragment translational energy.

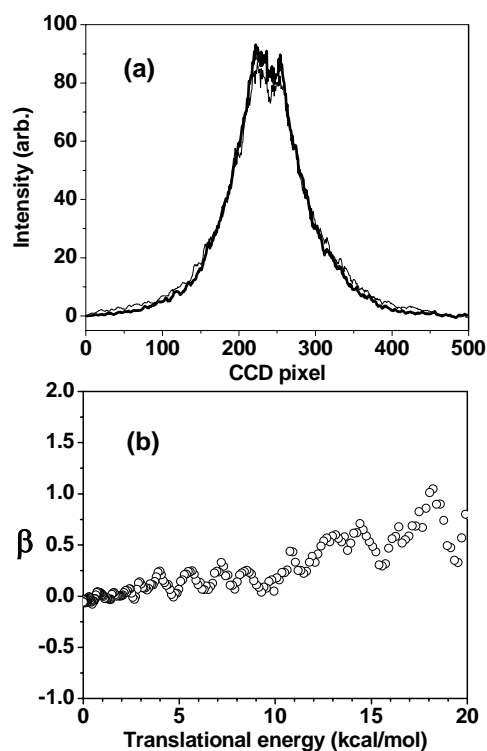
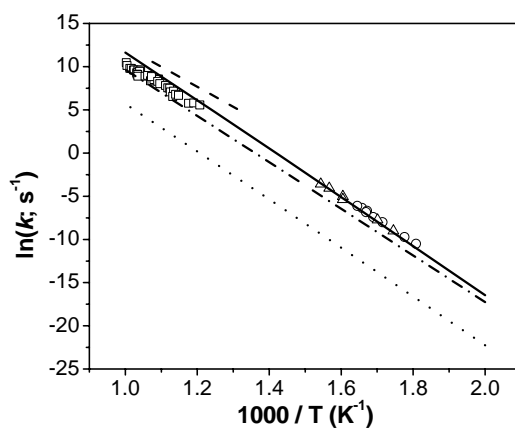


Fig.9. Experimental and predicted thermal rate constants for the dissociation of C_6H_5NO at the high-pressure limit. Points are experimental data; solid, dash-dotted, and dotted lines correspond to the prediction for the states of X^1A' , $^1A''$, and $^3A''$, respectively. Their sum gives $k^\infty = 1.52 \times 10^{17} \exp[-55200/RT] s^{-1}$



4. Deposition and characterization of InN/TiO₂ nanoparticle films

The PI's group at Emory University has recently demonstrated that the chemically robust InN film can be directly deposited on TiO₂ nanoparticles by OMCVD (organometallic chemical vapor deposition) with very good physical adhesion.^[5] The films exhibit a very broad UV/vis absorption covering 400 – 800 nm region of the spectrum. In

order to explore the possibility of developing the InN/TiO₂ system for solar energy conversion devices, efforts have been made through a series of experiments at CIMS, NCTU. In the following summary, we report the progress made in these efforts.

a. Construction of a small OMCVD system and a photoluminescence apparatus

A new OMCVD system has been constructed at CIMS for a new series of InN thin-film deposition on TiO₂ nanoparticles with emphasis on the improvement of chemical connectivity between InN and TiO₂ for enhancement of electron transfer rates. The interface materials or functional groups may include electron withdrawing or electron providing elements such as B or P, respectively. Other potential materials include semi-conductive metal oxide quantum dots and nanoparticles. The schematic diagram of the OMCVD system is shown in Fig. 10. In addition, a photoluminescence measurement apparatus has been assembled for thin-film characterization as shown in Fig. 11. These systems will be used in our continuing exploration of the new generation of cheap solar energy conversion devices.

Fig. 10. Sample holder and CVD chamber of CIMS's OMCVD apparatus

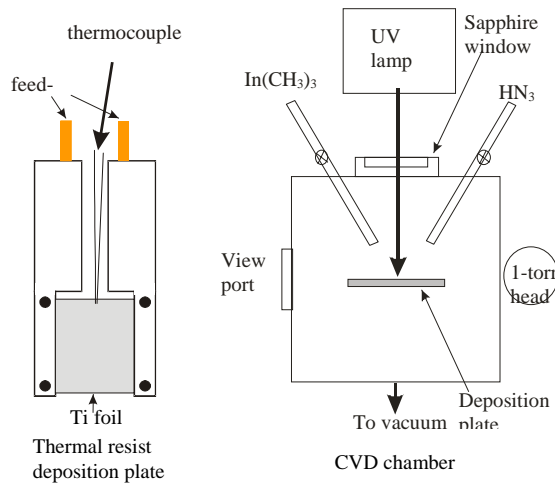
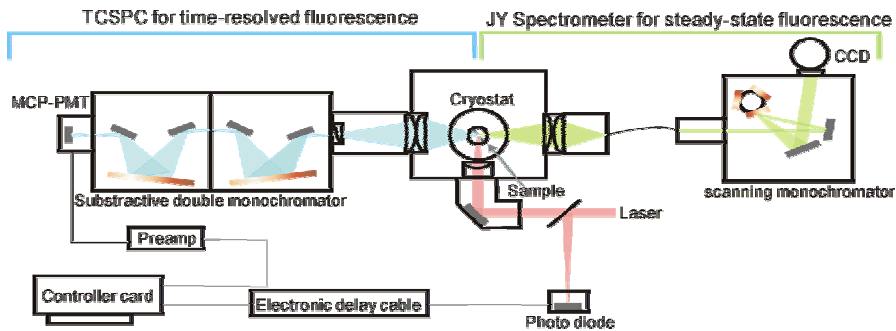


Fig. 11. Photoluminescence apparatus for solid surface characterization at 4 K or 77 K.



b. Establishment of a femtosecond pump-probe system for electron and energy transfer dynamics studies

In this year, we have successfully built a new fs pump probe system, and the experimental set up is shown in Fig 12. Briefly, a fs mode-locked Ti-Sapphire oscillator provides optical pump and probe light source in the near IR (700-1000 nm) region. For the

purpose of studying solar energy systems, the laser wavelength can be further extended to the visible region (525-665 nm) via coupling the oscillator with an OPO (Optical Parametric Oscillator) device. The laser beam was divided into two parts via a beam splitter (BS1) and used as pump (~80%) and probe (~20%). A computer-controlled optical delay line was set in pump path to vary the delay time between pump and probe pulses. A small portion of the pump beam was reflected by BS2 and used as the reference of the auto-balanced detector. The major part of the pump beam was modulated by a mechanical chopper (~1 kHz) and then focused onto the thin-film sample; the average power of pump beam was ~400 mW at 800 nm. For the probe beam, the power was attenuated to ~1/10 (40 mW) of the pump beam by a neutral-density filter, and focused onto the sample overlapping with pump beam at exactly the same position. The reflected probe beam was collected as the signal in auto-balanced detector and then the signal was sent to lock-in amplifier controlled by a computer.

In the present stage, we have successfully measured the ultrafast carrier dynamics of the reference compound (GaAs) by the constructed fs pump-probe system. Fig 13 shows our initial test data for the transient signal representing the photo-reflectance change of GaAs as a function of time at 800 nm.

Fig. 12. Experimental set-up of fs pump-probe system

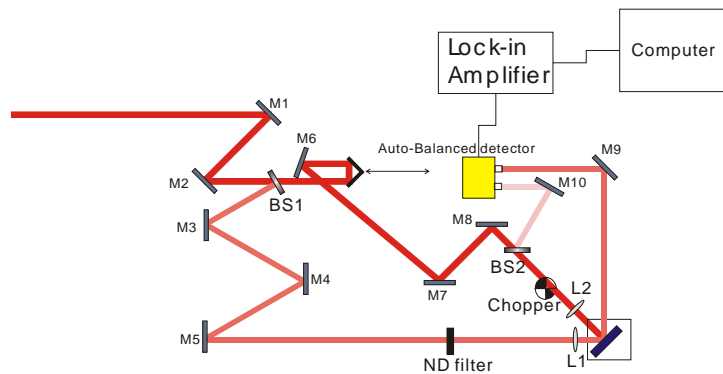
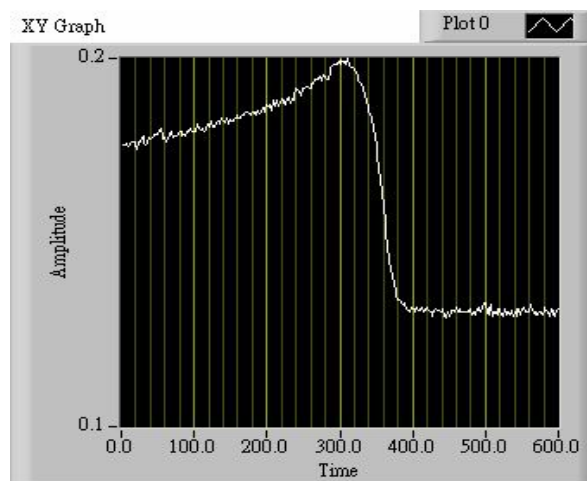


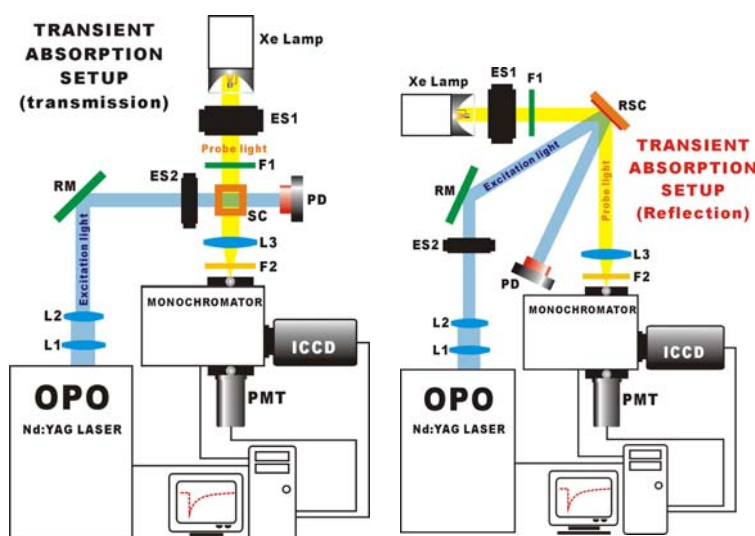
Fig. 13. Initial test data for the transient signal representing the photo-reflectance change of GaAs as a function of time at 800 nm



c. Establishment of nanosecond transient absorption system

A nanosecond transient absorption spectrometer has been reconstructed for the kinetics measurements in the condensed phase. The arrangement of the setup is summarized as follows (see fig. 14). The excitation source generates excited-state species under investigation; a ns Nd:YAG/OPO system (funded by the NSC project) was used as the light source to cover a broad excitation wavelength range (210-2300 nm). A pulsed Xe lamp (1-5 μ s duration), synchronously triggered by the excitation laser, was used for measurements of the time-dependent absorption spectra of the sample; the transient absorption spectra at a certain delay time can be recorded by the gated intensified charged-coupled devices (ICCD). Alternatively, the time-evolution profile of the sample at a certain absorption wavelength can be obtained by a sensitive photomultiplier tube (PMT). The current experimental setup is suitable for samples dissolved in solution (a transmission design shown in the left-hand side); in the future the system can be modified to a reflection design (shown in the right-hand side of the figure) for the purpose of electron back transfer kinetics measurements on samples such as InN functionalized on nanocrystalline TiO₂ thin films.

Fig. 14. Nanosecond transient absorption setup for electron back transfer kinetic studies.



RM: reflective mirror; **L:** lens; **ES:** electronic shutter; **F:** filter; **SC:** sample cell; **RSC:** reflective sample cell; **PD:** photodiode sensor.

References:

- [1] L. V. Moskaleva, W. S. Xia and M. C. Lin, "The CH + N₂ Reaction over the Ground Electronic Doublet Potential Energy Surface: A Detailed Transition State Search", *Chem. Phys. Lett.*, 331, 269-77 (2000).
- [2] L. V. Moskaleva and M. C. Lin, "The Spin-Conserved Reaction CH + N₂ → H + NCN: A Major Pathway to Prompt NO Studied by Quantum/Statistical Theory Calculations and Kinetic Modeling of Rate Constant", *Proc. Combust. Intst.*, 28 (Part II), 2393-401 (2000).
- [3] N. S. Wang, D. L. Yang, M. C. Lin and C. F. Melius, "Kinetics of CN Reactions with N₂O and CO₂", *Int. J. Chem. Kinet.*, 23, 151 (1991).
- [4] J. Park, I. V. Dyakov, A. M. Mebel, and M. C. Lin, "Experimental and Theoretical Studies of the Unimolecular Decomposition of Nitrosobenzene: High-Pressure Rate Constants and the C-N Bond Strength", *J. Phys. Chem. A*, 101, 6043 (1997).
- [5] Jenghan Wang and M. C. Lin, "Low-Pressure Organometallic Chemical Vapor Deposition of Indium Nitride on Titanium Oxide Nanoparticles", *ChemPhysChem*, 5, 1615-18 (2004).

三、計畫成果自評：

All of the proposed collaborative projects described above had been successfully carried out with 2 papers already published in the world's top chemical physics journals and 2 more accepted for publications. In addition, 10 papers written or edited by the PI during the visit at NCTU have been credited to NSC. They are listed below:

Papers published or accepted for publications:

- a. Cheng-Ming Tzeng, Y. M. Choi, Cheng-Liang Huang, Chi-Kung Ni, Yuan T. Lee, and M. C. Lin, "Photodissociation of nitrosobenzene and decomposition of phenyl radical", *J. Phys. Chem., A*, **108**, 7928-35, (2004).
- b. Chih-Wei Lu and Yu-Jong Wu, Yuan-Pern Lee, R. S. Zhu and M. C. Lin, "Experimental and Theoretical Investigations of Rate Coefficients of the Reaction $S(^3P) + O_2$ in the Temperature range 298–878 K", *J. Chem. Phys.*, **121**, 8271-78 (2004).
- c. Chih-Liang Huang, Shiang Yang Tseng, Tzu Yi Wang, N. S. Wang, Z. F. Xu and M. C. Lin, "Reaction Mechanism and Kinetics of the $NCN + NO$ Reaction: Comparison of Theory and Experiment", *J. Chem. Phys.*, in press.
- d. Chih-Wei Lu and Shen-Long Chou, Yuan-Pern Lee, Shucheng Xu, Z. F. Xu and M. C. Lin, "Experimental and Theoretical Studies of Rate Coefficients for the Reaction $O(^3P) + CH_3OH$ at High Temperatures", *J. Chem. Phys.*, in press.

Other publications prepared at NCTU during 2004 with acknowledgments to NSC:

1. R. S. Zhu and M. C. Lin, "Rate Constants of $ClO + NO$ for the Forward and Reverse Processes", *ChemPhysChem*, **5**, 1864-70 (2004).
2. R. S. Zhu and M. C. Lin, "Ab Initio Study of the Oxidation of NCN by O_2 ", *Int. J. Chem. Kinet.*, in press.
3. J. H. Wang and M. C. Lin, "Adsorption and Reaction of N_2H_4 on $Si(100)-2 \times 1$: A Computational Study with Single- and Double-Dimer Cluster Models", *Surf. Sci.*, in press.
4. Shucheng Xu and M. C. Lin, "A Computational Study on the Kinetics and Mechanism for the Unimolecular Decomposition of $C_6H_5NO_2$ and the Related $C_6H_5 + NO_2$ and $C_6H_5O + NO$ Reactions", *J. Phys. Chem., A*, in press.
5. R. S. Zhu and M. C. Lin, "Ab initio Studies of ClO_x Reactions: XI. Prediction of the Rate Constants of $ClO + NO_2$ for the Forward and Reverse Processes", *ChemPhysChem*, submitted.
6. Jenghan Wang, M. C. Lin and Ying-Chieh Sun, "Reactions of Hydrazoic Acid on TiO_2 Nanoparticles: An Experimental and Computational Study", *J. Phys. Chem, B*, in press.
7. Y. M. Choi and M. C. Lin, "Kinetics and Mechanisms for Reactions of HNO with CH_3 and C_6H_5 Studied by Quantum-chemical and Statistical-theory Calculations", *Int. J. Chem. Kinet.*, in press.
8. Jenghan Wang and M. C. Lin, "Reactions of Trimethyl Indium on TiO_2 Nanoparticles: An Experimental and Computational Study", *J. Phys. Chem, B*, submitted..
9. R. S. Zhu, J. Park and M. C. Lin, "Ab initio Kinetic Study of the Low Energy Paths of the $HO + C_2H_4$ Reaction", *Chem. Phys. Lett.*, submitted.
10. Z. F. Xu, H.-C. Hsu and M. C. Lin, "Ab Initio Kinetics of the HCO Reaction with NO : Abstraction vs. Association/Elimination Mechanism", *J. Chem. Phys.*, Submitted

四、附錄：

Photodissociation of nitrosobenzene and decomposition of phenyl radical

Cheng-Ming Tzeng,¹ Y. M. Choi,² Cheng-Liang Huang,^{1,3} Chi-Kung Ni^{1*},

Yuan T. Lee,^{1,4} and M. C. Lin,^{2,5*}

1. Institute of Atomic and Molecular Sciences, Academia Sinica, P. O. Box: 23-166, Taipei, Taiwan

2. Department of Chemistry, Emory University, Atlanta, Georgia 30322 USA

3. Present address: Department of Applied Chemistry, National Chiayi University, Chiayi, Taiwan

4. Department of Chemistry, National Taiwan University, Taipei, 106, Taiwan

5. Center for Interdisciplinary Molecular Science, National Chiao Tung University, Hsinchu 300, Taiwan.

* Corresponding authors: ckni@po.iam.s.sinica.edu.tw; chemmcl@emory.edu

Abstract

Photodissociation of nitrosobenzene in a molecular beam has been studied using multimass ion imaging techniques. Photodissociation at 248 nm shows that there is only one dissociation channel, i.e., $C_6H_5NO \rightarrow C_6H_5 + NO$, regardless of the fact that the other channel $C_6H_5NO \rightarrow C_6H_4 + HNO$ is energetically accessible in agreement with theoretically predicted result. Photodissociation at 193 nm also shows the same dissociation channel. However, about 10% of the C_6H_5 radicals produced at this wavelength further decomposed into benzyne and H atom, and the dissociation rates of phenyl radical as a function of internal energies were measured. The averaged photofragment translational energies released from the dissociation of nitrosobenzene at 193 nm and 248 nm are 10.2 and 6.9 kcal/mol, respectively, and fragment distributions are almost isotropic at both wavelengths. In addition, the thermal rate constant for dissociation of C_6H_5NO has been computed and compared with experimental data; the agreement between theory and experiment is excellent, confirming the most recently reported unusually high A-factor ($>10^{17} s^{-1}$).

I. Introduction

Nitrosobenzene has been popularly employed photolytically as the precursor of phenyl radicals in many kinetic and spectroscopic studies because of its large extinction coefficient in the UV region.¹⁻⁸ The molecule has a large energy gap between the S_1 and S_2 states.^{9,10} Hence, the possibility of fluorescence from the S_2 state has been discussed.¹¹ However, no fluorescence has been observed.¹²⁻¹⁴ The existence of a fast decay channel in the S_2 state is therefore expected. Indeed, it was found that the dissociation of nitrosobenzene in argon matrices at 12 K is very efficient upon irradiation of UV photons.¹⁵

The dynamics of photodissociation of nitrosobenzene in the gas phase have been studied recently.¹⁶⁻²² However, conclusions are very different from these studies. Dick and coworkers measured the absorption spectrum of the $S_0 - S_2$ transition of the ultracold nitrosobenzene in a supersonic jet.¹⁷ A lifetime of the S_2 state determined directly by the homogeneous linewidth of the absorption spectrum was found to be 60 ± 3 fs. They also measured the alignment, velocity distribution, and populations of the rotational and vibrational states of the NO fragments via laser induced fluorescence and ion imaging technique at various UV wavelengths.¹⁸⁻²⁰ Fragments have an isotropic velocity distribution and no alignment was observed. In addition, the NO rotational population has a statistical distribution and only 10 % of the NO fragments are produced in vibrational excited states. They concluded that the primarily populated S_n -state ($n \geq$

2) decays rapidly through internal conversion to the S_1 or S_0 state, and the dissociation occurs through a statistical mechanism on the potential surface of the lower state on a timescale much slower than rotation of the parent molecule. On the other hand, Han and coworkers also have studied the photodissociation of nitrosobenzene at 266 nm recently.^{21,22} The anisotropy parameter $\beta = -0.64$ was found from the time-of-flight spectra of NO and C_6H_5 photofragments. Their laser induced fluorescence study also demonstrated that more than 60 % of the NO fragments are populated in the vibrational excited state and the NO fragment rotational temperature is much higher than that measured by Dick et al.

In all existing studies, including those kinetic and spectroscopic papers cited above, only one dissociation channel, $C_6H_5NO \rightarrow C_6H_5 + NO$, has been assumed and/or detected in the photodissociation of nitrosobenzene in the UV region, despite the fact that the $C_6H_4 + HNO$ product channel is accessible at 248 nm while the $C_6H_4 + H + NO$ product channel becomes energetically accessible at 193 nm.

In this report, photodissociation of nitrosobenzene at 193 nm and 248 nm were studied using multimass ion imaging techniques. Particular attention has been focused on the search of the other possible dissociation channel and the fragment anisotropy measurement. In addition, the decomposition of the phenyl radical produced from the photodissociation reaction and the

thermal decomposition of nitrosobenzene were also studied; the data will be discussed in reference to the *ab initio* MO and statistical theory results.

II. Experimental and Computational Methods

Experimental setup. The experimental techniques have been described in detail in our previous reports on other aromatic molecules,²³⁻²⁶ and only a brief description is given here. Nitrosobenzene vapor was formed by flowing ultrapure He at pressures of 500 Torr through a reservoir filled with liquid sample at 293 K. The nitrobenzene/He mixture was then expanded through a 500 μm pulsed nozzle to form the molecular beam. Molecules in the molecular beam were photodissociated by an UV laser pulse. Due to the recoil velocity and center-of-mass velocity, the fragments were expanded to a larger sphere on their flight to the ionization region, and then ionized by a VUV laser pulse. The distance and time delay between the VUV laser pulse and the UV photolysis laser pulse were set such that the VUV laser beam passed through the center-of-mass of the dissociation products, and generated a line segment of photofragment ions by photoionization. The length of the segment was proportional to the fragment recoil velocity in the center-of-mass frame multiplied by the delay time between the photolysis and the ionization laser pulses. To separate the different masses within the ion segment, a pulsed electric

field was used to extract the ions into a mass spectrometer after ionization. While the mass analysis was being executed in the mass spectrometer, the length of each fragment ion segment continued to expand in the original direction according to its recoil velocity. At the exit port of the mass spectrometer, a two-dimensional ion detector was used to detect the ion positions and intensity distribution. In this two-dimensional detector, one direction was the recoil velocity axis and the other was the mass axis. The schematic diagram of the experimental set up is shown in Fig.1.

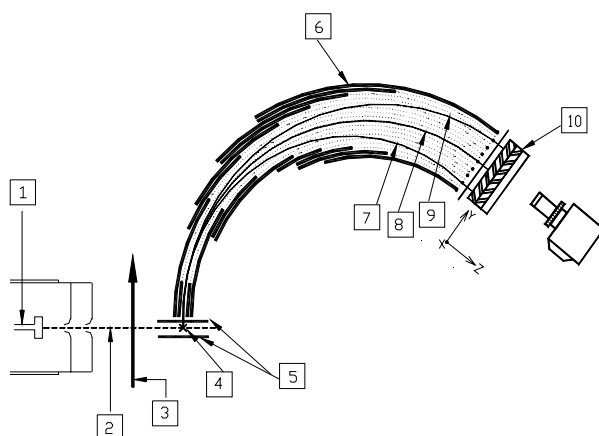


Fig. 1. Schematic diagram of the multimass ion imaging detection system. (1) nozzle; (2) molecular beam; (3) photolysis laser beam; (4) VUV laser beam, which is perpendicular to the plane of the paper; (5) ion extraction plates; (6) energy analyzer; (7), (8) and (9) simulation ion trajectories of $m/e = 16, 14, 12$; (10) Two-dimensional detector, where Y-axis is mass axis, and X-axis (perpendicular to the plane of the paper) is the velocity axis.

Computational method. The hybrid density functional B3LYP²⁷⁻²⁹ with three split valence basis sets, 6-31G(d), 6-31+G(d), and 6-31G(2df,p), has been applied to optimize the geometries of the reactant, intermediate, transition state, and products with tight convergence criterion. All the stationary points were identified by the number of imaginary frequencies (NIMG) with NIMG = 0 for stable species and NIMG = 1 for transition states, as well as by the normal mode analysis. To continue to study the unimolecular reaction of C₆H₅NO based on our earlier work³⁰ at the G2M(rec, MP2) and G2M(RCC, MP2) levels,³¹ in this report we also performed quantum-chemical calculations with the G2M(RCC, MP2) scheme. A series of single-point energy calculations for the G2M (RCC, MP2) composite scheme using the geometries and zero-point energy (ZPE) corrections from the B3LYP/6-31G(d) and B3LYP/6-31+G(d) levels of theory have been carried out to obtain more reliable information on energetics for the potential energy surface (PES) and the rate constant prediction by the following scheme:

$$E_0[\text{G2M}] = \text{RCCSD(T)/6-311G(d,p)} + \text{MP2/6-311+G(3df,2p)} - \text{MP2/6-311G(d,p)} \\ + \Delta\text{HLC} + \text{ZPE}$$

The empirical ΔHLC is given by $-5.3n_\beta - 0.19n_\alpha$ in mhartree, where n_α and n_β are the numbers of α and β valence electrons, respectively. Some of the energies have also been calculated by the G3SX composite method³² with the geometries optimized at the B3LYP/6-31G(2df,p) level.

Since the method does not include any empirical correction, this method has been proposed to apply for the system whose number of spins is changed like the present system. Therefore, we can compare the two composite schemes for the issue on the spin change. In addition, time-dependent density functional theory (TD-DFT)³³⁻³⁵ at the B3LYP/6-31+G(d) level has been used to calculate the vertical excitation energies and oscillator strengths for the S₁ and S₂ states of C₆H₅NO. The electronic structure calculations were carried out with the Gaussian 98³⁶ and MOLPRO 98³⁷ programs.

III. Results and Discussions

(a) Dissociation of nitrosobenzene at 248 nm

Ions of $m/e = 30$, 77 and 78 were the only two fragments we observed from the photodissociation of nitrosobenzene at this wavelength. $m/e = 78$ is the corresponding ¹³C isotope of fragment $m/e = 77$. Photofragment ion images are shown in Figs. 2(a) and 2(b). Photolysis laser intensity in the region between 2.5 ~ 30 mJ/cm² were used. They showed the same shapes of image. It suggests that one-photon absorption is the dominant process in this laser intensity region. Since there was no HNO and C₆H₄ detected, we can conclude that there is only one dissociation channel at 248 nm, i.e., C₆H₅NO → C₆H₅ + NO, in spite of the fact that the other channel C₆H₅NO → C₆H₄ + HNO is also energetically accessible (*vide infra*). As a result,

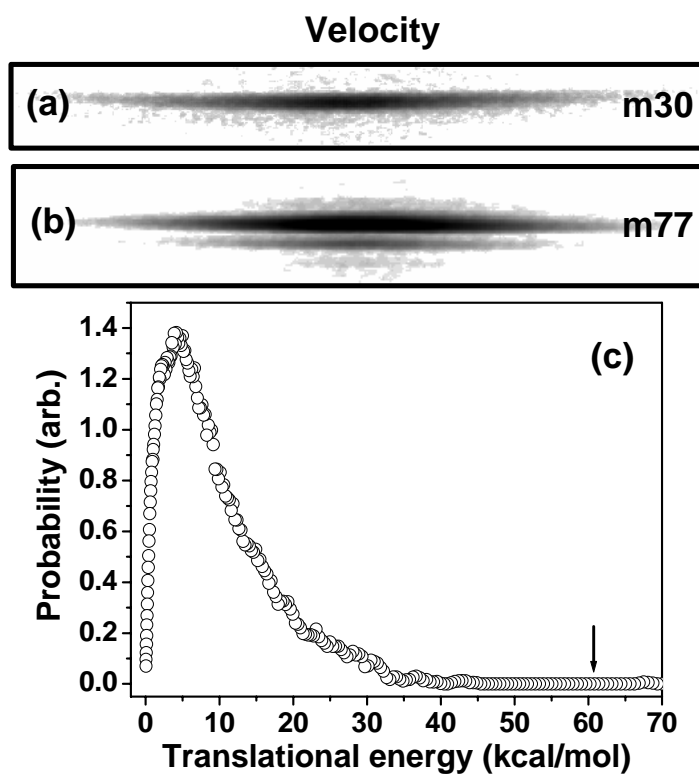


Fig. 2. Photofragment ion image of (a) $m/e = 30$, (b) $m/e = 77$ and 78 , and (c) photofragment translational energy distribution at 248 nm. Arrow indicates the maximum available energy.

nitrosobenzene is a “clean” precursor to generate phenyl radical at this wavelength.

The photofragment translational energy distribution obtained from the images is illustrated in Fig. 2(c). It shows that the probability monotonically decreases with the increasing translational energy. The average released translational energy is about 6.9 kcal/mol, and it is about 11 % of the total available energy. Compared to the average translational energy measured

in previous studies, our value is much smaller than 29 % of the fragment translational spectroscopy measurement at photolysis wavelength 266 nm,²² and it is very close to 7.3 % and 6 ~ 11 % of velocity map ion imaging measurement at 290.5 and 225.96 nm, respectively.²⁰

The C₆H₅ photofragment ion image profiles at two different photolysis laser polarizations are presented at Fig. 3(a). The shapes and the intensities of the profiles at the polarization directions parallel and perpendicular to the VUV probe laser beam are very close to each other. The anisotropy parameter β for the fragments with different translational energy is illustrated in Fig. 3(b). At low translational energy region where most of the fragments are produced, the values of β are very close to zero, indicating the isotropic distribution of the fragments. At high translational energy region, the values of β fluctuate between 0 and 1. The poor S/N ratios are due to the small amount of high translational energy fragments produced at high translational energy region. We can conclude that most of the fragments are isotropically distributed. If there is any anisotropic distribution, it must be from the fragments with large translational energy. However, the amount of those fragments is very small, and the value of β is positive.

The anisotropy parameter β we measured at 248 nm is very close to the value of 0.05 from the single line measurement at 225.96 nm.²⁰ It is also very close to the value of 0.03 ~ -0.05

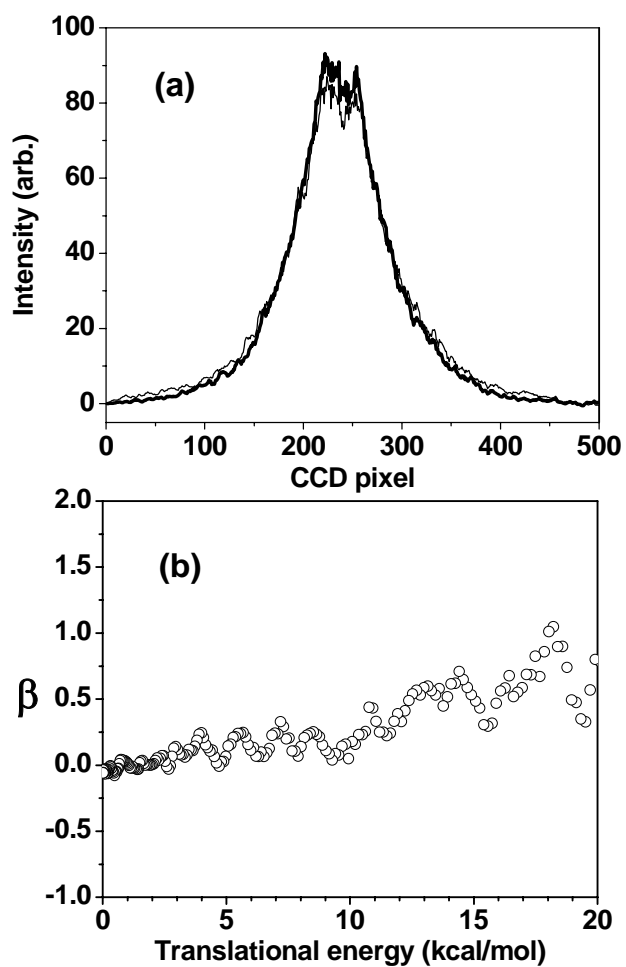


Fig. 3. (a) Photofragment ion image intensity profiles of $m/e = 77$ from two different photolysis laser polarizations at 248 nm. Thick and thin lines represent the polarization of UV laser perpendicular and parallel to the VUV laser beam, respectively. (b) Anisotropy parameter β as a function of fragment translational energy.

from the measurement of several rotational states of NO $v = 0$ at photolysis wavelength 290.5 nm.²⁰ However, it is very different from the value of -0.64 obtained from the photofragment translational energy measurement at 266 nm.²² Both the translational energy distribution and anisotropy parameter β measurement suggest that our results are similar to that of Dick's, but they are different from that of Han's.

(b) Dissociation of nitrosobenzene at 193 nm

Fragment ions of $m/e = 30, 76, 77$ and 78 were observed from the photodissociation of C_6H_5NO at 193 nm. Photolysis laser intensity in the region between $0.2 \sim 1.7 \text{ mJ/cm}^2$ were used, and all of these fragment intensities showed linear dependence on the laser intensity. The images are shown in Fig. 4. As the delay time between pump and probe laser pulses increased, the relative intensity between $m/e = 76$ and 77 also changed, as shown in Fig. 5. Since no HNO fragment was detected, fragments of $m/e = 76$ must result from the slow dissociation of the energetic fragments $m/e = 77$. Consequently, we can conclude that there is still only one dissociation channel of nitrosobenzene at 193 nm, even though the photon energy is much higher than the dissociation barrier of $C_6H_5NO \rightarrow C_6H_4 + HNO$. This observation is consistent with the significantly smaller decay rate predicted for this product channel as will be presented later. The photofragment translational energy distribution obtained at this wavelength is shown in Fig. 4(c). The average energy released is 10.2 kcal/mol, which is slightly larger than that at 248 nm.

The anisotropy parameter β at 193 nm was found to be very similar to that at 248 nm. The

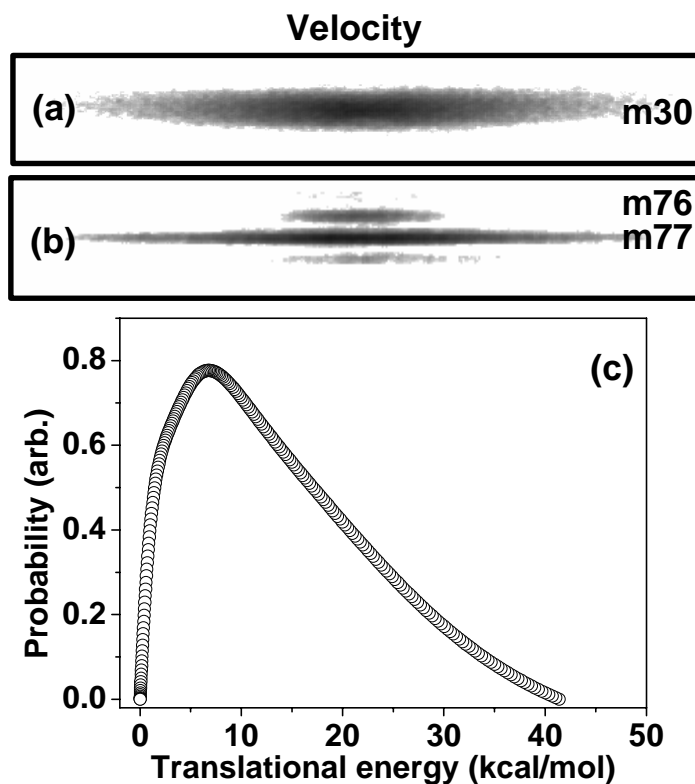


Fig. 4. Photofragment ion image of (a) $m/e = 30$, (b) $m/e = 76, 77$ and 78 , and (c) photofragment translational energy distribution at 193 nm.

C_6H_5 photofragment ion image intensity profiles at two different photolysis laser polarizations was found to be very close to each other, as presented in Fig. 6(a). The values of β as a function of translational energy are shown in Fig. 6(b). It suggests that most of the fragments are isotropically distributed, and only a small amount of fragments with large translational energy have a positive value of β . The dissociation mechanism at 193 nm must be similar to that at 248 nm.

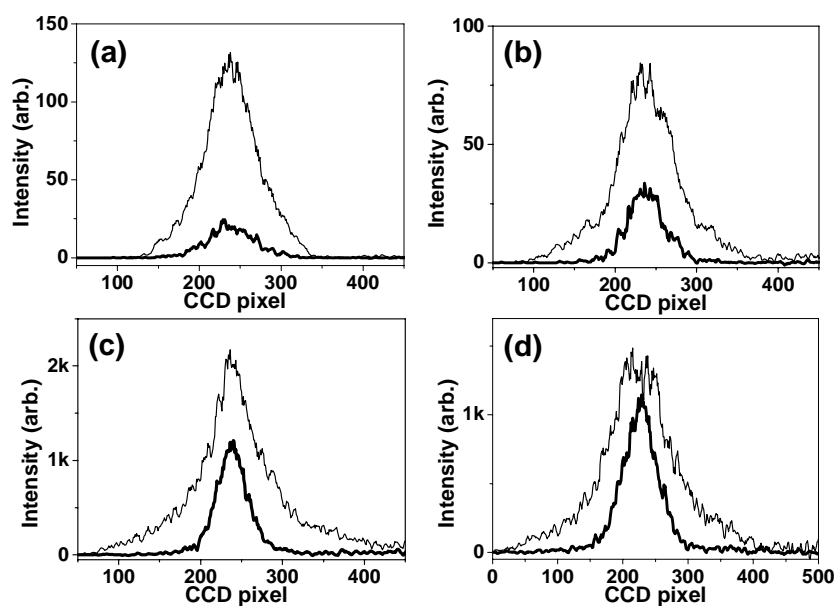


Fig. 5. Fragment ion image intensity profiles at various delay times. The thin solid line and thick solid line represent $m/e=77$ and 76 , respectively. (a) $t = 5 \mu\text{s}$, (b) $t = 9 \mu\text{s}$, (c) $t = 15 \mu\text{s}$, (d) $t = 18 \mu\text{s}$.

(c) Decomposition of phenyl radical

The phenyl radical plays a very important role in the combustion of small aromatic hydrocarbons.³⁸⁻⁴⁰ There has been considerable interest in its reactions with combustion species as well as its decomposition kinetics and mechanism. The *ab initio* calculation of a previous study⁴¹ showed that the decomposition of phenyl radical producing benzyne + H was

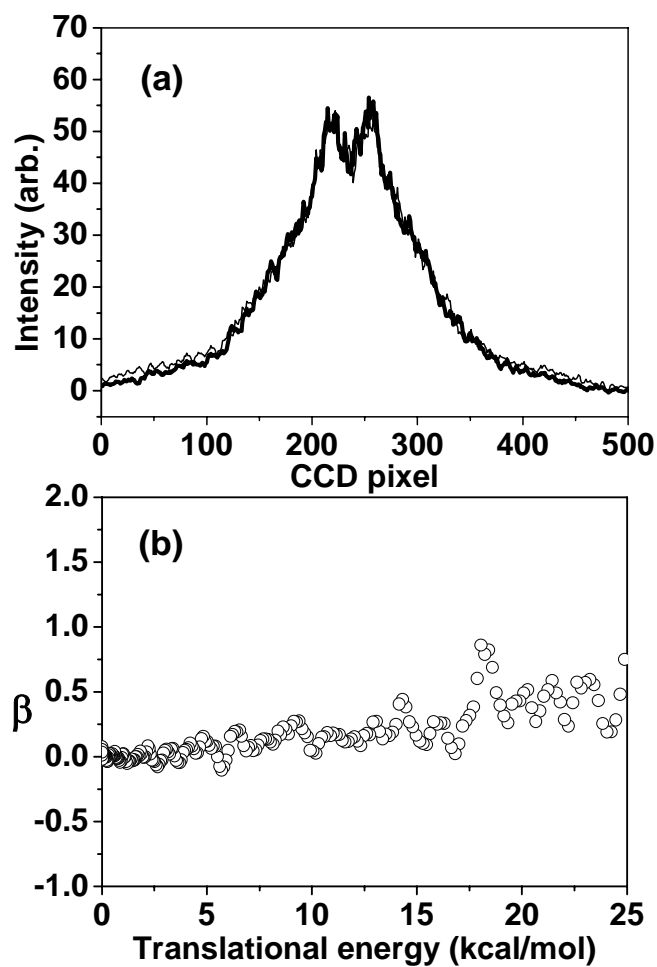


Fig. 6. (a) Photofragment ion image intensity profiles of $m/e = 77$ from two different photolysis laser polarizations at 193 nm. Thick and thin lines represent the polarization of UV laser perpendicular and parallel to the VUV laser beam, respectively. (b) Anisotropy parameter β as a function of fragment translational energy.

endothermic by 76.0 kcal/mol, and the reaction was reported to occur without a distinct transition state based on geometry optimization with the B3LYP method. This loose structure, also confirmed by MP2 and CCSD optimizations with the 6-31+G(d,p) basis set, however, over-estimated the high-temperature thermal decomposition rate constant determined by Braun-Unkoff et al,⁴² as was also shown by Wang and co-workers.⁴³ The new optimization carried out in this work with G96LYP/6-31+G(d,p) method located a low energy transition state. A G2M calculation based on this structure gives the barrier for the decomposition reaction at 79.4 kcal/mole above C₆H₅. For phenyl radicals produced from the photodissociation of nitrosobenzene at 193 nm, the maximum internal energy for phenyl radical is 93.8 kcal/mol. The decomposition into benzyne + H therefore is energetically allowed, as shown in Fig. 7.

The decomposition of phenyl radical into benzyne and H atom can be clearly seen from the image intensity changes of $m/e = 77$ and 76 at various delay times, as shown in Fig. 5. The central part of the fragment images in the velocity axis corresponds to small translational energy released, i.e., most of the available energy is distributed in the fragments' internal degrees of freedom. For the phenyl radicals located at the central part of the image, they contain a lot of internal energy and quickly decompose into benzyne and H atom. Since the mass ratio between benzyne and H atom is large and the available energy for the decomposition process is small, benzyne produced from this part of phenyl radicals is still located at the same position in the

velocity axis. The fast decomposition of this part of phenyl radicals can be seen from the fast rise of the central part of the image $m/e = 76$ at short delay time. On the other hand, phenyl radicals located on both sides contain less internal energy, and they have slow decomposition rates. The corresponding benzyne only appears at long delay time images. For the phenyl radicals positioned at both ends of the image in velocity axis, the translational energy released is large

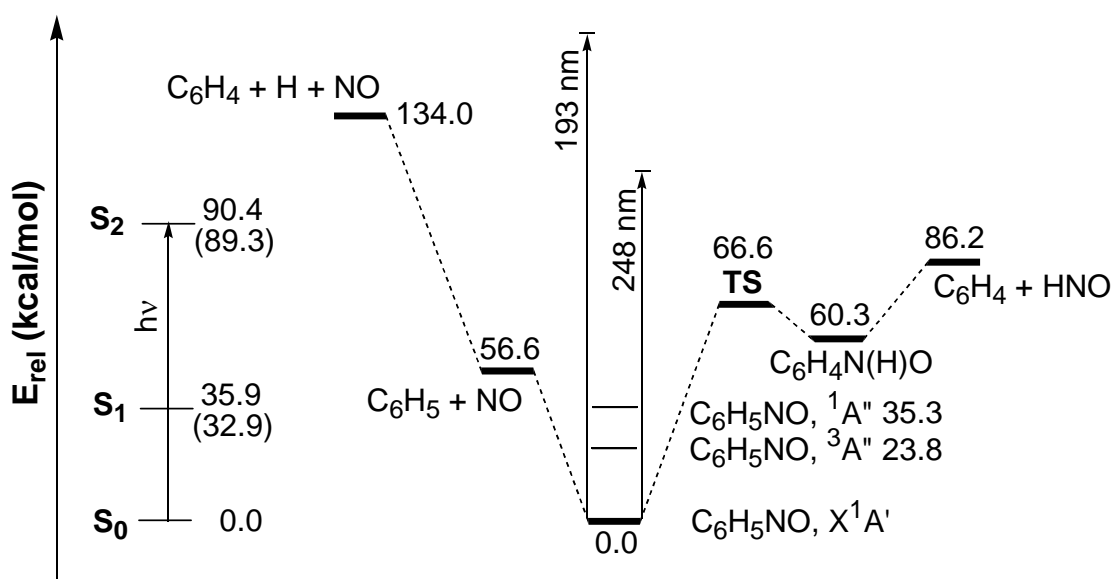


Fig. 7. Energy level scheme from the TD-DFT calculations at the B3LYP/6-31+G(d) level and schematic energy diagram for the isomerization and dissociation reactions of C_6H_5NO calculated at the G2M(RCC, MP2)//B3LYP/6-31+G(d) method in kcal/mol. Note that the energy of the $^1A''$ state, 35.3 kcal/mol, includes ZPE-correction.. The energy levels in parentheses are from ref 18.

and the energy left in the internal degrees of freedom is too small for the radical to be further dissociated into benzyne and H atom. They remain as phenyl radicals and no analogous benzyne is produced. Therefore, the length of the image $m/e = 76$ is shorter than that of $m/e = 77$ even at very long delay time.

The decomposition rate of phenyl radical as a function of internal energies can be obtained from the image intensity changes of each part of the image along the fragment velocity axis at various delay times. The internal energy of phenyl radical can be calculated from the following equation.

$$E(\text{int})_{\text{phenyl}} = h\nu - D_0 - E(\text{tran}) - E(\text{int})_{\text{NO}}$$

The photon energy $h\nu$ is 148 kcal/mol, the dissociation energy D_0 is 54 kcal/mol,³⁰ and the amount of translational energy released, $E(\text{tran})$, can be calculated directly using the fragment velocity obtained from the image. The only uncertainty in this equation is the internal energy of fragment NO. However, a proper estimation of the NO fragment internal energy could be made according to the previous studies and our measurement. Previous studies showed that the rotational and vibrational state distributions of NO fragments are statistical, and most of the energy is located in phenyl radical vibrational degrees of freedom. For example, the average vibrational energy of NO fragment is only 1.3 % of the total available energy at photolysis laser

wavelength 255 nm, and the rotational energies of both phenyl radical and NO are only 0.2 % and 3.7 %, respectively due to the transition state geometry. For nitrosobenzene photodissociation at 193 nm, both the value of anisotropy parameter β and the translational energy distribution suggest that dissociation mechanism is similar to that at 255 nm, i.e., the dissociation occurs after internal conversion to the lower electronic state. Energy must be redistributed among various vibrational degrees of freedom before dissociation occurs and the energy distribution is statistical. Therefore, we estimated that about 95 % of the available energy (total available energy after the subtraction of translational energy) is distributed in phenyl radical vibrational degrees of freedom.

For a given internal energy, the decomposition of phenyl radical into benzyne and H atom can be described by the equation $m_{77}(T_1) = \exp(-kT_1)$ and the growth of the corresponding benzyne can be described by $m_{76}(T_1) = 1 - \exp(-kT_1)$. $m_{77}(T)$ is the phenyl radical concentration for a given internal energy at delay time T . $m_{76}(T)$ is the benzyne concentration produced from the corresponding phenyl radical. k is the dissociation rate of phenyl radical. The ion intensity of $m/e = 77$ and 76 thus can be described by the following equations

$$I_{77}(T_1) = A(1 - \gamma)\exp(-kT_1) \quad (1)$$

$$I_{76}(T_1) = B[1 - \exp(-kT_1)] + A\gamma\exp(-kT_1) \quad (2)$$

A and B are the ionization cross sections of fragment mass 77 and 76, respectively. γ is the branching ratio of benzyne produced from the dissociative ionization of phenyl radical, described by the following reaction.



The dissociation rate can be calculated from the ion intensity ratios of fragment $m/e = 77$ and 76 at two different delay times using the following equation.

$$\frac{\frac{I_{m76}(T_1)}{I_{m77}(T_1)}}{\frac{I_{m76}(T_2)}{I_{m77}(T_2)}} = \frac{\frac{B(1-e^{-kT_1}) + A\gamma e^{-kT_1}}{A(1-\gamma)e^{-kT_1}}}{\frac{B(1-e^{-kT_2}) + A\gamma e^{-kT_2}}{A(1-\gamma)e^{-kT_2}}} = \frac{\frac{B}{A(1-\gamma)}(e^{kT_1} - 1) + \frac{\gamma}{1-\gamma}}{\frac{B}{A(1-\gamma)}(e^{kT_2} - 1) + \frac{\gamma}{1-\gamma}} \quad (4)$$

At short delay time when no benzyne is produced from the decomposition of phenyl radical, ion intensity ratio between I_{76} and I_{77} is close to the value of $\gamma/(1-\gamma)$. The upper limit of $\gamma/(1-\gamma)$ was obtained from the image at the available shortest delay time (5 μs), and final result of the decomposition rate k was calculated from the numerical solution of equation (4). The phenyl radical dissociation rates as a function of internal energy obtained from this equation are shown in Fig. 8. It shows that if the translational energy released in the photodissociation of nitrosobenzene is less than 1 kcal/mol, the decomposition rate of corresponding phenyl radical is in the region between $10^5 - 10^4 \text{ s}^{-1}$. However, if the translational energy release is more than 2 kcal/mol, the decomposition rate is too slow ($<10^4 \text{ s}^{-1}$) to be measured in our apparatus. The

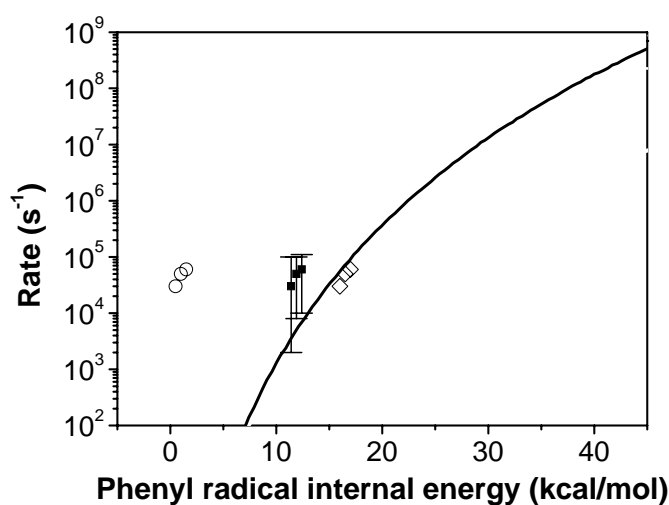


Fig. 8. Phenyl radical dissociation rate as a function of internal energy. Open circles, solid squares, and open diamonds represent the experimental values assuming 18 %, 5 % and 0 % of the available energy (93 kcal/mol) distributed in NO internal degrees of freedom. Solid line is the prediction at the G2M(RCC, MP2)//G96LYP/6-31+G(d) level in this work.

comparison of absolute ion image intensities of $m/e = 77$ between short delay time and long delay time indicate that about 10 % of phenyl radicals decompose into benzyne and H atom within the time scale ($<25 \mu\text{s}$) of our experiment. Compared to the decomposition rate obtained from G2M(RCC, MP2)//G96LYP/6-31+G(d) *ab initio* MO and statistical-theory calculations, the agreement between theory and experiment is satisfactory.

(d) Theoretical prediction of $\text{C}_6\text{H}_5\text{NO}$ decomposition rates

PES of the system. As described in the preceding section, the potential energy surface of the

C_6H_5NO system has been calculated with the G2M method³¹ based on the geometry optimized at the B3LYP/6-31+G(d,p) level of theory. The optimized structures of the reactant, transition state and intermediate are presented in Fig. 9. All the geometries of the C_6H_5NO (S_0, X^1A'), C_6H_5NO ($T_1, ^3A''$), and C_6H_5NO ($S_1, ^1A''$) are planar with C_s symmetry. The equilibrium C-N bond lengths of T_1 and S_1 states are shorter than that of the S_0 state as shown in Fig. 9. The predicted energetics and potential energy diagram for the formation of products accessible to 193 nm photon energy are presented in Table 1 and Fig. 7, respectively. At the G2M level, the 4-centered transition state leading to $C_6H_4 + HNO$ was predicted to locate at 67 kcal/mol above

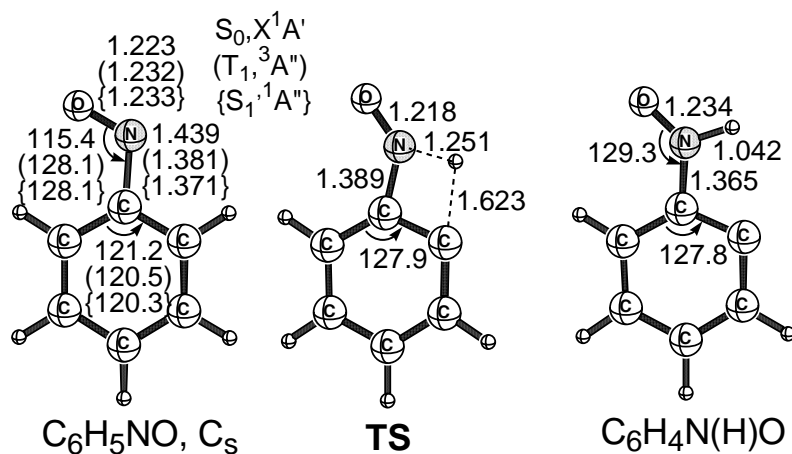


Fig. 9. Optimized structures of the reactant, transition state, and intermediate at the B3LYP/6-31+G(d) level of theory.

Table 1. Relative energies^a for the isomerization and decomposition reactions of C₆H₅NO.

species or reaction	B3LYP/ 6-31G(d)	G2M ^b	B3LYP/ 6-31+G(d)	G2M ^c	B3LYP/ 6-31G(2df,p)	G3SX ^d
C ₆ H ₅ NO	0.0	0.0	0.0	0.0	0.0	0.0
C ₆ H ₅ + NO	53.3	56.5	52.2	56.6	53.0	55.6
TS	66.1	66.7	65.6	66.6	63.3	66.0
C ₆ H ₄ N(H)O	60.5	60.2	57.8	60.3	58.4	59.6
C ₆ H ₄ + HNO	96.2	86.2	93.2	86.2	94.8	86.3
C ₆ H ₄ + H + NO	140.4	134.0	138.4	134.0	140.2	134.1

a. Relative energies are ZPE-corrected in kcal/mol.

b, c, and d. Based on the optimized geometries calculated at B3LYP/6-31G(d), B3LYP/6-31+G(d), and B3LYP/6-31G(2df,p), respectively.

C₆H₅NO, about 19 kcal/mol below the dissociated products. This suggests that a stable molecular complex must exist between C₆H₅NO and C₆H₄ + HNO. A detailed IRC calculation indeed confirms the presence of a benzyne-HNO complex, C₆H₄N(H)O, lying 60 kcal/mol above C₆H₅NO (see Fig. 9 for its structure). Further decomposition of the C₆H₄N(H)O complex was found to take place without a well-defined intrinsic barrier, similar to the fragmentation of C₆H₅NO to C₆H₅ and NO.

As shown in Table 1, the energetics predicted by both G2M and G3SX agree very closely. The latter, which does not include “high-level corrections”, is believed to be more reliable for applications to reactions with spin changes. In Table 2, the result of our TD-DFT calculations at the B3LYP/6-31+G(d) level for the S₁ and S₂ states confirms the energy gap between them, 54.5 kcal/mol, which compares closely with the experimental value, 56.4 kcal/mol.¹⁸

Table 2. Vertical energies in kcal/mol and oscillator strengths (f) in parenthesis for C_6H_5NO with estimated by TD-DFT at the B3LYP/6-31+(d) level.

state	sym	B3LYP/6-31+G(d)		experimental ^a
S ₁	1A''	35.9	(0.0003)	32.9
S ₂	1A'	90.4	(0.0183)	89.3

a. from ref 18.

Decomposition of photo-excited C_6H_5NO . Assuming that the internal conversion is fast comparing with fragmentation lifetimes, we can predict the fragmentation rates of C_6H_5NO following the excitation at 248 and 193 nm on the basis of the RRKM theory. As both product channels giving NO and HNO occur barrierlessly, the energy-dependent specific constants (k_E) were evaluated with the flexible transition state approach⁴⁴⁻⁴⁷ using the Variflex code.⁴⁸ The minimum energy paths (MEP) representing the dissociation processes were approximated with the Varshni potential,⁴⁹ $V(r) = D_e \{-a \exp[-b(R^2 - R_0^2)]\} - D_e$, where R is the reaction coordinate, R_0 is the equilibrium value of R , $a = R_0/R$, and D_e is the bond energy excluding the zero-point energy correction. Along the reaction coordinate, we stretched the bond length of C-N with the step size of 0.2 Å along the path from the equilibrium value to 5 Å. Each geometry was fully optimized at the B3LYP/6-31+G(d) level of theory and its energy was then scaled by the G2M(RCC, MP2) value for the Varshni potential. The approximated bond energy and b for the ground state with ¹A' are 60.4 kcal/mol and 0.522 Å⁻², respectively, using $R_0 = 1.439$ Å. Similar

calculations for the dissociation of $C_6H_4N(H)O$, C_6H_5NO ($T_1, {}^3A''$) and C_6H_5NO ($S_1, {}^1A''$) gave rise to $De = 30.3, 36.0, \text{ and } 20.0 \text{ kcal/mol}$; $b = 0.863, 0.834, \text{ and } 0.991 \text{ \AA}^{-2}$; $R_0 = 1.365, 1.381 \text{ and } 1.371 \text{ \AA}$, respectively.

Table 3. Decay rate of C_6H_5NO via different pathways.

Pathway	248 nm	193 nm
$C_6H_5NO \rightarrow C_6H_5 + NO$	2.5×10^{10}	3.2×10^{10}
$C_6H_5NO \rightarrow C_6H_4 + HNO^a$	1.0×10^4	1.3×10^7
$C_6H_5NO \rightarrow C_6H_4N(H)O$	2.9×10^5	1.8×10^7

a. The rate constant for $C_6H_5NO \rightarrow VTS \rightarrow C_6H_4 + HNO$ with VTS as the limiting step.

Using the molecular parameters given above, the specific rate constants for the dissociation of C_6H_5NO at 248 and 193 nm (approximately 115 and 148 kcal/mol, respectively) provide the lifetimes of the excited molecule along various pathways as summarized in Table 3. The lifetimes of C_6H_5NO are predicted to about 40 ps following the excitation at 248 nm and 33 ps at 193 nm producing exclusively $C_6H_5 + NO$ as was observed experimentally. The formation of HNO, slower by 10^5 at 248 nm and 10^3 at 193 nm, is experimentally undetectable. As the formation of HNO occurs via both the tight 4-centered TS1 and the variatioanl TS near the dissociation threshold, with the latter being slightly slower due to its higher energy (see Table 3), we have examined the effect of multiple reflections between the two TS's; the effect was found to be negligible because of the high photon energies. The predicted lifetimes are much longer

than that derived from the linewidth measurement suggesting that internal conversion is considerably faster than the fragmentation process.

Thermal decomposition rate constant. The high-pressure, first-order rate constant for the decomposition of C₆H₅NO producing C₆H₅ + NO, $k^\infty = (1.42 \pm 0.13) \times 10^{17} \exp[-(55060 \pm 1080)/RT] \text{ s}^{-1}$,³⁰ is seen to have an unusually large A-factor. The extrapolated rate constants in the temperature range of 800 - 1000K using the equation lies between the result of Horn and coworkers⁴⁸ (after high-pressure-limit correction by the RRKM theory) and that of Choo et al.⁴⁹ determined by the very-low-pressure pyrolysis method. Theoretically, the rate constant can be computed with the Varshni potential evaluated for the 3 MEP's producing NO. The thermal unimolecular dissociation rate constant defined by the rate equation,

$$d[\text{C}_6\text{H}_5]/dt = k^\infty [\text{C}_6\text{H}_5\text{NO}]_0 = \sum k_i^\infty X_i = k_X^\infty [X] + k_A^\infty [A] + k_B^\infty [B] \quad (5)$$

where [C₆H₅NO]₀, [X], [A] and [B] are, respectively, the initial concentration of nitrosobenzene entirely at its ground electronic state and those at the ground electronic, ³A" and ¹A" states under thermal equilibrium, and the k_i^∞ are the first-order rate constants for the dissociation from these states. Assuming K_A and K_B to be the equilibrium constants for X ↔ A and X ↔ B, respectively, equation (5) leads to the total unimolecular rate constant,

$$k^\infty = (k_X^\infty + k_A^\infty K_A + k_B^\infty K_B) / (1 + K_A + K_B) \quad (6)$$

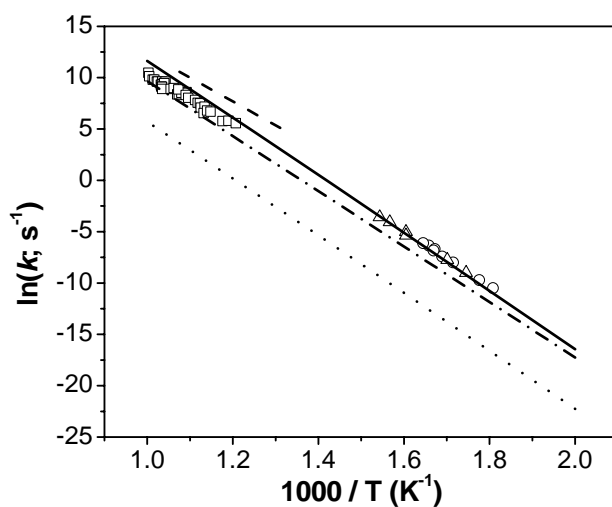


Fig. 10. Experimental and predicted thermal rate constants for the dissociation of C_6H_5NO at the high-pressure limit.. (\square) is from ref 50, (Δ) with NO added and (\circ) without NO added are from ref 30, and dashed line is from ref 51. Solid, dash-dotted, and dotted lines correspond to the prediction for the states of X^1A' , $^1A''$, and $^3A''$, respectively. Their sum gives $k^\infty = 1.52 \times 10^{17} \exp[-55200/RT] s^{-1}$

The predicted individual rate constants presented in Fig. 10 gave $k^\infty = 1.52 \times 10^{17} \exp[-55200/RT] s^{-1}$, which is in excellent agreement with the result obtained by Park et al.³⁰, $k^\infty = (1.42 \pm 0.13) \times 10^{17} \exp[-(55060 \pm 1080)/RT] s^{-1}$, confirming the unusually high A-factor. Notably, the result presented in Fig 10 indicates that the contributions from both T_1 and S_1 states are insignificant in the present system. For the decomposition of SO_2 at high temperatures in shock waves, we

have recently shown that contributions from 3 excited states to its second-order rate constants are significant.⁵²

IV. Conclusions

We demonstrate that there is only one dissociation channel of nitrosobenzene at both 248 and 193 nm. No products corresponding to the dissociation channel of $C_6H_5NO \rightarrow C_6H_4 + HNO$ were observed, in full agreement with theoretical prediction. The dissociation rate of nitrosobenzene is on a timescale much longer than the rotation of molecule, and the fragment distribution is almost isotropic. The results at 248 nm are close to that of Dick and the coworkers' measurement. In addition, about 10% of phenyl radical produced at 193 nm further decompose into benzyne and H atom, and the dissociation rates of phenyl radical as a function of internal energies were measured. The results for the dissociation of the excited C_6H_5NO and the C_6H_5 radical agree well with theoretically predicted values. In addition, the rate constant for the thermal decomposition of nitrosobenzene has been calculated with the variational RRKM theory by including the small contributions from the two low-lying excited states (T_1 and S_1). The agreement between theory and the experiment of Park et al.³⁰ was also found to be excellent, confirming for the first time the observed very high A-factor ($>10^{17} s^{-1}$).

Acknowledgements

CKN acknowledges the support from the National Science Council, Taiwan under contract no. NSC 91-2113-M-001-023. MCL and YMC are grateful to Dr. J. Park for his preliminary optimization of the TS in Figure 7 and for the support of this work from the Basic Energy Sciences, Department of Energy, under contract no. DE-FG02-97-ER14784 and the Cherry L. Emerson Center of Emory University for the use of its resources, which are in part supported by a National Science Foundation grant (CHE-0079627) and an IBM shared University Research Award. MCL also acknowledges the support from the National Science Council for a Distinguished Visiting Professorship at National Chiao Tung University in Hsichu, Taiwan.

References

- (1) Yu, T.; Lin, M. C. *J. Am. Chem. Soc.* **1993**, *115*, 4371.
- (2) Lin, M. C.; Yu, T. *Int. J. Chem. Kinet.* **1993**, *25*, 875.
- (3) Yu, T.; Lin, M. C. *J. Phys. Chem.* **1994**, *98*, 2105.
- (4) Yu, T.; Lin, M. C. *Int. J. Chem. Kinet.* **1994**, *26*, 771.
- (5) Yu, T.; Lin, M. C.; Melius, C. F. *Int. J. Chem. Kinet.* **1994**, *26*, 1095.
- (6) Yu, T.; Lin, M. C. *J. Am. Chem. Soc.* **1994**, *116*, 9571.
- (7) Yu, T.; Lin, M. C. *J. Phys. Chem.* **1995**, *99*, 8599.
- (8) Tonokura, K.; Norikane, Y.; Koshi, M.; Nakano, Y.; Nakamichi, S.; Goto, M.; Hashimoto, S.; Kawasaki, M.; Andersen Sulbaek, M. P.; Hurley, M. D.; Wallington, T. J. *J. Phys. Chem. A* **2002**, *106*, 5908.
- (9) McCoustra, M. R. S.; Pfab, J. *Chem. Phys. Lett.* **1985**, *122*, 395.
- (10) Engert, J. M.; Slenczka, A.; Kensy, U.; Dick, B. *J. Phys. Chem.* **1996**, *100*, 11883.
- (11) Bhujle, V.; Wild, U. P.; Baumann, H.; Wagniere, G. *Tetrahedron* **1976**, *32*, 467.
- (12) Bhujle, V. *V. Spectrosc. Lett.* **1997**, *10*, 587.
- (13) Chernoff, D. A.; Hochstrasser, R. M. *Chem. Phys. Lett.* **1980**, *70*, 213.
- (14) Condirston, D. A.; Knight, A. R.; Steer, R. P. *J. Photochem.* **1980**, *14*, 257.
- (15) Hatton, W. G.; Hacker, N. P.; Kasai, P. H. *J. Chem. Soc., Chem. Commun.* **1990**, 227.
- (16) Niles, S.; Wight, C. A. *Chem. Phys. Lett.* **1989**, *154*, 458.
- (17) Keßler, A.; Kensy, U.; Dick, B. *Chem. Phys. Lett.* **1998**, 289, 516.
- (18) Keßler, A.; Slenczka, A.; Seiler, R.; Dick, B. *Phys. Chem. Chem. Phys.* **2001**, *3*, 2819.
- (19) Seiler, R. D., B. *Chem. Phys.* **2003**, 288, 43.
- (20) Obernhuber, T. J.; Kensy, U.; Dick, B. *Phys. Chem. Chem. Phys.* **2003**, *5*, 2799.
- (21) Li, Y. M.; Sun, J. L.; Han, K. L.; He, G. Z. *Chem. Phys. Lett.* **2001**, 338, 297.
- (22) Huang, J. H.; Wang, G. J.; Gu, X. B.; Han, K. L.; He, G. H. *J. Phys. Chem. A* **2000**, *104*, 10079.
- (23) Tsai, S. T.; Lin, C. K.; Lee, Y. T.; Ni, C. K. *Rev. Sci. Instrum.* **2001**, *72*, 1963.
- (24) Tsai, S. T.; Lee, Y. T.; Ni, C. K. *J. Phys. Chem. A* **2000**, *104*, 10125.
- (25) Tsai, S. T.; Lin, C. K.; Lee, Y. T.; Ni, C. K. *J. Chem. Phys.* **2000**, *113*, 67.
- (26) Tsai, S. T.; Huang, C. L.; Lee, Y. T.; Ni, C. K. *J. Chem. Phys.* **2001**, *115*, 2449.
- (27) Becke, A. D. *J. Chem. Phys.* **1992**, *96*, 2155.
- (28) Becke, A. D. *J. Chem. Phys.* **1992**, *97*, 9173.
- (29) Becke, A. D. *J. Chem. Phys.* **1993**, *98*, 5648.
- (30) Park, J.; Dyakov, I. V.; Mebel, A. M.; Lin, M. C. *J. Phys. Chem.* **1997**, *101*, 6043.
- (31) Mebel, A. M.; Morokuma, K.; Lin, M. C. *J. Chem. Phys.* **1995**, *103*, 7414.

- (32) Curtiss, L. A.; Redfern, P. C.; Raghavachari, K.; Pople, J. A. *J. Chem. Phys.* **2001**, *114*, 108.
- (33) Bauernschmitt, R.; Ahlrichs, R. *Chem. Phys. Lett.* **1996**, *256*, 454.
- (34) Stratmann, R. E.; Scuseria, G. E.; Frisch, M. J. *J. Chem. Phys.* **1998**, *109*, 8218.
- (35) Casida, M. E.; Jamorski, C.; Casida, K. C.; Salahub, D. R. *J. Chem. Phys.* **1998**, *108*, 4439.
- (36) Frisch, M. J.; Trucks, G. W.; Schlegel, H. B.; Scuseria, G. E.; Robb, M. A.; Cheeseman, J. R.; Zakrzewski, V. G.; Montgomery, J. A., Jr.; Stratmann, R. E.; Burant, J. C.; Dapprich, S.; Millam, J. M.; Daniels, A. D.; Kudin, K. N.; Strain, M. C.; Farkas, O.; Tomasi, J.; Barone, V.; Cossi, M.; Cammi, R.; Mennucci, B.; Pomelli, C.; Adamo, C.; Clifford, S.; Ochterski, J.; Petersson, G. A.; Ayala, P. Y.; Cui, Q.; Morokuma, K.; Malick, D. K.; Rabuck, A. D.; Raghavachari, K.; Foresman, J. B.; Cioslowski, J.; Ortiz, J. V.; Baboul, A. G.; Stefanov, B. B.; Liu, G.; Liashenko, A.; Piskorz, P.; Komaromi, I.; Gomperts, R.; Martin, R. L.; Fox, D. J.; Keith, T.; Al-Laham, M. A.; Peng, C. Y.; Nanayakkara, A.; Gonzalez, C.; Challacombe, M.; Gill, P. M. W.; Johnson, B.; Chen, W.; Wong, M. W.; Andres, J. L.; Gonzalez, C.; Head-Gordon, M.; Replogle, E. S.; Pople, J. A. Gaussian 98; Revision A.7; Gaussian, Inc., Pittsburgh PA, 1998.
- (37) Amos, R. D.; Bernhardsson, A.; Berning, A.; Celani, P.; Cooper, D. L.; Deegan, M. J. O.; Dobbyn, A. J.; Eckert, F.; Hampel, C.; Hetzer, G.; Knowles, P. J.; Korona, T.; Lindh, R.; Lloyd, A. W.; McNicholas, S. J.; Manby, F. R.; Meyer, W.; Mura, M. E.; Nicklass, A.; Palmieri, P.; Pitzer, R.; Rauhut, G.; Schutz, M.; Schumann, U.; Stoll, H.; Stone, A. J.; Tarroni, R.; Thorsteinsson, T.; Werner, H.-J. MOLPRO; version 98.1; University of Birmingham, Birmingham, U.K., 1998.
- (38) Glassman, I. *Combustion*, 2nd ed.; Academic Press: New York, 1986.
- (39) Haynes, D. S. *Fossil Fuel Combustion*; Wiley-Interscience: New York, 1991.
- (40) Bockhorn, H. *Soot Formation in Combustion*; Springer-Verlag: New York, 1993.
- (41) Madden, L. K.; Moskaleva, L. V.; Kristyan, S.; Lin, M. C. *J. Phys. Chem. A* **1997**, *101*, 6790.
- (42) Braun-Unkoff, M.; Frank, P.; Just, T. 22nd Sym. (Int.) Combust. 1988, 1053.
- (43) Wang, H.; Laskin, A.; Moriaty, N.W., Frenklach, M., Proc. Combust. Inst. 2000, 28, 1545.
- (44) D. M. Wardlaw and R. A. Marcus, Chem. Phys. Lett. 110, 230 (1984); J. Chem. Phys. 83, 3462 (1985)
- (45) Klippenstein, S. J. *Chem. Phys. Lett.* **1990**, *170*, 71; Klippenstein, S. J. *J. Chem. Phys.* **1991**, *94*, 6469.
- (46) Klippenstein, S. J. *J. Chem. Phys.* **1992**, *96*, 367.
- (47) Robertson, S. H.; Wagner, A. F.; Wardlaw, D. M. *J. Chem. Phys.* **1995**, *103*, 2917.
- (48) Klippenstein, S. J.; Wagner, A. F.; Dunbar, R. C.; Wardlaw, D. M.; Robertson, S. H. Variflex; version 1.00, July 16, 1999.
- (49) Varshni, Y. P. *Rev. Mod. Phys.* **1957**, *29*, 664.

- (50) Horn, C.; Frank, P.; Tranter, R. S.; Schaugg, J.; Grotheer, H.-H.; Just, T. *26th Sym. (Int.) Combust.*, 1996.
- (51) Choo, K.-L.; Golden, D. M.; Benson, S. W. *Int. J. Chem. Kinet.* **1975**, 7, 713.
- (52) Lu, C.-W.; Wu, Y.-J.; Lee, Y.-P.; Zhu, R. S.; Lin, M. C. *J. Phys. Chem. A* **2003**, 107, 11020.

Experimental and theoretical investigations of rate coefficients of the reaction $S(^3P)+O_2$ in the temperature range 298–878 K

Chih-Wei Lu and Yu-Jong Wu

Department of Chemistry, National Tsing Hua University, Hsinchu 30013, Taiwan

Yuan-Pern Lee^{a)}

Department of Chemistry, National Tsing Hua University, Hsinchu 30013, Taiwan and Institute of Atomic and Molecular Sciences, Academia Sinica, Taipei 10764, Taiwan

R. S. Zhu and M. C. Lin^{b)}

Department of Chemistry, Emory University, Atlanta, Georgia 30322

(Received 1 June 2004; accepted 23 July 2004)

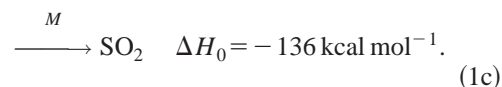
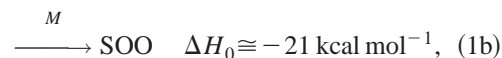
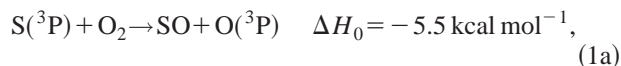
Rate coefficients of the reaction $S+O_2$ with Ar under 50 Torr in the temperature range 298–878 K were determined with the laser photolysis technique. S atoms were generated by photolysis of OCS with a KrF excimer laser at 248 nm; their concentration was monitored via resonance fluorescence excited by atomic emission of S produced from microwave-discharged SO_2 . Our measurements show that $k(298\text{ K})=(1.92\pm 0.29)\times 10^{-12}\text{ cm}^3\text{ molecule}^{-1}\text{ s}^{-1}$, in satisfactory agreement with previous reports. New data determined for 505–878 K show non-Arrhenius behavior; combining our results with data reported at high temperatures, we derive an expression $k(T)=(9.02\pm 0.27)\times 10^{-19}T^{2.11\pm 0.15}\exp[(730\pm 120)/T]\text{ cm}^3\text{ molecule}^{-1}\text{ s}^{-1}$ for $298\leq T\leq 3460\text{ K}$. Theoretical calculations at the G2M (RCC2) level, using geometries optimized with the B3LYP/6-311+G(3df) method, yield energies of transition states and products relative to those of the reactants. Rate coefficients predicted with multichannel RRKM calculations agree satisfactorily with experimental observations; the reaction channel via $SOO(^1A')$ dominates at $T<500\text{ K}$, whereas channels involving formation of $SOO(^3A'')$ followed by isomerization to SO_2 before dissociation, and formation of $SOO(^1A'')$ followed by direct dissociation, become important at high temperatures, accounting for the observed rapid increase in rate coefficient. © 2004 American Institute of Physics. [DOI: 10.1063/1.1792611]

I. INTRODUCTION

The reaction of $S(^3P)$ with O_2 is important in combustion chemistry; it plays an important role in the SO_x emission during combustion of fuels containing sulfur compounds. Table I summarizes rate coefficients reported for this reaction. The rate coefficient for this reaction near room temperature has been extensively investigated and values are reported in the range $(1.5\text{--}2.8)\times 10^{-12}\text{ cm}^3\text{ molecule}^{-1}\text{ s}^{-1}$.^{1–7} The temperature dependence of the rate coefficient below 423 K was reported to be small, with E_a/R values of $0\pm 50\text{ K}$ (Ref. 3) or $-(153\pm 108)\text{ K}$.⁶ Measurements of rate coefficients at high temperatures ($T\geq 675\text{ K}$) have large discrepancies. Although the activation energy reported by Homann, Krome, and Wagner⁸ ($E_a/R=2820\text{ K}$) is similar to that ($E_a/R=3110\text{ K}$) reported by Woiki and Roth,⁹ the preexponential factors A vary more than fourfold. Saito *et al.*¹⁰ reported a value $k=(6.3\pm 1.2)\times 10^{-12}\text{ cm}^3\text{ molecule}^{-1}\text{ s}^{-1}$ for temperatures between 1900 and 2200 K, about 0.4 times that reported by Woiki and Roth in this temperature range.⁹ Matsui and co-workers^{7,11} re-

ported $E_a/R=1840\pm 300\text{ K}$ for temperatures between 980 and 1610 K, much smaller than that reported by Woiki and Roth,⁹ but rate coefficients determined in both works are within experimental uncertainties in the overlapping temperature range 1138–1610 K. No experimental data exist for temperatures between 423 and 980 K except much smaller, and likely erroneous, values reported by Homann, Krome, and Wagner for $T\geq 675\text{ K}$.⁸

The reaction might proceed via various channels:



Formation of O atoms was observed near 300 K (Ref. 3) and at high temperatures.^{9,10} Miyoshi *et al.*⁷ reported the yield of O atom to be 1.05 ± 0.14 at 1566 K and 924 Torr, 1.06 ± 0.11 at 293 K and 2.02 Torr, and 1.04 ± 0.12 at 293 K and 50.2 Torr (all with Ar buffer gas), indicating that reactions (1b) and (1c) are unimportant.

The reaction of $S(^3P)$ with O_2 is expected to proceed via multiple potential-energy surfaces (PES). Based on an ob-

^{a)} Author to whom correspondence should be addressed. Electronic mail: yplee@mail.nctu.edu.tw

^{b)} Author to whom correspondence should be addressed. Also at Center for Interdisciplinary Molecular Science, Chiao Tung University, Hsinchu, Taiwan. Electronic mail: chemmcl@emory.edu

TABLE I. Summary of reported experimental rate coefficients using various methods.

Temperature /K	Pressure (gas) /Torr	$k(\sim 298\text{ K})$ / 10^{-12} , ^a	A / 10^{-12} , ^a	E_a/R /K	Method ^b	Author names	Reference
298	2.2 (Ar)	2.0 ± 0.5			DF/CL	Fair and Thrush (FT)	1
298	60–200 (CO ₂ , Ar)	2.8 ± 0.3			FP/ABS	Fair, Roodselaar, and Strausz (FRS)	2
295	113 (Ar)	1.7 ± 0.3			FP/ABS	Donovan and Little (DL)	4
298	0.98–3.0 (He)	1.5 ± 0.5			DF/RF	Clyne and Townsend (CT)	5
293	2–50 (Ar)	2.27 ± 0.08			LP/LIF	Miyoshi <i>et al.</i> (MSTM)	7
252–423	20–200 (CO ₂ , He, Ar)	2.32 ± 0.27	2.24 ± 0.27	0 ± 50	FP/RF	Davis, Klemm, and Pilling (DKP)	3
296–393	0.72–1.15 (Ar)	2.6 ± 0.3	1.7 ± 0.5	$-(153 \pm 108)$	DF/RF	Clyne and Whitefield (CW)	6
675–1090	1–60 (Ar)		16.6	2820	DF/MS	Homann, Krome, and Wagner (HKW)	8
980–1610	>578 (Ar)		25 ± 6	1840 ± 300	ST/ABS	Miyoshi <i>et al.</i> (MSTM)	7
1138–3463	281–953 (Ar)		69.8	3110	ST/ABS	Woiki and Roth (WR)	9
1900–2200	>1212 (Ar)		6.3 ± 1.2^c	0^c	ST/ABS	Saito <i>et al.</i> (SUIKI)	10
298–878	50 (Ar)	1.92 ± 0.29	^d	^d	LP/RF	This work	...

^aIn units of $\text{cm}^3 \text{ molecule}^{-1} \text{ s}^{-1}$.

^bDF—discharge flow; FP—flash photolysis; LP—laser photolysis; ST—shock tube; CL—chemiluminescence; ABS—absorption; RF—resonance fluorescence; LIF—laser-induced fluorescence.

^c $k(T) = 1.2 \times 10^{-13} T^{0.52} \text{ cm}^3 \text{ molecule}^{-1} \text{ s}^{-1}$ for all data reported in the range 250–2200 K.

^d $k(T) = (9.02 \pm 0.27) \times 10^{-19} T^{2.11 \pm 0.15} \exp[(730 \pm 120)/T] \text{ cm}^3 \text{ molecule}^{-1} \text{ s}^{-1}$ for temperature range 298–3460 K.

served small rate coefficient, Fair *et al.* proposed that reaction (1) proceeds via SOO, which subsequently decomposes to SO+O;² the end-on attack to form SOO leads to an effective cross section for collisions much smaller than that associated with the side-on attack, hence a smaller rate coefficient. The existence of intermediate SOO is supported by its infrared absorption spectrum recorded after photolysis with laser radiation at 193 nm of an Ar matrix sample containing SO₂.¹² Craven and Murrell performed quasiclassical trajectory (QCT) calculations and predicted a rate coefficient of $(1.67 \pm 0.17) \times 10^{-12} \text{ cm}^3 \text{ molecule}^{-1} \text{ s}^{-1}$ for reaction (1) at 298 K, in satisfactory agreement with experiment.^{13,14} All trajectories show a common mechanism in which an initial SOO intermediate is formed, followed by rapid isomerization to OSO, which subsequently dissociates to O+SO. Lendvay, Shatz, and Harding performed a similar study with a many-body expansion (MBE) PES calibrated with extensive *ab initio* calculations.¹⁵ Rodrigues and Varandas¹⁶ performed QCT calculations with an accurate single-value double many-body expansion (DMBE) PES of SO₂ (Ref. 17) and obtained rate coefficients of reaction (1) and its reverse reaction in the temperature range 50–3500 K; the rate coefficient predicted at 300 K, $(6.21 \pm 0.08) \times 10^{-12} \text{ cm}^3 \text{ molecule}^{-1} \text{ s}^{-1}$, is about two to four times that determined experimentally. They indicate that nearly all trajectories evolve via intermediate SOO, and only about one quarter of the trajectories are associated with a long-lived SO₂ isomer having a lifetime ~ 1.5 ps.

We have performed careful experimental work on the reaction of S+O₂ under 50 Torr of Ar and extended rate measurements from 298 to 878 K to bridge between the region $T \leq 423$ K with a nearly temperature-independent rate coefficient and the region $T \geq 980$ K in which rate coefficients show an activation energy corresponding to $E_a/R = 1840$ –3110 K. We also performed detailed theoretical cal-

culations to predict rate coefficients and to identify important channels in this reaction at various temperatures.

II. EXPERIMENTS

The experimental setup was described in detail previously;^{18,19} only a brief description is given. The reaction vessel is a six-way tubular quartz cross (diameter 40 mm) with one axis having sidearms ≈ 15 cm in length and with Brewster windows for laser photolysis. The temperature of the reactor was regulated through resistive heating with a temperature controller (Omega CN 9000). S atoms were produced by photolysis of OCS with radiation from a pulsed KrF excimer laser at 248 nm (24 – 60 mJ cm^{-2} , 1 – 3 Hz). Excessive Ar gas was added to the system to ensure that most S(¹D) is quenched before reaction.²⁰ S atoms were excited with emission of S(³S)–S(³P_{2,1,0}) at 180.73, 182.03, and 182.62 nm, respectively, from a microwave-discharge lamp with a flowing gas mixture of SO₂ $\sim 0.10\%$ in He. An S1-UV lens (focal length $f = 5$ cm) served to collect light of wavelength $\lambda > 170$ nm and to discriminate against emission of shorter wavelength.

The fluorescence was collected perpendicular to both photolysis laser and probe beams with a MgF₂ lens ($f = 5$ cm) before being detected with a solar-blind photomultiplier tube (EMR 541G-09). The signal was converted to voltage with a low-noise amplifier (Stanford Research Systems, SR570) before being transferred to a digital oscilloscope (Tektronix, TDS-620B, 2.5 GS s^{-1} with 500 MHz band width). The signal was typically averaged over more than 500 laser pulses. The temporal profiles of S atoms were transferred to a computer for further processing.

He (99.9995%), Ar (99.9995%), and O₂ (99.999%, all AGA Specialty Gases) were used without further purification. OCS (99.98%, Matheson) was purified through trap-to-

trap distillation. A 20% mixture of OCS in Ar was prepared with standard gas handling techniques. Flow rates of He, Ar, O_2 , and the OCS/Ar mixture were monitored with mass flowmeters (Tylan FM360) that were calibrated with a wet testmeter and by the pressure increase in a calibrated volume before and after experiments.

Typical experimental conditions were as follows: total flow rate $F_T = 7-11 \text{ STP cm}^3 \text{ s}^{-1}$ (STP=1 atm and 273 K), total pressure $P \approx 50 \text{ Torr}$, reaction temperature $T = 298-878 \text{ K}$, $[OCS] = (1.50-37.5) \times 10^{14} \text{ molecule cm}^{-3}$, $[S] = (1.4-33.4) \times 10^{11} \text{ molecule cm}^{-3}$, $[O_2] = (1.0-35.7) \times 10^{14} \text{ molecule cm}^{-3}$, $[Ar] = (5.5-16.5) \times 10^{17} \text{ molecule cm}^{-3}$, probed intervals of decay = 20 μs –20 ms, and mean flow speed $v = 5.9-24.2 \text{ cm s}^{-1}$.

III. COMPUTATIONAL METHODS

The geometries of reactants, intermediates, transition states, and products of the title reaction were optimized at the B3LYP/6-311+G(3df) level of theory with Becke's three-parameter nonlocal exchange functional²¹ and the nonlocal correlation functional of Lee, Yang, and Parr.²² Energies of all species were calculated at the G2M(RCC2) level of theory²³ using geometries optimized with the B3LYP/6-311+G(3df) method. Intrinsic reaction coordinate calculations²⁴ were performed to connect each transition state with designated reactants and products. All calculations were carried out with GAUSSIAN98 (Ref. 25) and MOLPRO 2002 programs.²⁶

Rate coefficients for various reaction channels were calculated with a microcanonical variational RRKM method using the Variflex program.²⁷ The component rates were evaluated at E , J -resolved levels. The master equation was solved with an inversion approach for association and an eigenvalue-based approach for dissociation.^{28,29} For the barrierless transition state, we used a Morse potential

$$E(R) = D_e [1 - e^{-\beta(R-R_e)}]^2, \quad (2)$$

in which D_e is the dissociation energy (D_0) plus zero-point energy, R_e is the equilibrium bond distance, and β is fitted from calculated potential energies at discrete atomic separations R , to represent the potential energy in a stretching mode along the minimum energy path of each individual reaction coordinate. In addition, a Lennard-Jones pairwise potential and an anisotropic potential (a form for potential anisotropy assuming a bonding potential that is cylindrically symmetric with respect to each fragment) are combined to form the final potential for calculation of the variational rate coefficient with the Variflex code. For tight transition states, numbers of states were calculated with the rigid-rotor harmonic-oscillator approximation.

IV. RESULTS AND DISCUSSION

A. Experimental rate coefficient

All experiments were carried out under pseudo-first-order conditions with $[O_2]/[S]$ greater than 200. The initial concentration of S, $[S]_0$, was estimated from the absorption cross section ($2.36 \times 10^{-20} \text{ cm}^2$) of OCS and quantum yield $\Phi(S) = 0.72 \pm 0.08$ at 248 nm,³⁰ and the fluence of the pho-

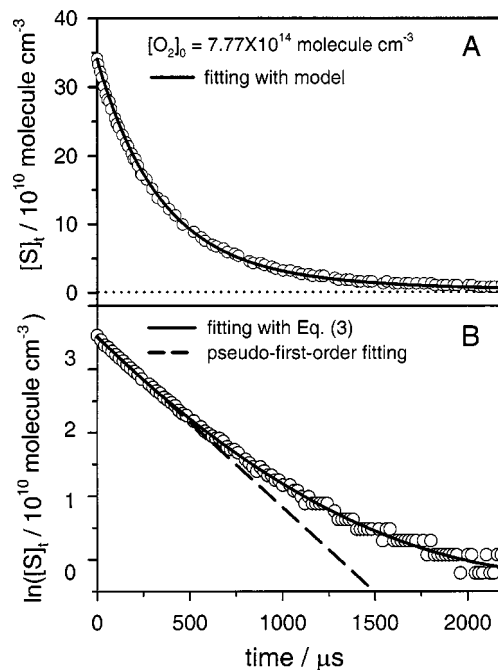
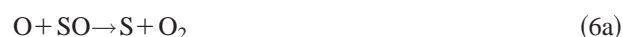


FIG. 1. (A) Temporal profiles of $[S]_t$ observed after photolysis of an Ar sample containing OCS and O_2 . $T = 878 \text{ K}$, $[O_2] = 7.77 \times 10^{14} \text{ molecule cm}^{-3}$, $[OCS] = 3.83 \times 10^{14} \text{ molecule cm}^{-3}$, and $[Ar] = 5.53 \times 10^{17} \text{ molecule cm}^{-3}$. The solid line represents fitted results according to a model described in the text. (B) Semilogarithmic plot of (A). The solid line represents fitted results according to Eq. (3) and the dashed line represents initial pseudo-first-order decay.

tolysis laser. Figure 1(a) shows a typical temporal profile of $[S]$ observed when a flowing gas mixture containing OCS, O_2 , and Ar was irradiated at 248 nm; a semilogarithmic plot is shown in Fig. 1(b). The relative concentration of S atoms, $[S]_t$, follows an exponential decay in the initial stage. The apparent pseudo-first-order rate coefficient k^1 may be derived with the equation

$$\ln([S]_t/[S]_0) = -k^1 t + at^2 - bt^3, \quad (3)$$

in which t is the reaction time and a and b are fitting parameters to account for secondary reactions. To derive accurate rate coefficients, we employed a model consisting of the following reactions:





for which rate coefficients have these reported dependences on temperature:

$$k_{1b}(T) = 1.09 \times 10^{-25} T^{-2.6} \times \exp(-276/T) \text{ cm}^6 \text{ molecule}^{-2} \text{ s}^{-1}, \quad (13)$$

$$k_{4a}(T) = 0.12 T^{-2.19} \times \exp(-10630/T) \text{ cm}^3 \text{ molecule}^{-1} \text{ s}^{-1}, \quad (14)$$

$$k_{4b}(T) = 7.02 \times 10^{-4} T^{-1.72} \times \exp(-10803/T) \text{ cm}^3 \text{ molecule}^{-1} \text{ s}^{-1}, \quad (15)$$

$$k_5(T) = 3.16 \times 10^{-19} T^{2.35} \times \exp(-1253/T) \text{ cm}^3 \text{ molecule}^{-1} \text{ s}^{-1} \quad (16)$$

$$k_{6a}(T) = 3.76 \times 10^{-18} T^{1.79} \times \exp(-2230/T) \text{ cm}^3 \text{ molecule}^{-1} \text{ s}^{-1} \quad (17)$$

$$k_{6b}(T) = 4.82 \times 10^{-31} (T/298)^{-2.17} \text{ cm}^6 \text{ molecule}^{-2} \text{ s}^{-1} \quad (18)$$

$$k_{7a}(T) = 6.61 \times 10^{-11} \exp(-2706/T) \times (0.4 - 202/T) \text{ cm}^3 \text{ molecule}^{-1} \text{ s}^{-1} \text{ (Ref. 31)} \quad (19)$$

$$k_{7b}(T) = 6.61 \times 10^{-11} \exp(-2706/T) \times (0.6 + 202/T) \text{ cm}^3 \text{ molecule}^{-1} \text{ s}^{-1} \text{ (Ref. 31)} \quad (20)$$

$$k_8(T) = 2.16 \times 10^{-27} T^{-2.7} \text{ cm}^6 \text{ molecule}^{-2} \text{ s}^{-1} \text{ (Ref. 32)} \quad (21)$$

$$k_9(T) = 1.0 \times 10^{-12} \times \exp(-1720/T) \text{ cm}^3 \text{ molecule}^{-1} \text{ s}^{-1} \text{ (Ref. 33)} \quad (22)$$

$$k_{10}(T) = 1.7 \times 10^{-12} \times \exp(-4089/T) \text{ cm}^3 \text{ molecule}^{-1} \text{ s}^{-1} \text{ (Ref. 34)} \quad (23)$$

$$k_{11}(T) = 1.86 \times 10^{-40} \times \exp(-4829/T) \text{ cm}^3 \text{ molecule}^{-1} \text{ s}^{-1} \text{ (Ref. 35)} \quad (24)$$

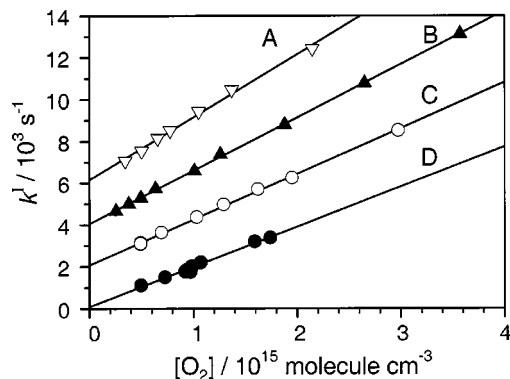


FIG. 2. Derived k_{1a}^1 as a function of $[\text{O}_2]$ at various temperatures. (A) 878 K, symbol ∇ ; (B) 726 K, symbol \blacktriangle ; (C) 658 K, symbol \circ ; (D) 298 K, symbol \bullet . The ordinates are shifted for each set of data for clarity.

$$k_{12}(T) = 2.2 \times 10^{-11} \times \exp(-84/T) \text{ cm}^3 \text{ molecule}^{-1} \text{ s}^{-1} \text{ (Ref. 14)} \quad (25)$$

in which k_{1b} , k_{4a} , and k_{4b} are calculated results discussed in the following section, k_5 is derived on fitting data at high temperatures ($860 \leq T \leq 1680$ K) (Ref. 36) and low temperatures ($233 \leq T \leq 445$ K) (Ref. 37) to the equation, k_{6a} is derived on fitting data at high temperatures ($2212 \leq T \leq 3385$ K) (Ref. 38) and those at low temperatures ($252 \leq T \leq 423$ K) (Ref. 3) estimated from k_{1a}^1 and the equilibrium constants based on ΔG of formation,³⁹ and k_{6b} is theoretically predicted in our previous work on pyrolysis of SO_2 ;³⁸ the latter agrees satisfactorily with the expression $9.3 \times 10^{-31} (T/298)^{-1.84} \text{ cm}^6 \text{ molecule}^{-2} \text{ s}^{-1}$ reported by Grillo, Reed, and Slack.⁴⁰

We modeled observed temporal profiles of $[\text{S}]_t$ with reactions (1a), (1b), and (4)–(12) with a commercial kinetic modeling program FACSIMILE;⁴¹ rate coefficients listed in Eqs. (13)–(25) were held constant and the pseudo-first-order rate coefficient of the title reaction, k_{1a}^1 , was varied to yield the best fit. Summary of experimental conditions and values of k_{1a}^1 for 58 measurements in a temperature range 298–878 K may be found in Electronic Physics Auxiliary Publication Service (EPAPS); we list also k^1/k_{1a}^1 for comparison.⁴² Values of k^1 obtained with Eq. (3) based on initial pseudo-first-order decays deviate from k_{1a}^1 by less than 15% in most cases, indicating that secondary reactions play only a minor role under the initial experimental conditions. Detailed modeling shows that secondary reactions are negligible at low temperatures, whereas at high temperatures and with large $[\text{OCS}]$ and $[\text{S}]_0$ the corrections become greater; only reactions (5), (7a), and (7b) account for corrections greater than 3%.

Values of k_{1a}^1 determined with various concentrations of O_2 at temperatures 298, 658, 726, and 878 K are plotted in Fig. 2, with ordinates shifted vertically for each line for clarity; the slope of the line fitted with least squares yields the bimolecular rate coefficient k_{1a}^1 at each temperature. At 298 K, $k_{1a}^1 = (1.92 \pm 0.08) \times 10^{-12} \text{ cm}^3 \text{ molecule}^{-1} \text{ s}^{-1}$; unless otherwise noted, the uncertainty represents one standard error in fitting. In these experiments, rate coefficients remained

TABLE II. Bimolecular rate coefficients k_{1a} at various temperatures.

Temp /K	P /Torr	$[S]$ / 10^{11} , ^a	$[O_2]$ / 10^{14} , ^a	$[Ar]$ / 10^{17} , ^a	k_{1a} / 10^{-12} , ^b
298	51	2.12–33.4	4.96–17.4	16.5	1.92 ± 0.29
406	51	7.65	2.24–12.3	12.0	1.74 ± 0.26
505	50	7.72	1.01–4.43	9.6	1.77 ± 0.27
658	51	5.37–14.7	4.91–29.7	7.4	2.19 ± 0.33
726	51	4.27	2.57–35.7	6.7	2.55 ± 0.38
878	50	3.41–11.13	3.45–21.5	5.5	3.01 ± 0.45

^aIn units of molecule cm^{-3} .^bIn units of cm^3 molecule $^{-1}$ s $^{-1}$.

the same while $[S]_0$ was varied from 2.1×10^{11} to 3.34×10^{12} molecule cm^{-3} . Combined systematic error (measurements of flow rates, pressure, and temperature) of our system is estimated to be $\sim 8\%$, and the error in deriving k_{1a} and its dependence on $[O_2]$ is $\sim 12\%$. Hence, we estimate an error $\sim 15\%$ for k_{1a} and recommend a rate coefficient $(1.92 \pm 0.29) \times 10^{-12}$ cm^3 molecule $^{-1}$ s $^{-1}$ at 298 K.

Rate coefficients k_{1a} determined at 298, 406, 505, 658, 726, and 878 K are listed in Table II. k_{1a} remains approximately constant from 298 to 505 K, but increases from $\sim 1.8 \times 10^{-12}$ to 3.0×10^{-12} cm^3 molecule $^{-1}$ s $^{-1}$ as the temperature increases further to 878 K. In the temperature range 298–505 K, rate coefficients show a small negative temperature dependence with $E_a/R = -(65 \pm 40)$ K. Reported rate coefficients are compared in Table I and Fig. 3; lines of various types are drawn for only the range of temperature investigated. The value of k_{1a} at 298 K determined in this work is within experimental uncertainties of previous reports by Fair and Thrush (designated FT in Fig. 3),¹ Donovan and Little (DL),⁴ Clyne and Townsend (CT),⁵ Miyoshi *et al.* (MSTM),⁷ and Davis, Klemm, and Pilling (DKP),³ but is slightly smaller than values of $(2.6 \pm 0.3) \times 10^{-12}$ cm^3 molecule $^{-1}$ s $^{-1}$ by Clyne and Whitefield (CW)⁶ and $(2.8 \pm 0.3) \times 10^{-12}$ cm^3 molecule $^{-1}$ s $^{-1}$ by Fair, Roodselaar, and Strausz (FRS).² The small negative activation energy of $E_a/R = -(65 \pm 40)$ K is consistent also with two previous reports of $E_a/R = -(153 \pm 108)$ K by CW⁶ and 0 ± 50 K by DKP,³ even though their rate coefficients are slightly greater

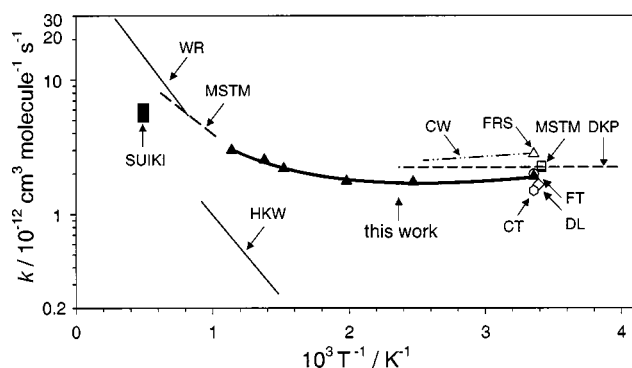


FIG. 3. Arrhenius plots of k_{1a} for the reaction $S+O_2 \rightarrow O+SO$. Our data are shown as symbols \blacktriangle with a fitted equation shown as a thick solid line. Previous results on temperature dependence are shown as lines of various types drawn for the temperature range of study. A combination of first characters of each authors last name is used to indicate previous reports, as listed in Table I.

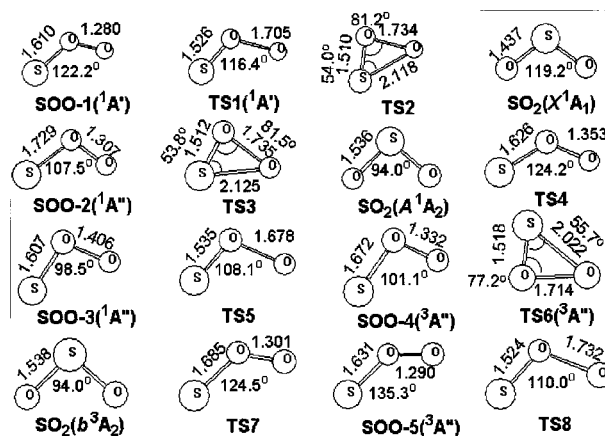


FIG. 4. Optimized geometries of transition states and intermediates of the $S+O_2$ system at the B3LYP/6-311+G(3df) level, with bond lengths in \AA and bond angles in degree. Small and large solid spheres in the structures represent O and S atoms, respectively.

than ours. Rate coefficients at 505–878 K are new; they match well with rate coefficients reported for $T \geq 980$ K by MSTM (Ref. 7) and WR,⁹ as illustrated in Fig. 3.

Fitting our results yields an expression for the rate coefficient in the range $298 \leq T \leq 878$ K:

$$k_{1a}(T) = (8.60 \pm 0.34) \times 10^{-20} T^{2.40 \pm 0.24} \times \exp[(960 \pm 120)/T] \text{ cm}^3 \text{ molecule}^{-1} \text{ s}^{-1}. \quad (26)$$

When combined with data at high temperatures by MSTM and WR, a general expression

$$k_{1a}(T) = (9.02 \pm 0.27) \times 10^{-19} T^{2.11 \pm 0.15} \times \exp[(730 \pm 120)/T] \text{ cm}^3 \text{ molecule}^{-1} \text{ s}^{-1} \quad (27)$$

is derived for $298 \leq T \leq 3460$ K. This equation reproduces reported rate coefficients by MSTM, WR, and our work to within 30% except a few data points.

B. Potential-energy surfaces and reaction mechanism

Our calculations show that several triplet and singlet intermediates and transition states are involved in the reaction $S(^3P)+O_2(X^3\Sigma_g^-)$ to produce $SO(X^3\Sigma^-)+O(^3P)$. Optimized geometries of the intermediates and transition states involved in the reaction are shown in Fig. 4. The energy diagrams for singlet and triplet surfaces calculated with the G2M(RCC2)//B3LYP/6-311+G(3df) method are presented in Fig. 5. Predicted vibrational wave numbers and rotational constants as well as available experimental data^{43–47} for the species involved are discussed and summarized in Table 4 of Ref. 38. The results indicate that the predicted vibrational wave numbers are underestimated by 0.2%–2.3% from experimental values.

The predicted enthalpy of reaction, -4.8 kcal mol^{-1} , for reaction (1a) is near the value obtained from JANAF Thermochemical Tables, -5.5 kcal mol^{-1} .³⁹ Figure 5 shows that $S(^3P)+O_2(X^3\Sigma_g^-)$ might proceed via singlet and triplet SOO intermediates. The singlet channels involve two sur-

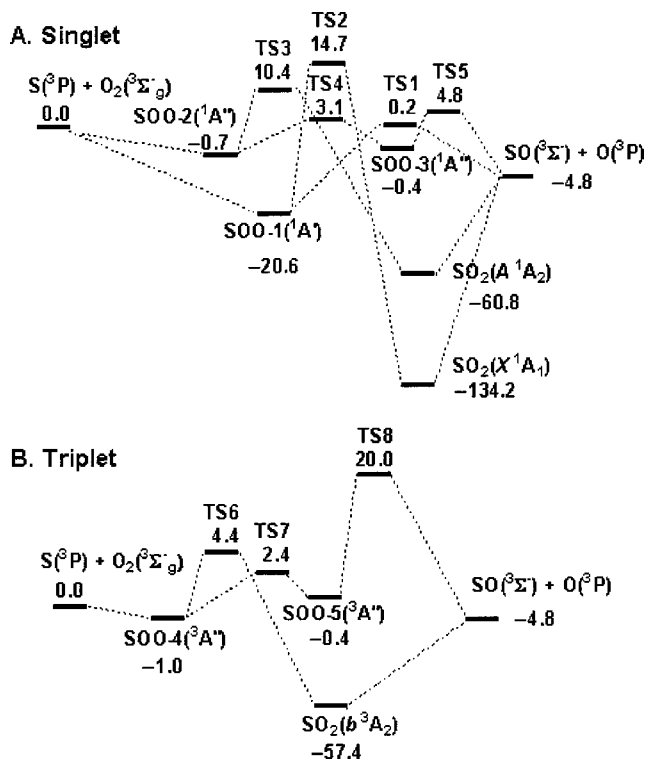


FIG. 5. Potential-energy diagrams for the $S+O_2$ reaction based on energies calculated at the G2M(RCC2)//B3LYP/6-311+G(3df) level: (A) singlet system and (B) triplet system. Energies are listed in kcal mol⁻¹.

faces, $1A'$ and $1A''$. The $1A'$ intermediate (SOO-1) is more stable than those of $1A''$ (SOO-2 and SOO-3) and has no barrier for formation from $S(^3P)+O_2(X^3\Sigma_g^-)$. The predicted energy of SOO-1, 113.6 kcal mol⁻¹ above $SO_2(X^1A_1)$, is similar to a value of 117 kcal mol⁻¹ predicted by Kellogg and Schaefer,⁴⁸ but greater than a value of 105 kcal mol⁻¹ predicted by Dunning and Raffanetti⁴⁹ who employed a two-reference CI method with generalized valence-bond (GVB) natural orbitals. SOO-1 can directly dissociate to $SO+O$ via TS1 lying only about 0.2 kcal mol⁻¹ above $S(^3P)+O_2(X^3\Sigma_g^-)$. This channel is hence the most important path at low temperature. Otherwise, SOO-1 can isomerize to $SO_2(X^1A_1)$ via TS2 with a large barrier, 14.7 kcal mol⁻¹ above the reactants; this process is kinetically unimportant for the formation of $SO+O$. The second singlet channel proceeds via SOO-2($1A''$) and SOO-3($1A''$) to form $SO+O$. TS4 connects SOO-2($1A''$) and SOO-3($1A''$), and TS5 corresponds to dissociation of SOO-3($1A''$) to the products. Transition states TS4 and TS5 lie 3.1 and 4.8 kcal mol⁻¹, respectively, above $S+O_2$. In addition, SOO-2 can isomerize to $SO_2(A^1A_2)$ via TS3 with a barrier of 10.4 kcal mol⁻¹ above the reactants, followed by dissociation to products.

The triplet channel proceeds via SOO-4($3A''$) without a barrier, followed by formation of $SO_2(b^3A_2)$ and SOO-5($3A''$) via TS6 and TS7 with barriers of 5.4 and 3.4 kcal mol⁻¹, respectively. $SO_2(b^3A_2)$ directly dissociates to $SO+O$ with an endothermicity of 52.6 kcal mol⁻¹ and SOO-5($3A''$) dissociates to $SO+O$ via TS8 at 20.0 kcal mol⁻¹ above $S(^3P)+O_2(X^3\Sigma_g^-)$. The above singlet

channel via TS4 and TS5 and the triplet channel via TS6 are expected to be insignificant at low temperatures, but become important at high temperatures.

The quintuplet surface is also investigated in this work, but no stable intermediates are found. One direct abstraction channel with a linear transition state is located; it lies 54.4 kcal mol⁻¹ above the reactants $S+O_2$. Hence, the contribution of quintuplet surfaces to production of $SO+O$ is negligible even at high temperature.

Calculations based on variational transition-state and RRKM theories were carried out with the Variflex code²⁷ for the overall reaction



via three possible channels to yield rate coefficients

$$k_{1a-1}(T) = 6.78 \times 10^{-14} T^{0.53} \times \exp(-15/T) \text{ cm}^3 \text{ molecule}^{-1} \text{ s}^{-1}, \quad (28)$$

$$k_{1a-2}(T) = 1.07 \times 10^{-14} T^{0.96} \times \exp(-1980/T) \text{ cm}^3 \text{ molecule}^{-1} \text{ s}^{-1}, \quad (29)$$

$$k_{1a-3}(T) = 8.69 \times 10^{-15} T^{0.89} \times \exp(-2240/T) \text{ cm}^3 \text{ molecule}^{-1} \text{ s}^{-1}. \quad (30)$$

Channel 1 proceeds via SOO-1($1A'$) and TS1 that has the smallest barrier relative to $S+O_2$. Channel 2 involves SOO-4($3A''$) and TS6 on the triplet surface, with an energy of 4.4 kcal mol⁻¹, whereas channel 3 proceeding via SOO-2($1A''$), TS4, SOO-3($1A''$), and TS5; TS5 has the greatest energy (4.8 kcal mol⁻¹) among these three channels. The predicted total rate coefficients are expressed as

$$k_{1a}(T) = 1.29 \times 10^{-17} T^{1.78} \times \exp(430/T) \text{ cm}^3 \text{ molecule}^{-1} \text{ s}^{-1}. \quad (31)$$

In the above calculations, the association from $S+O_2$ to the potential minimum SOO-1($1A'$) was calculated on increasing the S-O bond distance from its equilibrium value of 1.610 to 3.740 Å at intervals of 0.1 Å with the B3LYP/6-311+G(3df) method; the calculated energies were fitted to a Morse equation [Eq. (2)] to evaluate $\beta=4.06$ Å⁻¹. For the associations from $S+O_2$ to SOO-2($1A''$) and to SOO-4($3A''$), because the wells are shallow, -0.7 and -1.0 kcal mol⁻¹, the rate coefficients for channels 2 and 3, respectively; furthermore, because structures of SOO-1($1A'$), SOO-2($1A''$), and SOO-4($3A''$) are similar, the same value of β (4.06 Å⁻¹) was used for the association processes. Dissociation energies predicted at the G2M level are used in calculations of the rate coefficient for association. The Lennard-Jones (LJ) parameters required for the RRKM calculations are the same as those used for the reaction $O+SO$ previously.³⁸ The exponential-down model with $\alpha=1500$ cm⁻¹ is employed for collisional deactivation. Because the electronic ground state of the S atom is split into three (quintuplet, triplet, and singlet) degenerate levels separated by 396.1 and 573.6 cm⁻¹, the electronic partition function of these low-lying excited states are also taken into account in calculations of the rate constant.

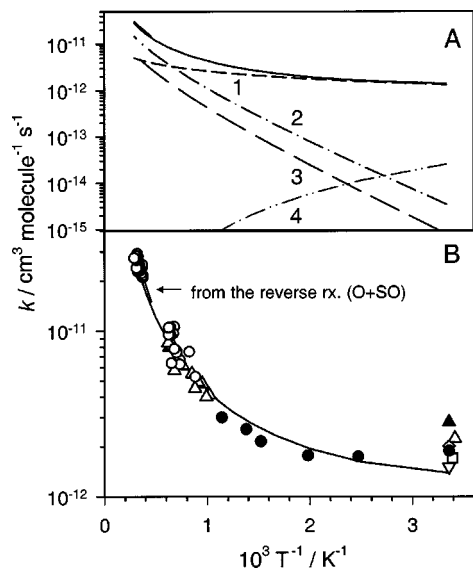


FIG. 6. (A) Theoretically predicted rate coefficients for the reaction $S + O_2 \rightarrow O + SO$. Channel 1—via $SOO-1(^1A')$ and TS1; channel 2—via $SOO-4(^3A'')$, TS6, and $SO_2(b^3A_2)$; channel 3—via $SOO-2(^1A'')$, TS3, $SOO-3(^1A'')$, and TS4; channel 4—rate of association of $SOO(^1A')$; solid line—total rate coefficient. (B) Comparison of predicted total rate coefficient k_{1a} (solid line) with experimental data (●—this work; ○—Woiki and Roth (Ref. 9); △—Miyoshi *et al.* (Ref. 7); ◇—Fair and Thrush (Ref. 1); ▲: Fair, Roodselaar, and Strausz (Ref. 2); ▽—Clyne and Townsend (Ref. 5); □—Donovan and Little (Ref. 4).

Rate coefficients for each channel and the total rate coefficient, Eq. (31), for the title reaction are plotted in Fig. 6(a); the total rate coefficient is compared with experimental results on an expanded scale in Fig. 6(b). Channel 1 is clearly the only available path at temperatures below 500 K, whereas channels 2 and 3 become important at higher temperatures, resulting in a more rapid increase of the rate coefficient at high temperatures. The total rate coefficient agrees satisfactorily with experimental results in this work, and also with those at high temperatures reported by Miyoshi *et al.*⁷ and by Woiki and Roth.⁹ In our previous experiments using a diaphragmless shock tube to investigate pyrolysis of SO_2 ,³⁸ we observed formation of S atoms from the secondary reaction,



and determined a rate coefficient for the temperature range 2212–3385 K

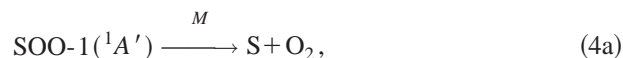
$$k_{6a}(T) = (3.0 \pm 0.3) \times 10^{-11} \times \exp[-(6980 \pm 280)/T] \text{ cm}^3 \text{ molecule}^{-1} \text{ s}^{-1}. \quad (32)$$

Combining with the equilibrium constant derived from literature values of $\Delta G(T)$ for the corresponding species,³⁹ we derive the rate expression for the title reaction in the temperature range 2212–3385 K to be

$$k_{1a}(T) = (1.1 \pm 0.3) \times 10^{-11} \times \exp[-(4360 \pm 220)/T] \text{ cm}^3 \text{ molecule}^{-1} \text{ s}^{-1}. \quad (33)$$

The results are consistent with previous experimental results by Woiki and Roth,⁹ and our theoretical predictions described above, as compared in Fig. 6.

The formation of SO_2 via channel 2 is negligibly small. SOO might be produced at high pressure and low temperature via channel 1 [Reaction (1b)]; subsequent decomposition might produce $S + O_2$ and $SO + O$:



Rate coefficients for reactions (1b), (4a), and (4b) are predicted, as listed in Eqs. (13)–(15); they are negligibly small at 50 Torr and 298 K.

It must be mentioned that the predicted rate coefficients at low temperatures are sensitive to pressure and the energy of TS1. Our results show that, at 298 K, increasing the pressure to 700 Torr and decreasing the exit barrier of TS1 by 0.2 kcal mol⁻¹ can well reproduce the experimental value; a negative temperature-dependent effect on the rate coefficient k_{1a} in the low temperature range, 200–298 K, is also obtained, which is attributed to combined effects of the barrierless association reaction (1b) and the decomposition reaction (4b).

V. CONCLUSION

Rate coefficients for the reaction of S with O_2 to form O and SO in the temperature range 298–878 K are determined using laser photolysis for production of S atoms and resonance fluorescence for detection of S atoms. Our result at 298 K, $k_{1a} = (1.92 \pm 0.29) \times 10^{-12} \text{ cm}^3 \text{ molecule}^{-1} \text{ s}^{-1}$, is consistent with previous measurements, and new data in the range 505–878 K fill the gap between reported rate coefficients for $T \leq 423$ K and $T \geq 980$ K. From combined available data, rate coefficients fit well with the equation $k_{1a}(T) = (9.02 \pm 0.27) \times 10^{-19} T^{2.11 \pm 0.15} \exp[(730 \pm 120)/T] \text{ cm}^3 \text{ molecule}^{-1} \text{ s}^{-1}$ for temperatures in the range 298–3460 K; listed uncertainties represent one standard error in fitting. Theoretical calculations based on PES computed at the G2M(RCC2)//B3LYP/6-311+(3df) level indicate that the reaction proceeds to form SOO having various conformations; the reaction path via $SOO(^1A')$ to form $SO + O$ dominates at $T \leq 500$ K, but two additional paths, one via $SOO(^3A'')$ then SO_2 and one via $SOO(^1A')$, become important at high temperatures. Predicted total rate coefficients agree with experiments throughout the temperature range under investigation. Predicted and reported experimental rate coefficients at high temperatures also agree satisfactorily with those calculated based on the reverse reaction $O + SO$ and equilibrium constants.

ACKNOWLEDGMENTS

Y.P.L. thanks the National Science Council of Taiwan (Grant No. NSC92-2113-M-007-034) and the MOE Program for Promoting Academic Excellence of Universities (Grant No. 89-FA04-AA) for support. R.S.Z. thanks the Office of Naval Research, U.S. Navy (Contract No. N00014-89-

J1949) for support. M.C.L. acknowledges support from the National Science Council of Taiwan for a distinguished visiting professorship.

- ¹R. W. Fair and B. A. Thrush, *Trans. Faraday Soc.* **65**, 1557 (1969).
- ²R. W. Fair, A. van Roodselaar, and O. P. Strausz, *Can. J. Chem.* **49**, 1659 (1971).
- ³D. D. Davis, R. B. Klemm, and M. Pilling, *Int. J. Chem. Kinet.* **4**, 367 (1972).
- ⁴R. J. Donovan and D. J. Little, *Chem. Phys. Lett.* **13**, 488 (1972).
- ⁵M. A. A. Clyne and L. W. Townsend, *Int. J. Chem. Kinet.* **1**, 73 (1976).
- ⁶M. A. A. Clyne and P. D. Whitefield, *J. Chem. Soc., Faraday Trans. 2* **75**, 1327 (1979).
- ⁷A. Miyoshi, H. Shiina, K. Tsuchiya, and H. Matsui, *Symp. Int. Combust. Proc.* **26**, 535 (1996).
- ⁸K. H. Homann, G. Krome, and H. Gg. Wagner, *Ber. Bunsenges. Phys. Chem.* **72**, 998 (1968).
- ⁹D. Woiki and P. Roth, *Int. J. Chem. Kinet.* **27**, 59 (1995).
- ¹⁰K. Saito, Y. Ueda, R. Ito, T. Kakumoto, and A. Imamura, *Int. J. Chem. Kinet.* **18**, 871 (1986).
- ¹¹K. Tsuchiya, K. Kamiya, and H. Matsui, *Int. J. Chem. Kinet.* **29**, 57 (1997).
- ¹²L.-S. Chen, C.-I. Lee, and Y.-P. Lee, *J. Chem. Phys.* **105**, 9454 (1996).
- ¹³J. N. Murrell, W. Craven, and S. C. Farantos, *Mol. Phys.* **49**, 1077 (1983).
- ¹⁴W. Craven and J. N. Murrell, *J. Chem. Soc., Faraday Trans. 2* **83**, 1733 (1987).
- ¹⁵G. Lendvay, G. C. Shatz, and L. B. Harding, *Faraday Discuss.* **102**, 389 (1995).
- ¹⁶S. P. J. Rodrigues and A. J. C. Varandas, *J. Phys. Chem. A* **107**, 5369 (2003).
- ¹⁷A. J. C. Varandas and S. P. J. Rodrigues, *Spectrochim. Acta, Part A* **58**, 629 (2002).
- ¹⁸E. W.-G. Diau and Y.-P. Lee, *J. Chem. Phys.* **96**, 377 (1992).
- ¹⁹L.-H. Lai, Y.-C. Hsu, and Y.-P. Lee, *J. Chem. Phys.* **97**, 3092 (1992).
- ²⁰G. Blake and L. E. Jusinski, *J. Chem. Phys.* **82**, 789 (1985).
- ²¹A. D. Becke, *J. Chem. Phys.* **98**, 5648 (1993); *ibid.* **96**, 2155 (1992); *ibid.* **97**, 9173 (1992).
- ²²C. Lee, W. Yang, and R. G. Parr, *Phys. Rev. B* **37**, 785 (1988).
- ²³A. M. Mebel, K. Morokuma, and M. C. Lin, *J. Chem. Phys.* **103**, 7414 (1995).
- ²⁴C. Gonzalez and H. B. Schlegel, *J. Phys. Chem.* **90**, 2154 (1989).
- ²⁵M. J. Frisch, G. W. Trucks, H. B. Schlegel *et al.*, GAUSSIAN 98, Revision A.9, Gaussian Inc., Pittsburgh, PA, 1998.
- ²⁶MOLPRO is a package of *ab initio* programs written by H.-J. Werner and P. J. Knowles, with contributions from J. Almlöf, R. D. Amos, A. Berning *et al.*
- ²⁷S. J. Klippenstein, A. F. Wagner, R. C. Dunbar, D. M. Wardlaw, and S. H. Robertson, VARIFLEX: Version 1.00, 1999.
- ²⁸R. G. Gilbert and S. C. Smith, *Theory of Unimolecular and Recombination Reactions* (Blackwell Scientific, Carlton, Australia, 1990).
- ²⁹K. A. Holbrook, K. J. Pilling, and S. H. Robertson, *Unimolecular Reactions* (Wiley, Chichester, U.K., 1996).
- ³⁰R. N. Rudolph and E. C. Y. Inn, *J. Geophys. Res., C: Oceans Atmos.* **86**, 9891 (1981).
- ³¹N. Isshiki, Y. Murakami, K. Tsuchiya, A. Tezaki, and H. Matsui, *J. Phys. Chem. A* **107**, 2464 (2003).
- ³²H. Hippler, R. Rahn, and J. Troe, *J. Chem. Phys.* **93**, 6560 (1990).
- ³³K. Schofield, *Combust. Flame* **124**, 137 (2001).
- ³⁴K. Tsuchiya, K. Kamiya, and H. Matsui, *Int. J. Chem. Kinet.* **29**, 57 (1997).
- ³⁵Y. Murakami, S. Onishi, T. Kobayashi, N. Fujii, N. Isshiki, K. Tsuchiya, A. Tezaki, and H. Matsui, *J. Phys. Chem. A* **107**, 10996 (2003).
- ³⁶H. Shiina, M. Oya, K. Yamashita, A. Miyoshi, and H. Matsui, *J. Phys. Chem.* **100**, 2136 (1996).
- ³⁷R. B. Klemm and D. D. Davis, *J. Phys. Chem.* **78**, 1137 (1974).
- ³⁸C.-W. Lu, Y.-J. Wu, Y.-P. Lee, R. S. Zhu, and M. C. Lin, *J. Phys. Chem. A* **107**, 11020 (2003).
- ³⁹M. W. Chase, Jr., *J. Phys. Chem. Ref. Data Monogr.* **9**, 1 (1998).
- ⁴⁰A. Grillo, R. Reed, and M. W. Slack, *J. Chem. Phys.* **70**, 1634 (1979).
- ⁴¹FACSIMILE is a computer software for modeling process and chemical-reaction kinetics released by AEA Technology, Oxfordshire, United Kingdom.
- ⁴²See EPAPS Document No. E-JCPSA6-121-027438 for experimental conditions and values of K_{1a}^1 . A direct link to this document may be found in the online article's HTML reference section. The document may also be reached via the EPAPS homepage (<http://www.aip.org/pubservs/epaps.html>) or from <ftp.aip.org> in the directory /epaps/. See the EPAPS homepage for more information.
- ⁴³T. Shimanouchi, *Tables of Molecular Vibrational Frequencies Consolidated* (National Bureau of Standards, Gaithersburg, MD, 1972), Vol. 1, pp. 1–160.
- ⁴⁴A. G. Hopkins and C. W. Brown, *J. Chem. Phys.* **62**, 2511 (1975).
- ⁴⁵C.-C. Zen, I.-C. Chen, and Y.-P. Lee, *J. Phys. Chem. A* **104**, 771 (2000).
- ⁴⁶C. L. Huang, I.-C. Chen, A. J. Merer, C.-K. Ni, and A. H. Kung, *J. Chem. Phys.* **114**, 1187 (2001).
- ⁴⁷L.-S. Chen, C.-I. Lee, and Y.-P. Lee, *J. Chem. Phys.* **105**, 9454 (1996).
- ⁴⁸C. B. Kellogg and H. F. Schaefer III, *J. Chem. Phys.* **102**, 4177 (1995).
- ⁴⁹T. H. Dunning and R. C. Raffanetti, *J. Am. Chem. Soc.* **85**, 1350 (1981).

Reaction mechanism and kinetics of the NCN + NO reaction: comparison of theory and experiment

Chih-Liang Huang,¹ Shiang Yang Tseng,¹ Tzu Yi Wang,¹ Niann S. Wang,¹ Z. F. Xu and M. C. Lin*^{1,2}

¹*Department of Applied Chemistry and Center for Interdisciplinary Molecular Science, Chiao Tung University, Taiwan 30010*

²*Department of Chemistry, Emory University, Atlanta, GA 30322, USA*

The rate constants for the NCN + NO reaction have been measured by laser photolysis/laser induced fluorescence technique in the temperature range 254 – 353 K in the presence of He (40 – 600 Torr) and N₂ (30 – 528 Torr) buffer gases. The NCN radical was produced from the photodissociation of NCN₃ at 193 nm and monitored with a dye laser at 329.01 nm. The reaction was found to be strongly positive-pressure dependent with negative-temperature dependence, as was reported previously. The experimental data could be reasonably accounted for by dual channel Rice-Ramsperger-Kassel-Marcus calculations based on the predicted potential energy surface using the modified Gaussian-2 method. The reaction is predicted to occur via weak intermediates, cis- and trans-NCNNO, in the ²A'' state which crosses with the ²A' state containing more stable cis- and trans-NCNNO isomers. The high barriers for the fragmentation of these isomers and their trapping in the ²A' state by collisional stabilization give rise to the observed positive pressure dependence and negative temperature effect. The predicted energy barrier for the fragmentation of the cis-NCNNO (²A') to CN + N₂O also allows us to quantitatively account for the rate constant previously measured for the reverse process CN + N₂O → NCN + NO.

*corresponding author: email address: chemmcl@emory.edu

1. INTRODUCTION

The cyanonitrene radical (NCN) is the key product of the new prompt NO reaction occurring in the primary hydrocarbon flame zone^{1,2}



The presence of NCN has recently been confirmed by Smith in a methane-air flame.³ The radical has also been known as an interstellar species.⁴ The kinetics and mechanisms of NCN reactions were non-existent at the time the new prompt NO mechanism was first put forth by Lin and coworkers in 2000.^{1,2} Extensive theoretical calculations for NCN reactions with various combustion species (C, H, CH_x (x =1-3), CN, among others), however, have been reported by Moskaleva in her PhD dissertation.⁵ Most recently, the oxidation of NCN by O₂,⁶ OH and O atoms,⁷ has been studied by high-level ab initio MO/statistical-theory calculations for their rate constants under combustion conditions.

Experimentally, Baren and Hershberger⁸ recently investigated the kinetics of NCN reactions with NO, O₂, C₂H₄ and NO₂ by means of laser-induced fluorescence over the temperature range 298 – 573 K. They reported the rate constants for the reaction NCN + NO at 3, 300, and 600 Torr He and estimated the upper limits of the rate constants for the other radical reactions at 298 K in the 1-3 Torr pressure range. Theoretically, NCN and NO have been shown earlier by Wang et al.⁹ to be the products of the CN + N₂O reaction based on the result of a BAC-MP4 calculation.

In this paper, we report the results of our experimental studies for the NCN + NO

reaction by the laser-induced fluorescence (LIF) technique under varying pressures of He and N₂ in the temperature range 254 – 353 K, aided by a detailed theoretical calculation on the potential energy surface (PES) for the interaction of the ground state NCN (³Σ_g⁻) with the ground state NO (²Π) molecule. Because of the diradical character of NCN (³Σ_g⁻), its interaction with NO may take place over both ²A' and ²A'' surfaces. The effect of the crossing between these two surfaces and the formation of the NCNNO intermediate on the measured rate constants will be examined and the results of our prediction will be compared with the new and existing experimental data.

2. EXPERIMENTAL SECTION

As the system for laser photolysis and LIF that we employed has been described previously,¹⁰ only a brief description is needed here. The reaction cell is a double-walled pyrex flask of volume about 250 ml. Dissociation and probing laser beams were admitted to and exit the cell through two pairs of mutually perpendicular baffled side arms and cross at the center. The fluorescent signal of NCN was collected at a photomultiplier tube (Hamamatsu R1136) through appropriate lenses and an interference filter from the side window perpendicular to the laser beams. The LIF signal was amplified (Hamamatsu C1053, 5 MHz) and averaged with a gated integrator (Stanford Research System, SR250). A microcomputer was used to store and to analyze the collected data.

NCN radicals were produced by photolysis of NCN₃ at 193 nm (ArF) with an excimer laser (Lambda Physik LEXTRA 50). NCN radicals were detected with LIF

by exciting NCN from its $X^3\Sigma_g(0,0^1,0)$ to $A^3\Pi_u(0,2^0,0)$ state at 329.01 nm by means of a doubled output of a Nd-YAG laser (Continuum NY61)-pumped dye laser (Continuum ND60). The fluorescence was collected through an interference filter at 330 nm (FWHM = 10 nm, 15% transmission).

A delay/pulse generator (Stanford Research System, DG535) was used to control the firing of the photolysis and probe lasers, and to initiate the boxcar integrator. Typically 30 - 100 laser shots (at a repetition rate 5 - 10 Hz) were averaged to obtain a single fluorescence data point.

The radical precursor (NCN_3), the molecular reactant (NO) and buffer gas (He, N_2) were mixed in a flexible tubing (30 cm long) before entering the reactor. The reaction mixtures were under slow flow (flow velocity $\sim 10 - 20 \text{ cm s}^{-1}$) conditions such that the reaction zone was replenished with fresh gas for each photolysis laser pulse.

The pressure of the system was measured with a Baratron gauge (MKS 122A). The flow rates of reactants and buffer gas were measured with calibrated mass flowmeters (Tylan FM360). A temperature-controlled fluid was employed by circulating through the jacket of the reactor to maintain a constant reaction temperature ($\pm 2 \text{ K}$), which was measured with a K-type thermocouple placed 5 mm above the detection region. The concentrations of reactants were calculated according to the equation

$$[\text{A}] = 9.66 \times 10^{18} \text{ PF}_\text{A}/\text{F}_\text{T}\text{T} \text{ (molecule cm}^{-3}\text{)}$$

in which P is the reaction pressure (in Torr); T is the reaction temperature (K); F_A

and F_T are the flow rates (in STP cm s^{-1} , STP = 273.15 K, 760 Torr) of reactant A and the total reaction mixture, respectively. The initial concentration of NCN was estimated to be less than 10^{12} radicals/ cm^3 according to the equation

$$[\text{NCN}]_0 = \sigma \times \Phi \times F \times [\text{NCN}_3] \quad (\text{X})$$

in which σ is the absorption cross section of NCN_3 at 193 nm (the value 3.6×10^{-18} cm^2 was used),¹¹ Φ is the quantum yield of NCN from the photolysis (= 1), F is the fluence (photons cm^{-2}) of the dissociation laser.

He (99.999 %) and N_2 (99.999 %) were used without further purification. NO (99.9 %) was purified in freeze-pump-thaw cycles, and diluted in He to a 2% mixture. NCN_3 , prepared by reacting NaN_3 and BrCN overnight,¹¹ was degassed under vacuum and diluted in He or N_2 . This preparation procedure should be handled with extreme care in a well-shielded hood to avoid possible damage caused by explosion which can occur readily for most small azide compounds.

3. COMPUTATIONAL METHODS

The geometric parameters of the reactants, products, transition states, and molecular complexes of the NCN + NO reaction system were optimized at the spin unrestricted B3LYP/6-311+G(d) level of theory.¹² All the stationary points were identified for local minima and transition states by vibrational analysis. Intrinsic reaction coordinate analyses¹³ were performed to confirm the connections of transition states with designated reactants, products or intermediates. In addition, the Complete Active Space Multiconfiguration SCF (MC-SCF) theory¹⁴ was applied to

find the crossing points of the $^2A'$ and $^2A''$ potential energy surfaces by using the conical intersection optimization method.¹⁵ Based on the optimized geometries, higher level single-point energy calculations of the stationary points were performed by the G2M(CC5) method,¹⁶ which calculated the base energy at the MP4/6-311G(d, p) level of theory and improved it with the expanded basis set and the coupled cluster method as well as “higher level corrections (HLC)”. All electronic structure calculations were performed with GAUSSIAN 98 program.¹⁷

The rate constant for the barrierless association reaction producing NCNNO was calculated by the VARIFLEX program¹⁸ based on the microcanonical Rice-Ramsperger-Kassel-Marcus (RRKM) theory.¹⁹ The component rates were evaluated at the E/J-resolved level and the pressure dependence was treated by one-dimensional master equation calculations using the Boltzmann probability of the complex for the J-distribution. For the barrierless association/decomposition process, the fitted Morse function, $V(R) = D_e\{1 - \exp[-\beta(R - R_e)]\}^2$, was used to approximate the minimum potential energy path (MEP) as will be discussed later. Here, D_e is the bonding energy excluding zero-point vibrational energy for an association reaction, R is the reaction coordinate (i.e., the distance between the two bonding atoms), and R_e is the equilibrium value of R at the stable intermediate structure.

The T, P-dependent total rate constants and the branching rate constants for formation of accessible product channels have been computed by the ChemRate program of NIST²⁰ based on the predicted PES. These results will be presented in the following section.

4. RESULTS AND DISCUSSION

A. Rate coefficient measurement

All kinetic measurements were carried out under pseudo-first-order conditions with [NO] more than 200 times as great as that of [NCN]. The initial concentrations for NCN were kept small, $[\text{NCN}]_0 \leq 1 \times 10^{12}$ radicals/cm³, to avoid possible radical-radical reactions and to ensure the pseudo-first-order condition. The rate equation is expressed as

$$-d \ln [\text{NCN}]/dt = k' = k_d + k'' [\text{NO}], \quad (\text{X})$$

in which k' (in s⁻¹) is the first-order decay coefficient, k_d is radical loss rate coefficient mainly due to diffusion from the region of detection and k'' is the second-order reaction-rate coefficient of interest.

The rate coefficient was measured in the temperature range 254-353 K at either 50 – 600 Torr of He or 30 - 528 Torr of N₂, respectively. Figure 1 shows plots of the pseudo-first-order rate coefficient k' vs. [NO] at various pressures of N₂ measured at 298 K. The slopes of the lines give second-order rate coefficients k'' ; N₂ was found to be 1.6 times more efficient as a third body than He. The results of the pressure and temperature dependence experiments are summarized in Table 1. These results will be compared graphically with predicted values later. The values of k'' (in cm³ molecule⁻¹ s⁻¹) obtained at specific He and N₂ pressures can be presented by the Arrhenius equations below:

$$k'' = (7.09 \pm 1.38) \times 10^{-14} \exp [(845 \pm 95)/T] \text{ for 80 Torr He}$$

$$k'' = (5.25 \pm 1.40) \times 10^{-13} \exp [(639 \pm 98)/T] \text{ for 400 Torr He}$$

$$k'' = (8.22 \pm 1.93) \times 10^{-14} \exp [(996 \pm 192)/T] \text{ for 100 Torr N}_2$$

$$k'' = (5.14 \pm 1.22) \times 10^{-13} \exp [(790 \pm 57)/T] \text{ for 400 Torr N}_2.$$

The uncertainty of the reported k'' values represents two standard deviations in the linear least-squares fits.

B. Potential energy surface and reaction mechanism

Figure 2 shows the geometric parameters of both the stationary points and the two crossing points optimized at the B3LYP/6-311+G(d) and the CAS(5,5)/6-311+G(d) methods, respectively. Their vibrational frequencies and the moments of inertia are summarized in Table 2. The relative potential energy diagram obtained at the G2M level based on the optimized structures in Fig. 2 is presented in Fig. 3.

Formation of NCNNO ($^2A''$) intermediates and their isomerization. There are two isomers for the NCNNO ($^2A''$) intermediate (denoted by cis-LM0 and trans-LM0) as indicated in Fig. 2. Their forming processes from the reactants are barrierless as shown in Fig. 3; the energies of cis-LM0 and trans-LM0 at the G2M level are 8.8 and 12.1 kcal/mol, respectively, below the reactants. In addition, as indicated in Table 2, cis-LM0 has a very small torsional vibration frequency, only 9 cm^{-1} and trans-LM0 has a small frequency of 50 cm^{-1} . This implies that both cis- and trans-LM0 have effectively free rotations around the N-N axis. The transition state of the isomerization between cis-LM0 and trans-LM0, iso-TS1, is predicted to be almost equal to that of cis-LM0 at the B3LYP/6-311+G(d) level and become 2.8 kcal/mol lower than that of cis-LM0 at the G2M level. Kinetically, the two isomers are indistinguishable.

Formation of NCNNO ($^2A'$) intermediates and their isomerization. As their $^2A''$ counterparts, NCNNO ($^2A'$) may have cis and trans isomers (denoted as cis-LM1 and trans-LM1). However, they are formed from the reactants NCN + NO via the transition states, cis-TS1 and trans-TS1, as shown in Fig. 3, with relatively high barriers, 7.8 and 7.7 kcal/mol at cis-TS1 and trans-TS1 with the N-N distances of 1.953 Å and 2.011 Å, respectively. Accordingly, the association reaction of NCN with NO over the $^2A'$ PES is rather slow, although cis-LM1 and trans-LM1 are more stable than cis-LM0 and trans-LM0. The relative energies of cis-LM1 and trans-LM1 are predicted to be -31.1 and -22.4 kcal/mol with much shorter N-N distances, 1.243 and 1.262 Å, respectively.

The isomerization between cis-LM1 and trans-LM1 can take place via the iso-TS2 transition state by rotation of the O atom around the N-N bond. In the transition state iso-TS2, the dihedral angle $\angle ONNC$ is 86.1 degree and its energy is -9.6 kcal/mol relative to the reactants (or 12.8 kcal/mol above cis-LM1).

Formation of CN + 1NNO . From Fig. 3, it can be seen that the products CN + 1NNO can be formed by the decomposition of both cis-LM1 and trans-LM1. For the cis-LM1 decomposition channel, the breaking bond C-N is stretched from 1.354 Å at cis-LM1 to 1.906 Å at cis-TS2 and the forward and reverse barriers are 25.7 and 9.0 kcal/mol, respectively. For the trans-LM1 decomposition channel, it is difficult to find the transition state corresponding to the C-N bond breaking in the trans structure. Accordingly, a partial optimization was performed by manually stretching the C-N bond from trans-LM1. The transition state trans-TS2 was found at a rather high

energy of 14.6 kcal/mol relative to the reactants. The breaking C-N bond is elongated from 1.344 Å at trans-LM1 to 1.883 Å at trans-TS2. The forward and reverse barriers are 45.7 and 20.3 kcal/mol, respectively. It is apparent that cis-LM1 should decompose to CN + ¹NNO easier than trans-LM1 does.

Formation of NCO + N₂. NCO and N₂ can be produced by the path from cis-LM1 to the LM2 intermediate via the TS3, followed by the decomposition of LM2 via TS4 to the products as seen in Fig. 3. These transition states and the intermediate are of four-member ring structures. From cis-LM1, the O atom approaches the C atom with the O-N and C-N bonds elongating while the O-C distance shortening to 1.719 Å at TS3 and 1.409 Å at LM2, and the O-N and C-N bonds elongate to 1.467 Å and 1.708 Å, respectively, at TS4. After TS4, as the O-N and C-N bonds break open rapidly, the reaction system is separated into the NCO radical and the N₂ molecule. The energies of TS3, LM2 and TS4 are predicted to be 7.1, -2.4, and 3.2 kcal/mol, respectively, relative to that of the reactants. Although the products, NCO and N₂, have the lowest energy in the PES, it is not more competitive than the formation of the products CN + NNO, because TS3 is predicted to be 3.8 kcal/mol higher than cis-TS2.

Formation of CNO + N₂. The third decomposition channel of cis-LM1 leads to the products CNO + N₂ through LM3, a 5-membered ring intermediate. At the beginning of the decomposition, the O atom of cis-LM1 approaches its terminal N atom to form LM3 via the five-member ring transition state TS5. As seen in Fig. 2, the forming O-N bond length is 1.745 Å at TS5 and 1.378 Å at LM3. The ensuing

decomposition of LM3 proceeds through TS6 to CNO + N₂. The breaking O-N and C-N bonds at TS6 are stretched to 1.975 Å and 1.578 Å, respectively; the relative energies of TS5, LM3, and TS6 are predicted to be 14.8, 5.4, and 16.5 kcal/mol, respectively, above the NCN + NO reactants. Apparently, this reaction channel forming CNO + N₂ cannot compete effectively with other lower energy paths.

Crossing of the ²A'' and ²A' potential surfaces. As suggested by the geometries presented in Fig. 2, the N-N bonds of cis-LM0 and trans-LM0 are 0.551 and 0.394 Å longer than those of cis-LM1 and trans-LM1, respectively, with the concomitant increase in the stabilities from LM0 to LM1. As the N-N bonds are shortened from LM0 to LM1, the ²A'' state may potentially cross over to the ²A' state at energies below the reactants aided by the near free rotation around the N-N bonds. In order to search for the seams of crossing, the minimum energy paths were first traced at the B3LYP/6-311+G(d) level by the IRC method from cis-TS1 and trans-TS1 to cis-LM1 and trans-LM1, respectively, on the ²A' potential surface. Along the IRC, the energy of each structure was calculated again at the ²A'' electronic state to try to locate the point at which the energies at both ²A'' and ²A' states are basically equal. These crossing points were further optimized by the conical intersection optimization method at the CAS(5,5)/6-311+G(d) level of theory. The parameters of the crossing point structures are shown in Fig. 2 where the cis-X structure represents the intersection of the ²A'' and ²A' potential surfaces between cis-LM0 and cis-LM1, and the trans-X structure represents the crossing point between trans-LM0 and trans-LM1.

After an initial test calculation with the ChemRate multi-channel RRKM code of NIST²¹ based on the reaction scheme given above by coupling all intermediates, with and without the cis-trans-isomerization reaction of LM1, we noted that the effect of the isomerization was not significant, particularly under the experimental conditions employed because of the dominant role of the deactivation processes. All subsequent calculations were carried out with the Variflex code,¹⁸ which allows us to examine the effect of multiple reflections²² between the approaching variational transition state, NCN...NO, and the crossing points (cis-X and trans-X) above the LM0 wells. The result of this calculation indicates that the effect of multiple reflections is significant. For example, at 300 Torr He, the reflections reduce the total rate by 29% at 250 K; it drops to 12% at 473 K, then increases to 104% at 1000 K because of the increasing rate of the CN+ N₂O product formation (which reduces the back dissociation effect under collisionally controlled conditions). In this test calculation, the probabilities for crossing at cis-X and trans-X were assumed to be unity, similar to the A'' to A' crossing in the CH₃OO formation and decomposition process in which the free internal rotation of the O-O group was found to promote such a crossing.²³ All subsequent calculations performed with the Variflex code were made with the multiple reflection option.

The vibrational frequencies and moments of inertia of the stationary points employed in the calculations are listed in Table 2. The Lennard-Jones parameters required for the collisional stabilization of the excited NCNNO complex were calculated to be $\varepsilon/k = 201$ K and $\sigma = 4.04$ Å from the He-NCNNO potential curve

computed at the B3LYP/6-311+G(d) level of theory. The Lennard-Jones parameters for He and N₂ are taken from the literature.²⁴ The averaged step-size for energy transfer per collision, $\langle \Delta E \rangle_{\text{down}}$, for He and N₂ are taken to be 110 and 200 cm⁻¹, respectively.

For the barrierless processes NCN + NO → cis-LM0 and trans-LM0, the association potential energy curves were optimized by varying the NCN–NO distances point by point with an interval of 0.1 Å from the equilibrium separations of cis-LM0 and trans-LM0 to 5.0 Å. Morse's β-parameters for the two association processes, obtained by fitting the two computed potential energy curves, are 1.74 Å⁻¹ for the cis channel and 1.65 Å⁻¹ for the trans channel. The Morse potential functions will be used to approximate these two minimum energy paths for the rate constant calculation by the variational transition state approach employed in the Variflex code.

Figure 4 compares the theoretical rate constants predicted in the 250 – 1000 K temperature range for the total rate constants of NCN + NO with the experimental data reported by Baren and Hershberger⁹ and by this study with He and N₂ as buffer gases. The total rate constants for the decay of NCN exhibit a strong negative T-dependence in the middle and low temperature ranges and a strong positive T-dependence at temperatures above 500 K, depending on the pressure of the system. The theoretical rate constants are in reasonable agreement with the experimental results except the data at 3 Torr reported by Baren and Hershberger. The reason for the apparent deviation is not clear.

In Fig. 5 we compare the predicted pressure effect observed at 298 K with He and N₂ as buffer gases. The agreement between experiment and theory is also quite reasonable. The theoretical total rate constants for the NCN+NO reaction can be expressed in units of cm³molecule⁻¹s⁻¹ as follows with 3-parameter equations due to the measured strong non-linear Arrhenius behavior:

At 100 Torr:

$$k''(\text{He}) = 9.62 \times 10^{-6} T^{-3.01} \exp(486/T) \text{ cm}^3 \text{ molecule}^{-1} \text{ s}^{-1} \quad (250 - 600 \text{ K})$$

$$= 7.61 \times 10^{-35} T^{6.69} \exp(3599/T) \text{ cm}^3 \text{ molecule}^{-1} \text{ s}^{-1} \quad (600 - 1000 \text{ K})$$

$$k''(\text{N}_2) = 0.783 T^{-4.57} \exp(-79/T) \text{ cm}^3 \text{ molecule}^{-1} \text{ s}^{-1} \quad (200 - 600 \text{ K})$$

$$= 3.01 \times 10^{-44} T^{9.45} \exp(6174/T) \text{ cm}^3 \text{ molecule}^{-1} \text{ s}^{-1} \quad (600 - 1000 \text{ K})$$

At 400 Torr:

$$k''(\text{He}) = 6.48 \times 10^3 T^{-5.80} \exp(-515/T) \text{ cm}^3 \text{ molecule}^{-1} \text{ s}^{-1} \quad (250 - 600 \text{ K})$$

$$= 1.26 \times 10^{-52} T^{11.90} \exp(8582/T) \text{ cm}^3 \text{ molecule}^{-1} \text{ s}^{-1} \quad (600 - 1000 \text{ K})$$

$$k''(\text{N}_2) = 2.57 \times 10^5 T^{-6.23} \exp(-747/T) \text{ cm}^3 \text{ molecule}^{-1} \text{ s}^{-1} \quad (200 - 600 \text{ K})$$

$$= 7.20 \times 10^{-57} T^{13.08} \exp(10170/T) \text{ cm}^3 \text{ molecule}^{-1} \text{ s}^{-1} \quad (600 - 1000 \text{ K})$$

Figure 6 presents the product branching ratios as a function of temperature based on the theoretical rate constants computed at 400 Torr He pressure. From this figure, we can conclude that below 500 K the dominant product is NCNNO (²A'); however, at T > 800 K the dominant product becomes CN and NNO. With temperature increasing from 500 K to 800 K, the branching ratio of NCNNO (²A') decreases

rapidly with a concomitant increase in CN + NNO formation. Accordingly, in the 500 - 800 K range, both product channels are competitive.

We have also compared in Fig. 7 the predicted rate constant for the reverse reaction, $\text{CN} + \text{NNO} \rightarrow \text{NCN} + \text{NO}$ reported previously by two of the present authors.⁹ The theoretical rate constant predicted with the 9.0 kcal/mol reverse barrier via the cis-LM1 intermediate is seen to agree closely with the experimental values in the experimental temperature range studied. The reaction is predicted to be independent of pressure below 40 atm. The effect of pressure was not examined in our previous study. The theoretical rate constant for this reverse reaction can be expressed in the temperature range 250 – 1000 K by

$$k_r'' = 1.37 \times 10^{-12} T^{0.31} \exp(-4695/T) \text{ cm}^3 \text{ molecule}^{-1} \text{ s}^{-1}$$

4. CONCLUSION

Kinetics and mechanism for the $\text{NCN} + \text{NO}$ reaction have been investigated experimentally and computationally. The reaction was found to be strongly dependent positively on the pressure and negatively on the temperature of the system under the conditions studied. The observed P, T-effects can be reasonably accounted for by the result of a dual-channel RRKM calculation with the predicted mechanism initially taking place via weakly bonded cis- and trans-NCNNO intermediates in the $^2\text{A}''$ state which crosses the $^2\text{A}'$ state to more stable cis- and trans-NCNNO isomers. These isomers can fragment to produce $\text{CN} + \text{N}_2\text{O}$ via two distinct transition states

located at 25.7 and 45.7 kcal/mol above the cis- and trans-isomers, respectively. The predicted rate constant for the reverse $\text{CN} + \text{N}_2\text{O}$ reaction along the dominant, low-energy path via cis-NCNNO to $\text{NCN} + \text{NO}$ agrees closely with previously reported experimental values.

Acknowledgements:

The authors acknowledge the funding of this work by the National Science Council of Taiwan to NCTU for the research and student supports, and to MCL for his distinguished visiting professorship at NCTU. ZFX would like to thank support from the Basic Energy Sciences, US Department of Energy, under contract no. DE-FG02-97-ER14784 and the Cherry L. Emerson Center of Emory University for the use of its resources, which are in part supported by a National Science Foundation grant (CHE-0079627) and an IBM shared University Research Award.

¹L. V. Moskaleva, W. S. Xia and M. C. Lin, *Chem. Phys. Lett.* **331**, 269 (2000).

²L. V. Moskaleva and M. C. Lin, *Proc. Combust. Inst.* **28**, 2393 (2000).

³G. P. Smith, *Chem. Phys. Lett.* **367**, 541 (2003).

⁴C. R. O'dell, C. O. Miller, A. L. Cochran, W. D. Cochran, C. B. Opal, R. S. Barker, *Astrophys. J.* **368**, 616 (1991).

⁵L. V. Moskaleva, PhD. Dissertation, Emory University, 2001.

⁶R. S. Zhu and M. C. Lin, *Int. J. Chem. Kinet.*, submitted.

⁷R. S. Zhu and M. C. Lin, in preparation.

- ⁸R. E. Baren and J. F. Hershberger, *J. Phys. Chem. A* **106**, 11093 (2002).
- ⁹N. S. Wang, D. L. Yang, M. C. Lin and C. F. Melius, *Int. J. Chem. Kinet.* **23**, 151 (1991).
- ¹⁰Y. Y. You and N. S. Wang, *J. Chin. Chem. Soc.* **40**, 337 (1993).
- ¹¹H. Okabe and A. Mele, *J. Chem. Phys.* **51**, 2100.17 (1969).
- ¹²(a) A. D. Becke, *J. Chem. Phys.* **98**, 5648 (1993); (b) A. D. Becke, *J. Chem. Phys.*, **96**, 2155 (1992); (c) A. D. Becke, *J. Chem. Phys.* **97**, 9173 (1992); (d) C. Lee, W. Yang and R. G. Parr, *Phys. Rev.*, **37B**, 785 (1988).
- ¹³(a) C. Gonzalez and H. B. Schlegel, *J. Chem. Phys.* **90**, 2154 (1989); (b) C. Gonzalez and H. B. Schlegel, *J. Phys. Chem.*, **94**, 5523 (1990).
- ¹⁴(a) D. Hegarty and M. A. Robb, *Mol. Phys.* **38**, 1795 (1979). (b) R. H. E. Eade and M. A. Robb, *Chem. Phys. Lett.* **83**, 362 (1981). (c) H. B. Schlegel and M. A. Robb, *Chem. Phys. Lett.* **93**, 43 (1982). (d) F. Bernardi, A. Bottini, J. J. W. McDougall, M. A. Robb, and H. B. Schlegel, *Far. Symp. Chem. Soc.* **19**, 137 (1984). (e) N. Yamamoto, T. Vreven, M. A. Robb, M. J. Frisch, and H. B. Schlegel, *Chem. Phys. Lett.* **250**, 373 (1996). (f) M. J. Frisch, I. N. Ragazos, M. A. Robb, and H. B. Schlegel, *Chem. Phys. Lett.* **189**, 524 (1992).
- ¹⁵(a) M. J. Bearpark, M. A. Robb, and H. B. Schlegel, *Chem. Phys. Lett.* **223**, 269 (1994).. (b) I. N. Ragazos, M. A. Robb, F. Bernardi, and M. Olivucci, *Chem. Phys. Lett.* **197**, 217 (1992). (c) F. Bernardi, M. A. Robb, and M. Olivucci, *Chem. Soc. Reviews* **25**, 321 (1996).
- ¹⁶A. M. Mebel, K. Morokuma, and M. C. Lin, *J. Chem. Phys.* **103**, 7414 (1995).

- ¹⁷M. J. Frisch, G. W. Trucks, H. B. Schlegel, G. E. Scuseria, M. A. Robb, J. R. Cheeseman, V. G. Zakrzewski, J. A. Montgomery, Jr., R. E. Stratmann, J. C. Burant, S. Dapprich, J. M. Millam, A. D. Daniels, K. N. Kudin, M. C. Strain, O. Farkas, J. Tomasi, V. Barone, M. Cossi, R. Cammi, B. Mennucci, C. Pomelli, C. Adamo, S. Clifford, J. Ochterski, G. A. Petersson, P. Y. Ayala, Q. Cui, K. Morokuma, D. K. Malick, A. D. Rabuck, K. Raghavachari, J. B. Foresman, J. Cioslowski, J. V. Ortiz, A. G. Baboul, B. B. Stefanov, G. Liu, A. Liashenko, P. Piskorz, I. Komaromi, R. Gomperts, R. L. Martin, D. J. Fox, T. Keith, M. A. Al-Laham, C. Y. Peng, A. Nanayakkara, C. Gonzalez, M. Challacombe, P. M. W. Gill, B. G. Johnson, W. Chen, M. W. Wong, J. L. Andres, M. Head-Gordon, E. S. Replogle and J. A. Pople, GAUSSIAN 98 Revision A.9, Gaussian, Inc., Pittsburgh PA, 1998.
- ¹⁸S. J. Klippenstein, A. F. Wagner, R. C. Dunbar, D. M. Wardlaw, and S. H. Robertson, VARIFLEX Version 1.00, 1999.
- ¹⁹D. M. Wardlaw and R. A. Marcus, Chem. Phys. Lett. **110**, 230 (1984); J. Chem. Phys. **83**, 3462 (1985). S. J. Klippenstein, J. Chem. Phys. **96**, 367 (1992); S. J. Klippenstein and R. A. Marcus, J. Chem. Phys. **87**, 3410 (1987).
- ²⁰H. Hippler, J. Troe, and H. J. Wendelken, J. Chem. Phys. **78**, 6709 (1983).
- ²¹V. Mokrushin, V. Bedanov, W. Tsang, M. R. Zachariah, and V. D. Knyazev, CHEMRATE Version 1.19; National Institute of Standards and Technology: Gaithersburg, MD 20899, 2002.
- ²²S. J. Klippenstein, D. L. Yang, T. Yu, S. Kristyan and M. C. Lin, J. Phys. Chem. A **102**, 6973 (1998).

- ²³R. S. Zhu, C.-C. Hsu, and M. C. Lin, *J. Chem. Phys.* **115**, 195 (2001).
- ²⁴J. O. Hirschfelder, C. F. Curtiss, and R. B. Bird, *Molecular theory of gases and liquids 2nd^{ed}*, John Wiley and Sons Inc., New York, NY, 1964.
- ²⁵D. E. Milligan, M. E. Jacox, *J. Chem. Phys.* **45**, 1387 (1966)
- ²⁶K. P. Huber and G. Herzberg, *Molecular Spectra and Molecular Structure. IV. Constants of Diatomic Molecules*, Van Nostrand Reinhold Company, New York, 1979,
- ²⁷T. Shimanouchi, *Tables of Molecular Vibrational Frequencies Consolidated Volume I*, National Bureau of Standards, 1972, 1-160

TABLE 1. Experimental conditions and rate coefficients of the reaction NCN+NO

T	P	[NO]	k	T	P	[NO]	k
			$/ 10^{-12} \text{ cm}^3$				
/ K	/ Torr	$/(10^{14} \text{ molecule cm}^{-3})$	$\text{molecule}^{-1} \text{ s}^{-1}$	/ K	/ Torr	$/(10^{14} \text{ molecule cm}^{-3})$	$/10^{-12} \text{ cm}^3 \text{ molecule}^{-1} \text{ s}^{-1}$
254(He)	80	1.24~6.69	2.11 ± 0.13	259(N ₂)	50	1.22~5.83	2.29 ± 0.13
	158	3.60~18.5	3.13 ± 0.19		100	1.32~8.52	4.34 ± 0.18
	265	2.74~17.6	4.92 ± 0.32		150	1.93~13.9	6.68 ± 0.57
	381	2.65~19.0	5.05 ± 0.25		217	1.91~18.8	7.16 ± 0.38
	400	1.64~10.6	6.14 ± 0.23		254	1.41~15.0	7.78 ± 0.30
	513	3.11~19.2	8.14 ± 0.43		400	1.14~14.6	10.48 ± 0.52
278(He)	82	1.27~7.93	1.39 ± 0.09	278(N ₂)	101	0.66~6.99	2.75 ± 0.15
	423	2.16~11.5	5.58 ± 0.29		397	1.31~13.1	9.25 ± 0.59
298(He)	40	1.13~9.45	0.98 ± 0.12	298(N ₂)	30	4.80~0.96	1.21 ± 0.08
	80	1.34~9.13	1.16 ± 0.07		50	5.35~0.49	1.44 ± 0.04
	150	3.82~10.0	2.37 ± 0.25		100	7.59~0.63	2.05 ± 0.09
	200	1.60~9.15	3.42 ± 0.29		150	1.23~7.68	2.65 ± 0.14
	300	1.30~11.8	4.49 ± 0.90		198	1.13~12.9	4.15 ± 0.23
	400	2.43~9.98	4.83 ± 0.88		253	1.76~16.4	4.52 ± 0.22
	500	1.00~8.76	4.99 ± 1.09		300	1.20~16.4	6.42 ± 0.24
	600	1.40~8.41	4.81 ± 0.74		400	1.28~18.5	7.38 ± 0.59
353(He)	83	0.57~4.90	0.81 ± 0.02		528	1.45~12.7	8.09 ± 0.65
	394	0.92~8.68	3.05 ± 0.19	353(N ₂)	102	0.55~6.40	1.50 ± 0.05
					401	1.29~10.2	4.74 ± 0.30

^aError limits are 2σ

TABLE 2. Moments of inertia and frequencies of the stationary points calculated at the B3LYP/6-311+G(d) level.

Species	I_a, I_b, I_c (a.u.)	Frequencies (cm^{-1})
NCN ($^3\Sigma_g$)	150.3, 150.3	440, 440, 1272, 1563 (423, 423, 1197, 1475) ^a
NO ($^2\Pi$)	35.1, 35.1	1980 (1904) ^b
NNO ($^1\Sigma$)	142.7, 142.7	580, 580, 1326, 2344 (589, 589, 1285, 2224) ^c
CN ($^2\Sigma$)	31.3, 31.3	2146 (2068) ^b
cis-LM0	132.6, 425.6, 558.3	9, 124, 268, 449, 573, 714, 1212, 1837, 1918
trans-LM0	42.6, 647.7, 690.3	50, 170, 279, 453, 570, 732, 1203, 1808, 1907
cis-LM1	90.9, 473.8, 564.8	164, 331, 464, 553, 805, 924, 1310, 1685, 2309
trans-LM1	22.4, 650.6, 673.0	203, 242, 521, 545, 637, 1028, 1345, 1681, 2319
LM2	110.7, 288.0, 398.7	257, 396, 627, 735, 758, 936, 1064, 1513, 1726
LM3	145.8, 178.5, 324.3	595, 616, 681, 837, 969, 1025, 1116, 1384, 1495
iso-TS1	131.3, 429.2, 559.7	<i>i</i> 41, 133, 266, 448, 574, 711, 1208, 1836, 1917
iso-TS2	51.6, 594.5, 632.0	<i>i</i> 459, 147, 402, 479, 634, 863, 1330, 1649, 2202
cis-TS1	104.1, 597.4, 701.6	<i>i</i> 354, 84, 216, 396, 489, 566, 1227, 1710, 1893
trans-TS1	39.8, 819.4, 859.3	<i>i</i> 284, 101, 162, 375, 497, 545, 1247, 1688, 1924
cis-TS2	58.9, 732.4, 791.3	<i>i</i> 367, 66, 87, 240, 516, 569, 1278, 2150, 2201
trans-TS2	44.5, 760.3, 804.8	<i>i</i> 637, 124, 264, 375, 426, 616, 1195, 1769, 2216
TS3	112.7, 309.2, 422.0	<i>i</i> 698, 257, 333, 671, 699, 949, 1019, 1484, 1840
TS4	112.3, 309.7, 422.1	<i>i</i> 771, 271, 329, 618, 632, 754, 979, 1579, 1878
TS5	153.9, 192.7, 346.6	<i>i</i> 552, 507, 657, 759, 954, 990, 1047, 1395, 1670
TS6	145.1, 244.0, 389.2	<i>i</i> 662, 115, 335, 480, 666, 813, 1212, 1332, 1884
cis-X ^d	106.0, 418.5, 524.6	<i>i</i> 261, 123, 404, 435, 788, 859, 1139, 1987, 2433

trans-X^d 40.0, 629.5, 669.6 *i*315, 157, 301, 478, 564, 765, 1107, 1994, 2526

^aRef. 25.

^bRef. 26.

^cRef. 27

^dCalculated at the CAS(5,5)/6-311+(d) level of theory.

FIGURE CAPTIONS

Figure 1. Plots of the pseudo-first-order decay rate of NCN, k' vs [NO] at 298 K, at various pressure of N₂ (Torr): (■) 30 ; (□) 150; (●) 253; (○) 528.

Figure 2. Geometries of the reactants, products, intermediates and transition states (Å and degree) optimized at the B3LYP/6-311+G(d) level except the cis-X and trans-X crossing points which are optimized at the CAS(5,5)/6-311+(d) level with the conical intersection method.

Figure 3. Energy diagram of the NCN + NO system calculated at the G2M level.
 $E(\text{NCN}) = -147.271877$ Hartrees and $E(\text{NO}) = -129.738203$ Hartrees.

Figure 4. Plots of the rate constants for the NCN + NO reaction as a function of reciprocal temperature. (a) He buffer gas; (b) N₂ buffer gas.

Figure 5. Plots of the rate constants for the NCN + NO reaction at 298 K as a function of pressure at 298 K. (a) He buffer gas; (b) N₂ buffer gas.

Figure 6. Theoretical branching ratios as functions of temperature for the individual products in the NCN + NO reaction at the 400 Torr He pressure producing N₂O + CN and NCNNO by collisional deactivation.

Figure 7. Plot of the rate constant for the reverse reaction, CN + NNO → NCN + NO.

^aRef. 9

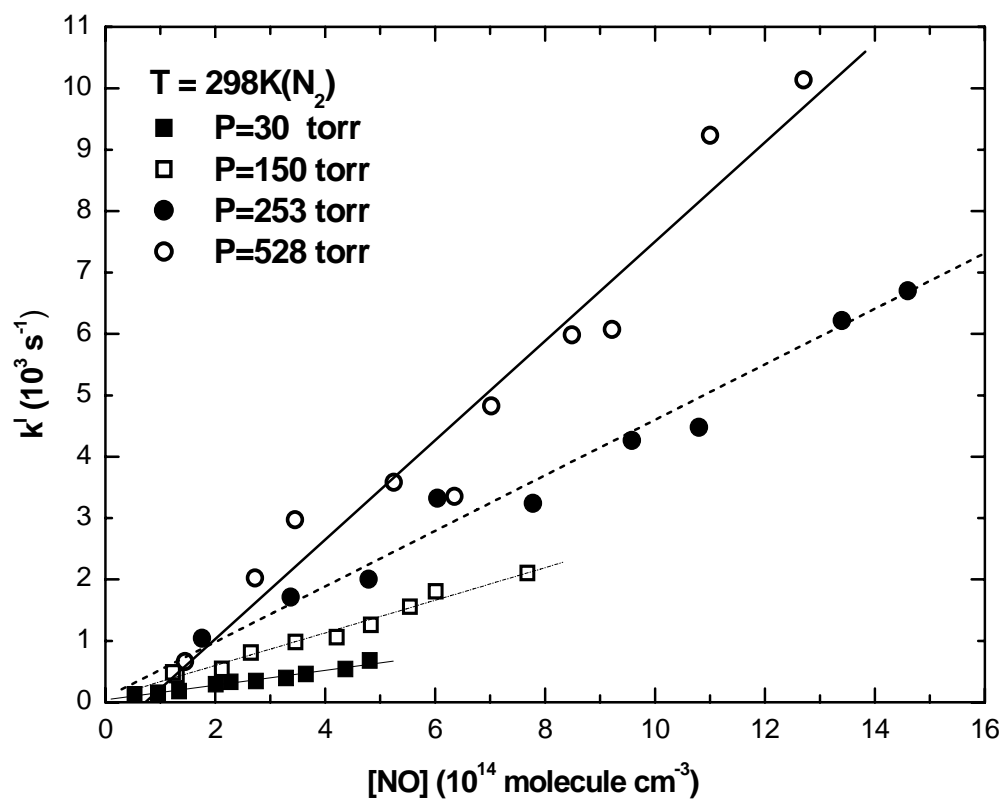


Fig. 1

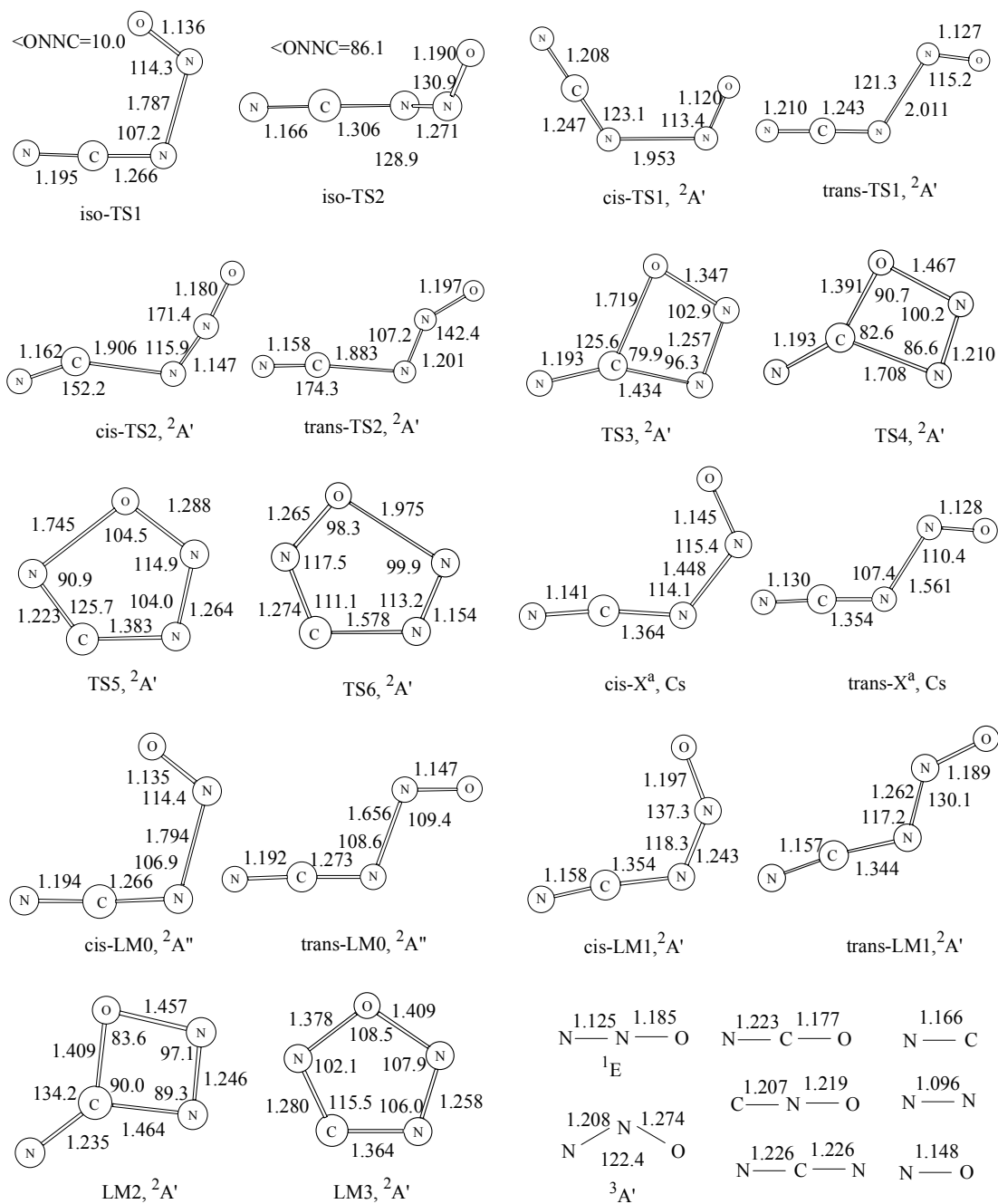


Fig. 2

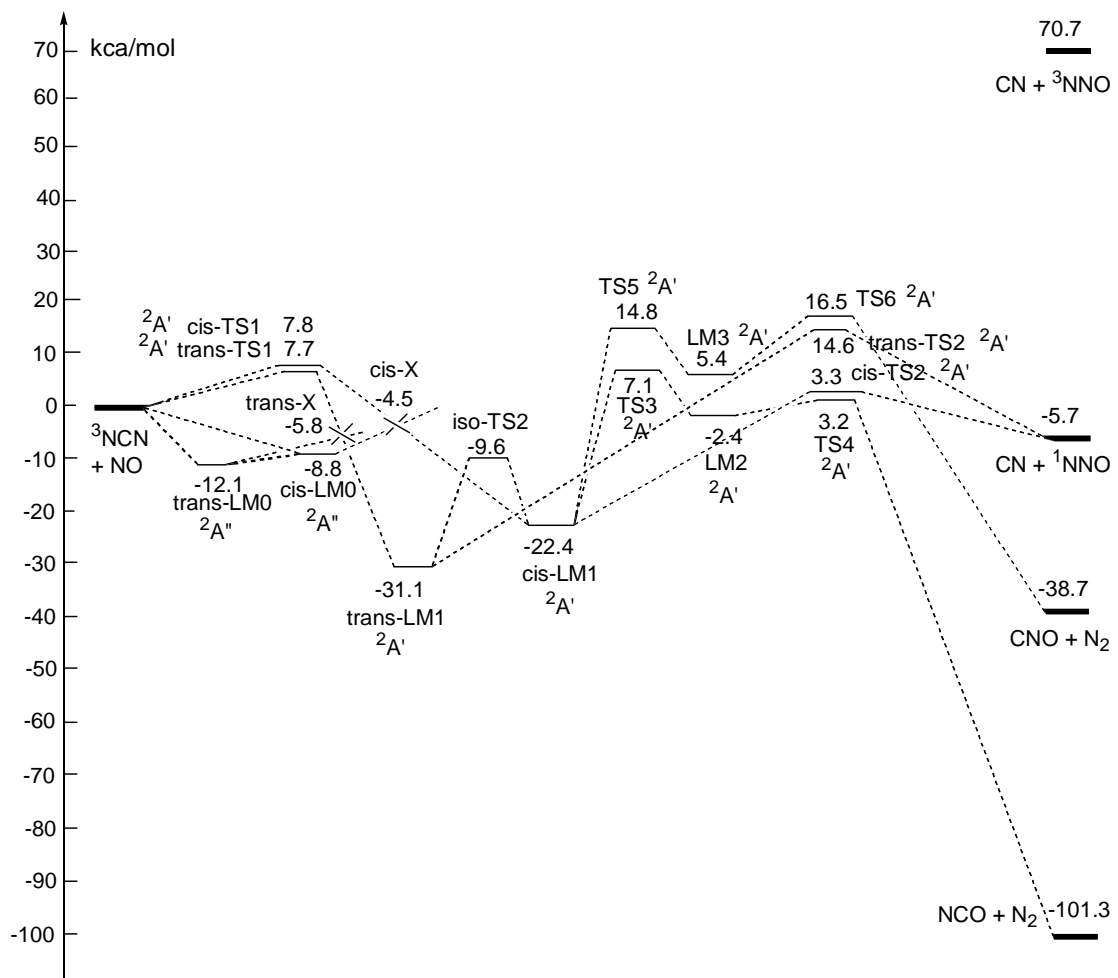


Fig. 3

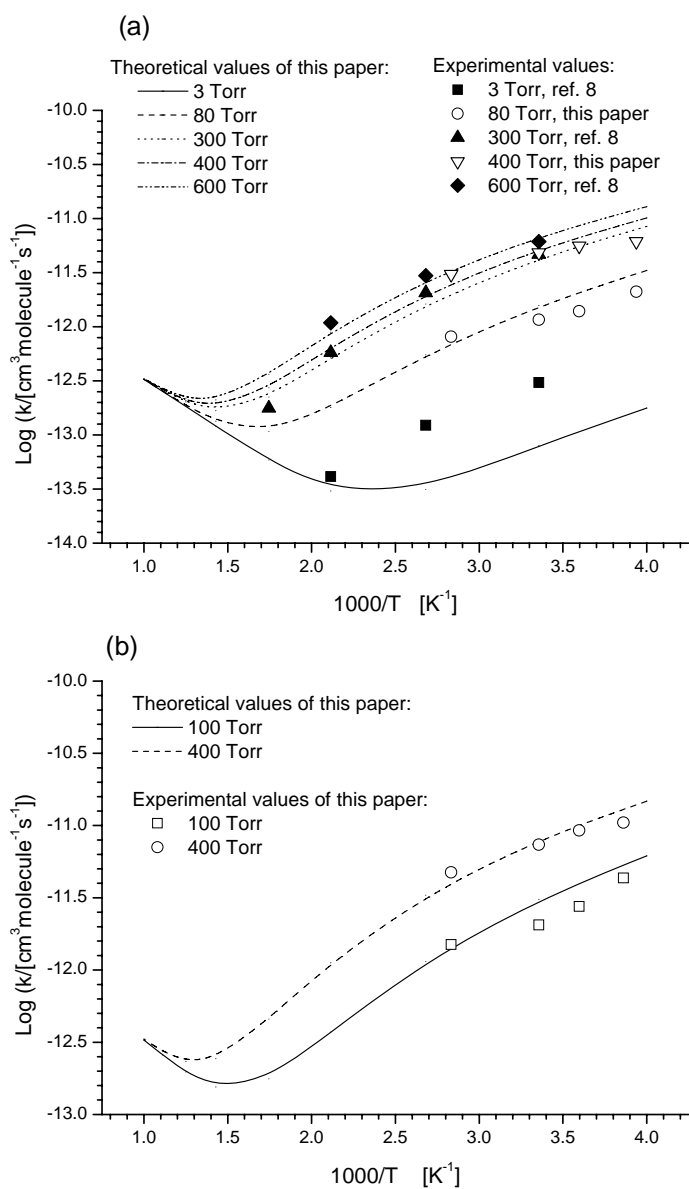


Fig. 4

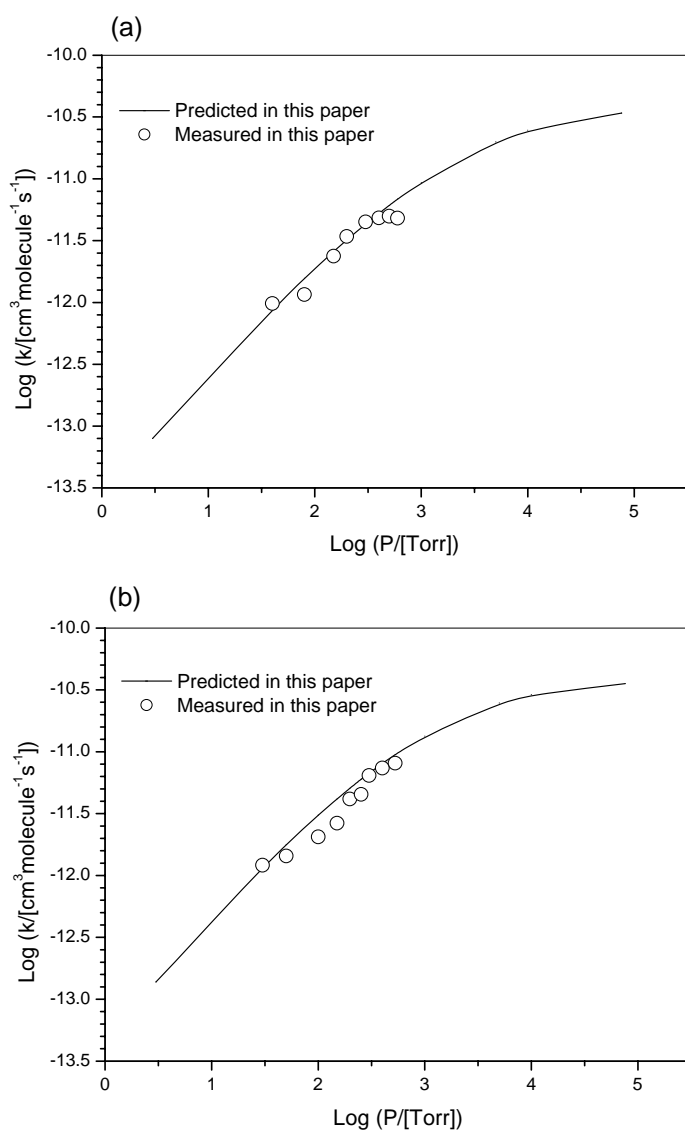


Fig. 5

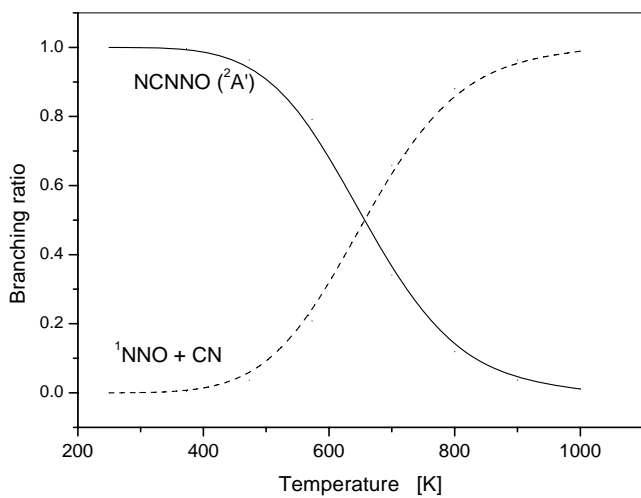


Fig. 6

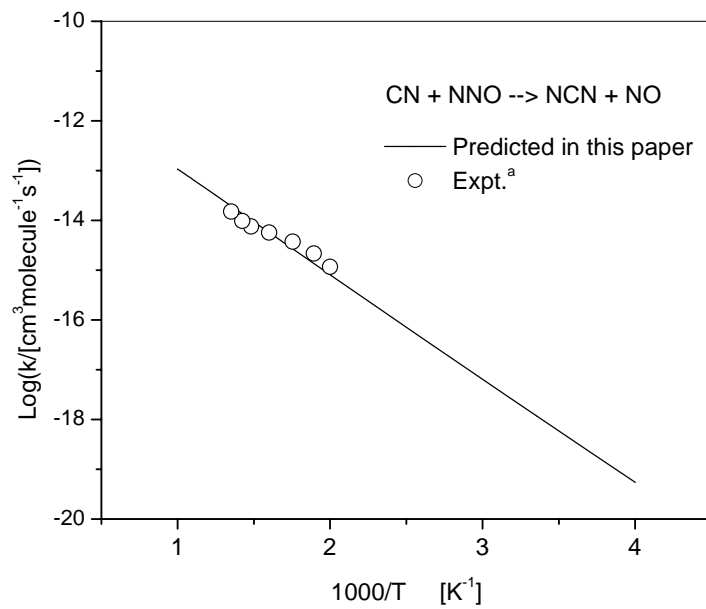


Fig. 7

**Experimental and theoretical studies of rate coefficients
for the reaction $O(^3P) + CH_3OH$ at high temperatures**

Chih-Wei Lu and Shen-Long Chou

*Department of Chemistry, National Tsing Hua University,
101, Sec. 2, Kuang Fu Road, Hsinchu 30013, Taiwan*

Yuan-Pern Lee*

*Department of Applied Chemistry and Institute of Molecular Science,
National Chiao Tung University, 1001, Ta Hsueh Road, Hsinchu 30010, Taiwan
and Institute of Atomic and Molecular Sciences, Academia Sinica, Taipei 106, Taiwan*

Shucheng Xu, Z. F. Xu and M. C. Lin* ^a

Department of Chemistry, Emory University, Atlanta, GA 30322, USA

(Received xx February 2005; accepted xx xxxx 2005)

*Corresponding authors. Y.-P. Lee: E-Mail: yplee@mail.nctu.edu.tw; FAX: 886-3-5713491.
M.C. Lin: chemmcl@emory.edu; FAX: 1-404-727-6586.

^aNational Science Council Distinguished Visiting Professor at the Center for Interdisciplinary Molecular Science, National Chiao Tung University, Taiwan.

ABSTRACT

Rate coefficients of the reaction $\text{O}({}^3\text{P}) + \text{CH}_3\text{OH}$ in the temperature range 835–1777 K were determined using a diaphragmless shock tube. O atoms were generated by photolysis of SO_2 with a KrF excimer laser at 248 nm or an ArF excimer laser at 193 nm; their concentrations were monitored via atomic resonance absorption excited by emission from a microwave-discharged mixture of O_2 and He. Rate coefficients determined for the temperature range can be represented by the Arrhenius equation: $k(T) = (2.29 \pm 0.18) \times 10^{-10} \exp[-(4210 \pm 100)/T] \text{ cm}^3 \text{ molecule}^{-1} \text{ s}^{-1}$; unless otherwise noted, all listed errors represent one standard deviation in fitting. Combination of these and previous data at lower temperature shows a non-Arrhenius behavior described as the three-parameter equation $k(T) = (2.74 \pm 0.07) \times 10^{-18} T^{2.25 \pm 0.13} \exp[-(1500 \pm 90)/T] \text{ cm}^3 \text{ molecule}^{-1} \text{ s}^{-1}$. Theoretical calculations at the B3LYP/6-311+G(3df, 2p) level locate three transition states. Based on the energies computed with CCSD(T)/6-311+G(3df, 2p)//B3LYP/6-311+G(3df, 2p), rate coefficients predicted with canonical variational transition state theory with small curvature tunneling corrections agree satisfactorily with experimental observations. The branching ratios of two accessible reaction channels forming $\text{CH}_2\text{OH} + \text{OH}$ (1a) and $\text{CH}_3\text{O} + \text{OH}$ (1b) are predicted to vary strongly with temperature. At 300 K, reaction (1a) dominates, whereas reaction (1b) becomes more important than reaction (1a) above 1700 K.

I. INTRODUCTION

Methanol (CH_3OH) is considered as an important alternative fuel; it may be used directly in an internal engine via combustion or in a fuel cell via catalytic electrolytic reactions. The reaction



with 3 energetically accessible channels is one of the most important processes in combustion of CH_3OH . The branching between these channels plays an important role in the formation of the end products, inhibition of flames, and formation of soot.¹

Rate coefficients of reaction (1) have been determined in the temperature range 273–1006 K by several groups.^{2–9} Experimental conditions, reported rate coefficients near room temperature and Arrhenius parameters of these studies are listed in Table I for comparison; the corresponding Arrhenius plots are also shown in Fig. 1. Most rate coefficients are reported to be within a factor of two except those of LeFevre *et al.* (designated LMT)² and Basevich *et al.* (designated BKF)³ which are 4–17 times greater near 298 K, and those of Avramenko *et al.* (designated AKK)⁸ which are about 3 times smaller. Rate coefficients of this reaction show a non-Arrhenius behavior, as reported activation energies increases with the temperature of measurements. The two measurements covering limited temperature range below 450 K by LMT² and by Owens and Roscoe (designated OR)⁴ have activation energies ($E_a/R = 1150$ and 1540 K, respectively) smaller than the two reports of $E_a/R \cong 2640 \pm 110$ K by Keil *et al.* (designated KTSKM)⁵ and Grotheer and Just (designated GJ)⁶ covering temperatures up to ~1000 K. Experiments in the intermediate temperature range of 297–544 K by Failes *et al.* (designated FSPI)⁷ yields an intermediate value of $E_a/R = 2270 \pm 110$ K.

Although the two sets of experiments by KTSKM⁵ and GJ⁶ at high temperatures show similar values of E_a/R (2530 ± 80 and 2750 ± 150 K, respectively), rate coefficients vary by as much as 1.7 times at 1000 K partly because of variations in Arrhenius pre-exponential factors (2.7×10^{-11} and 5.7×10^{-11} $\text{cm}^3 \text{ molecule}^{-1} \text{ s}^{-1}$, respectively).^{5,6} Experimental data are lacking

for temperatures above 1006 K.

To the best of our knowledge, there have been no high-level quantum-chemical calculations performed for the O + CH₃OH system. Tsang¹⁰ combined existing experimental data with a transition state theory using BEBO (bond-energy-bond-order) approximations and predicted the temperature dependence of the rate coefficient to be

$$k_1 = 6.44 \times 10^{-19} T^{2.50} \exp [-(1550/T)] \text{ cm}^3 \text{ molecule}^{-1} \text{ s}^{-1} \quad (2)$$

The rate coefficient is predicted to increase rapidly at temperatures above 1000 K, yielding an upward curved Arrhenius plot.

Because of the importance of this reaction in combustion, kinetic data at higher temperatures are needed. We have determined rate coefficients of the title reaction up to 1777 K with a diaphragmless shock tube. We also performed theoretical calculations on this reaction to compare with our experimental measurements and to understand the competition between the two channels at varied temperatures.

II. EXPERIMENTS

Details of the diaphragmless shock tube apparatus have been described previously.^{11, 12} The shock tube (length 5.9 m and i.d. 7.6 cm) is coupled to a detection system using atomic resonance absorption. The speed of the shock wave were determined with pressure sensors and time-frequency counters. A microwave-discharged lamp with a flowing gas mixture of ~1 % O₂ in He served as a light source for atomic absorption of O atoms. Emission at 130.23, 130.49, and 130.60 nm, corresponding to atomic transitions of O(³S-³P_{2, 1, 0}), passes perpendicularly near the end of the shock tube and a vacuum UV monochromator (reciprocal linear dispersion 4.0 nm mm⁻¹, slit width 350 μm) before being detected with a solar-blind photomultiplier tube (PMT). Variation of the signal from the PMT was monitored with a digital storage oscilloscope and transferred to a computer for further processing.

For kinetic measurements, O atoms were generated from laser photolysis of SO₂ at 248 nm or 193 nm. At 248 nm, absorption cross section of SO₂ is 7.7 × 10⁻²⁰ cm² at 1100 K and 5.3 × 10⁻¹⁹ cm² at 2000 K.¹³ At 193 nm, absorption cross section of SO₂ is 3.4 × 10⁻¹⁸ cm² at

1100 K and $2.8 \times 10^{-18} \text{ cm}^2$ at 2000 K.¹³ Light from the ArF excimer laser at 193 nm (or KrF excimer laser at 248 nm) enters the shock tube from the quartz end-plate and passes along the tube. A pulse generator was employed to trigger the laser about 150–200 μs after the arrival of the incident shock wave at the last pressure sensor.

Before each experiment, the system was pumped below 5.0×10^{-7} Torr. The temperature (T_5), density (ρ_5), and pressure (P_5) in the reflected shock regime were calculated from measured velocity of the incident shock, the composition of the test gas, the initial pressure, and the temperature using the ideal shock-wave theory¹⁴ with Mirels' boundary layer corrections.^{15, 16}

We calibrated the concentration of O atoms in the shock tube with pyrolysis of N_2O , assuming a 100% yield of O atoms.¹⁷ The concentration of O atoms is fitted with the equation

$$[\text{O}] / 10^{13} \text{ molecule cm}^{-3} = 4.4233 A - 0.0336 A^2 + 2.5741 A^3 \quad (3)$$

in which absorbance A is calculated with the equation

$$A = \ln(I_0 / I), \quad (4)$$

in which the light intensity before and after production of O atoms is denoted as I_0 and I , respectively.

He (99.9995 %, AGA Specialty Gases), Ar (99.9995 %, AGA Specialty Gases), N_2O (99 %, Scott Specialty Gases), O_2 (99.999 %, Scott Specialty Gases), and SO_2 (99.98 %, Matheson) were used without further purification. CH_3OH (99.9 %, Mallinckrodt, Analytical Reagent grade) was purified by passing the vapor through P_2O_5 to remove trace water impurity. Mixtures of CH_3OH in Ar (100–500 ppm) and SO_2 in Ar (100–900 ppm) were used.

III. COMPUTATIONAL METHODS

The geometry of reactants, transition states, and products of the $\text{O} + \text{CH}_3\text{OH}$ system were optimized at the B3LYP/6-311+G(3df, 2p) level of theory with Becke's three-parameter non-local exchange functional¹⁸ and the non-local correlation functional of Lee *et al.*¹⁹ Single-point energies of all species were calculated with the CCSD(T)/6-311+G(3df, 2p) method,²⁰ based on the optimized geometries at the B3LYP/6-311+G(3df, 2p) level.

Rate coefficients were calculated with conventional transition state theory (TST),

canonical variational transition state theory (CVT) with zero curvature tunneling corrections (ZCT) and small curvature tunneling corrections (SCT) using the POLYRATE program of Truhlar *et al.*²¹

All calculations were carried out with Gaussian 03²² programs using a PC cluster and the computers at the Emerson Computation Center of Emory University.

IV. RESULTS AND DISCUSSION

A. Rate coefficient k_1 for O + CH₃OH

Experiments were carried out under pseudo-first-order conditions with $[\text{CH}_3\text{OH}]_0 \gg [\text{O}]$. Figure 2 shows a typical temporal profile recorded for the mixture containing SO₂, CH₃OH, and Ar after laser photolysis at 193 nm. The concentration of O atoms at reaction period t , $[\text{O}]_t$, is derived according to Eqs. (3) and (4). $[\text{O}]_t$ follows an exponential decay in the initial stage. The apparent pseudo-first-order rate coefficient k^1 is derived with the equation

$$\ln([\text{O}]_t/[\text{O}]_0) = -k^1 t + a t^2 - b t^3 \quad (5)$$

in which t is the reaction time and a and b are fitting parameters to account for deviation from the exponential decay due to secondary reactions. The apparent bimolecular rate coefficient, k_1' , is thus derived from

$$k_1' = k^1 / [\text{CH}_3\text{OH}]_0 \quad (6)$$

Comparison of k_1' with the true bimolecular rate coefficient k_1 provides information on the extent of interference due to secondary reactions.

At low temperature, previously observed deuterium isotopic effects on rate coefficient indicate that reaction (1) is dominated by channel (1a). Grotheer and Just⁶ observed similar apparent decay rates for reactions of O + CH₃OH and O + CH₃OD at 305 K, which are ~8 times greater than those of O + CD₃OH and O + CD₃OD, indicating that the main reaction channel is the abstraction of the H atom of the methyl group. However, as temperature increases, reaction (1b) may become important. Our theoretical calculations (discussed in Sec. IV-C) show that reaction (1c) is unimportant under our experimental conditions and the branching ratio of reaction (1b) increases from ~0.13 at 300K to ~0.5 at 1700 K. Because we

are only probing the decay of [O] and cannot distinguish between channels (1a) and (1b), we employed branching ratios calculated theoretically in this work in the model to derive the total decay coefficient.

Photolysis of SO₂ at 193 nm is more efficient in generating O atoms, thus enabling us to use smaller concentrations of SO₂. However, irradiation of CH₃OH with light at 193 nm produces CH₃O and H.²³ Effect of CH₃O production on the decay of [O] was examined by employing photolysis laser at 248 nm, at which wavelength photolysis of CH₃OH is negligible. We estimate the photolysis yield by the following equation:

$$[\text{CH}_3\text{O}]_0 = \sigma \times F \times [\text{CH}_3\text{OH}] \times \phi \quad (7)$$

in which σ is the cross section (cm² molecule⁻¹) of CH₃OH,²⁴ F is the fluence (photons cm⁻²) of the laser, and ϕ is the photolysis yield.²³ No significant variations in derived rate coefficients were observed for photolysis of SO₂ at 193 and 248 nm.

Several interference reactions need to be considered. At high temperatures, pyrolysis of CH₃OH is non-negligible.¹⁰ According to modeling, at 1777 K and [CH₃OH]₀ = 5.95 × 10¹⁴, [SO₂]₀ = 2.95 × 10¹⁵, [Ar] = 5.91 × 10¹⁸ molecule cm⁻³, about one half of CH₃OH decomposes within 90 μs.



The products CH₂OH and CH₃ react rapidly with O atoms



Hence, subsequent reactions involving H and OH need to be considered.

Because we used SO₂ as the source of O atoms, reactions involving SO, SO₂, and SO₃ should also be considered.



We modeled observed temporal profiles of [O] with a commercial kinetic modeling

program FACSIMILE.²⁵ The model employed is listed in Table II; it is basically a simplified version of that employed by Held and Dryer¹ with additional reactions involving S, SO_x and CH₃. The rate coefficients are obtained from the literature unless noted.

Because the laser was triggered about 50–100 μ s after arrival of the reflected shock wave at the observation zone, pyrolysis of CH₃OH before generation of O atoms should be taken into account, especially at high temperature. We modeled these reactions in two separate periods: the first period started from the arrival of the reflected shock wave and ended with the arrival of the photolysis laser pulse, and the second period started on arrival of the photolysis laser pulse. In the first period, we used [O] = 0 to derive concentrations of all reactants and intermediates at the end of this period, which were then employed in the second period, along with experimentally observed concentration of laser-produced O atoms, to model the temporal profile of [O]. In the fitting, the branching ratio of the title reaction calculated quantum-chemically in this work and literature values of rate coefficients of all reactions except the title reaction k_1 were held constant, and the bimolecular rate coefficient k_1 was varied to yield the best fit.

Experimental conditions and values of k_1 for 44 measurements in a temperature range 835–1777 K using mixtures of various concentrations of CH₃OH and SO₂ are summarized in Table III. We list k_1'/k_1 in Table III for comparison; values of k_1' obtained with Eq. (6) from pseudo-first-order decays are greater than k_1 , by factors as much as 2.4 at high temperatures, indicating that interference reactions are non-negligible.

Sensitivity analysis shows that rate coefficient of the title reaction is most sensitive to variations of rate coefficients of reactions (12a) and (32) at low temperatures, and reactions (8a), (10), (27), (28a), (32), (33) and (50) at high temperatures. In the extreme case that one of the above reactions was neglected in the modeling, we found that rate coefficient k_1 would increase by as much as 2.7 times.

Some representative decays curves covering the whole temperature range of study were also modeled with a complete model consisting of 89 reactions employed by Held and Dryer¹, 8 reactions involving sulfur compounds, and 8 additional reactions (reactions 26b, 27, 28a, 28b, 29b, 35b, 48b, and 50) not included in the model of Held and Dryer.¹ Derived rate

coefficients are similar to those listed in Table III using our model, with deviations less than 18 %.

We tested the effect of branching ratio $k_{1a}/(k_{1a}+k_{1b})$ on derived total rate coefficient k_1 and found that derived rate coefficient k_1 are insensitive to the branching ratio at all temperatures. Presumably this is because secondary reactions associated with CH_3O and CH_2OH have similar effects on the decay of O atoms. We also tested the effect of pyrolysis of CH_3OH before its reaction with O atoms. Pyrolysis of CH_3OH has two counteractive effects: the decrease in $[\text{CH}_3\text{OH}]$ and effects due to secondary reactions involving pyrolysis products CH_3 , OH , CH_2OH , and H . At temperatures below 1650 K, when we took out the simulation of the first period (i. e., to assume that pyrolysis of CH_3OH was negligible before the photolysis laser arrived), we found that fitted rate coefficients k_1 increased by $< 20\%$, indicating that the effect of $\sim 10\%$ decrease in $[\text{CH}_3\text{OH}]$ during the first period was smaller than the effect due to secondary reactions. In contrast, we found that k_1 decreased by $< 15\%$ for temperatures above 1700 K because 20–40 % of CH_3OH dissociated in the first period.

Values of k_1 at various temperatures are compared with previous reports in Figs. 1 and 3. Our rate coefficients correlate well with data of KSTKM⁵ and GJ⁶ in the overlapped range of temperatures. Our work extends the temperature range of study from 1006 K to 1777 K. Fitting our results to an Arrhenius equation yields

$$k_1 = (2.29 \pm 0.18) \times 10^{-10} \exp [-(4210 \pm 100)/T] \text{ cm}^3 \text{ molecule}^{-1} \text{ s}^{-1} \quad (13)$$

for $835 < T/\text{K} < 1777$, in which listed errors represent one standard deviation in fitting, unless otherwise noted. Observed value of $E_a/R = 4210$ K is much greater than values $E_a/R = 2530\text{--}2750$ K reported previously from measurements below 1000 K,^{5, 6} indicating clearly the non-Arrhenius temperature dependence with an upward curvature. Fitting our data combined with previous results of KTSKM⁵ yields the expression

$$k_1 = (2.74 \pm 0.07) \times 10^{-18} T^{2.25 \pm 0.13} \exp [-(1500 \pm 90)/T] \text{ cm}^3 \text{ molecule}^{-1} \text{ s}^{-1} \quad (14)$$

for $298 \leq T/\text{K} \leq 1777$.

B. Potential energy surfaces and reaction mechanism

Geometries of the molecular reactant (CH_3OH), transition states (TS1, TS2, and TS3), and

products (OH, HO₂, CH₃, CH₂OH, and CH₃O) optimized at the B3LYP/6-311+G(3df, 2p) level are shown in Fig. 4. The potential energy diagram obtained by the CCSD(T)/6-311+G(3df, 2p) single point calculations based on the optimized geometries at the B3LYP/6-311+G(3df, 2p) level is presented in Fig. 5. Total energies of the reactants and relative energies of the transition states and products are listed in Table IV and vibrational frequencies and moments of inertia of all species are summarized in Table V.

The oxygen atom may attack CH₃OH at one of the H atoms of the methyl group (reaction 1a), the H atom of the hydroxyl group (reaction 1b), or the O atom of the hydroxyl group (reaction 1c). As shown in Fig. 5, reaction (1a) proceeds via TS1 with a barrier of 6.3 kcal mol⁻¹ and forms CH₂OH and OH with energy -5.5 kcal mol⁻¹ relative to that of the reactants. Reaction (1b) proceeds via TS2 with a barrier of 10.6 kcal mol⁻¹ and forms CH₃O and OH with energy 2.4 kcal mol⁻¹ above that of the reactants. Reaction (1c) proceeds via TS3 with a barrier of 52.7 kcal mol⁻¹, giving CH₃ and HO₂ with energy 28.1 kcal mol⁻¹ above that of the reactants; the contribution of this channel to the rate coefficient is hence negligible in the temperature range of our study. The predicted enthalpies of reaction for the three branching reactions are compared with experimental values in Table IV. The agreement between theory and experiment is satisfactory.

As shown in Fig. 4, the reacting atoms O, H, and C in TS1 are almost linear with $\angle\text{OHC} = 177^\circ$; the length of the breaking C-H bond increases by 0.12 Å from that of CH₃OH. The imaginary vibrational wave number of TS1 is 426i cm⁻¹. For TS2, $\angle\text{OHO} = 161^\circ$ and the C-H bond length increases by 0.15 Å from that of CH₃OH. The imaginary vibrational wave number of TS2 is 1313i cm⁻¹. The significant difference between the two imaginary frequencies may be conceived by comparing the lengths of the forming O-H and the breaking C-H bonds in TS1 and TS2, as illustrated in Fig. 4. For TS3, the O-O bond length is 1.574 Å and the C-O bond is 1.987 Å; both are longer than those of HOO and CH₃OH. The imaginary vibrational wave number of TS3 is 942i cm⁻¹.

C. Calculation and comparison of rate coefficients

Rate coefficients of reactions (1a) and (1b) calculated with TST, CVT, CVT/ZCT, and

CVT/SCT methods in the temperature range 300 to 3000 K are presented in Fig. 6. As shown in panels A and B of Fig. 6, rate coefficients of reactions (1a) and (1b) predicted with TST are similar to those predicted with CVT because of their moderately high barriers. The rate coefficients predicted with CVT/ZCT are smaller than those predicted with CVT/SCT. At 300 K, rate coefficients of reactions (1a) and (1b) predicted with CVT/SCT are 24 and 10500 times that predicted with CVT, respectively.

The branching ratio of channels (1a) and (1b) predicted with the CVT/SCT method for 300–3000 K are plotted in Fig. 6C. Reaction (1a) is the major channel at low temperatures; its branching ratio decreases from 0.87 at 300 K to 0.50 at 1700 K. Above 1700 K, reaction (1b) becomes the major channel; its branching ratio increases from 0.50 at 1700 K to 0.62 at 3000 K.

In order to compare predicted rate coefficients with experimental data quantitatively, we fit rate coefficients predicted with CVT/SCT in the temperature range 300–1000 K to the Arrhenius form to yield

$$k_{1a}(T) = 1.77 \times 10^{-11} \exp[-(2298/T)] \text{ cm}^3 \text{ molecule}^{-1} \text{ s}^{-1} \quad (15)$$

$$k_{1b}(T) = 1.50 \times 10^{-11} \exp[-(2845/T)] \text{ cm}^3 \text{ molecule}^{-1} \text{ s}^{-1} \quad (16)$$

At higher temperatures, rate coefficients increase more rapidly with temperature. We fit rate coefficients predicted with CVT/SCT in the temperature range 300–3000 K with a three-parameters function to yield

$$k_{1a}(T) = 8.80 \times 10^{-20} T^{2.61} \exp[-(941/T)] \text{ cm}^3 \text{ molecule}^{-1} \text{ s}^{-1} \quad (17)$$

$$k_{1b}(T) = 4.15 \times 10^{-23} T^{3.64} \exp[-(974/T)] \text{ cm}^3 \text{ molecule}^{-1} \text{ s}^{-1} \quad (18)$$

Predicted total rate coefficients may be expressed with the three-parameter equation

$$k_1(T) = 1.93 \times 10^{-21} T^{3.20} \exp[-(763/T)] \text{ cm}^3 \text{ molecule}^{-1} \text{ s}^{-1} \quad (19)$$

The total rate coefficients predicted with CVT/SCT in the temperature range 300–3000 K are plotted in Fig. 3 to compare with experimental data of KTSKM,⁵ GJ,⁶ FSPI,⁷ and this work. In general, rate coefficients predicted with CVT/SCT is in satisfactory agreement with experimental value reported previously, indicating that the SCT method treats tunneling effects adequately. At low temperatures, predicted rate coefficients are slightly greater than experimental values, but within expected uncertainties of calculation and experiments. At

high temperatures, predicted rate coefficients fit satisfactorily with experimental data of this work and of KTSKM⁵ and GJ.⁶

Our experimental data are about 20 % smaller than theoretically predicted rate coefficients, but the deviations are within expected uncertainties. The equation reported by Herron²⁶

$$k_1(T) = 3.99 \times 10^{-19} T^{2.50} \exp [-(1550/T)] \text{ cm}^3 \text{ molecule}^{-1} \text{ s}^{-1} \quad (20)$$

is in satisfactory agreement with our experimental results in the overlapping temperature range 1000–1777 K. The equation reported by Tsang¹⁰

$$k_1(T) = 6.44 \times 10^{-19} T^{2.50} \exp [-(1550/T)] \text{ cm}^3 \text{ molecule}^{-1} \text{ s}^{-1} \quad (2)$$

is slightly greater than our experimental results but appears to fit well with calculated rate coefficients at high temperatures, as illustrated in Fig. 3.

V. CONCLUSION

Total rate coefficients of the reaction $\text{O}(^3\text{P}) + \text{CH}_3\text{OH}$ in the temperature range 835–1777 K were determined using a diaphragmless shock tube with atomic resonance absorption detection of O atoms. Our results extended the upper limit of the temperature range of study from 1006 to 1777 K and clearly indicate a non-Arrhenius behavior of the rate coefficient. Rate coefficients obtained in this work correlate well with those determined previously by Keil *et al.*⁵; they were combined to yield the temperature dependence as $k_1 = (2.74 \pm 0.07) \times 10^{-18} T^{2.25 \pm 0.13} \exp [-(1500 \pm 90)/T] \text{ cm}^3 \text{ molecule}^{-1} \text{ s}^{-1}$ for $298 \leq T/\text{K} \leq 1777$. Theoretical calculations at the CCSD(T)/6-311+G(3df, 2p)//B3LYP/6-311+G(3df, 2p) level predict transition states and barriers for various channels. Rate coefficients predicted with CVT/SCT show that branching ratios of two accessible reaction channels to form $\text{CH}_2\text{OH} + \text{OH}$ (1a) and $\text{CH}_3\text{O} + \text{OH}$ (1b) varies with temperature. At 300 K, reaction (1a) dominates, whereas above 1700 K, reaction (1b) becomes more important. Predicted total rate coefficients are in satisfactory agreement with our experimental data at high temperature (835–1777 K) and those reported by Keil *et al.*⁵ at 298–998 K.

ACKNOWLEDGMENT

YPL thank the National Science Council of Taiwan (grant no. NSC93-2119-M-009-002) for

support. MCL, SCX, and ZFX thank the support from the Basic Energy Science, Department of Energy, under Contract DE-FG02-97-ER14784, and Cherry L. Emerson Center for Scientific Computation of Emory University for the use of its resources, which are in part supported by a National Science Foundation Grant (CHE-0079627) and an IBM Shared University Research Award. MCL also acknowledges the support from the National Science Council of Taiwan for a Distinguished Visiting Professorship at the National Chiao Tung University in Hsinchu, Taiwan. SCX also thank the support from Cherry L. Emerson Center for Scientific Computation of Emory University for a Cherry L. Emerson Visiting Fellowship.

Table I. Summary of reported experimental rate coefficients using various methods

Temperature / K	Pressure (gas) / Torr	k (~298 K) / 10^{-15} , ^a	A / 10^{-12} , ^a	E_a/R / K	Method ^b	Reference
347–506			0.85	1560	DF/PCA	Avramenko <i>et al.</i> (AKK) ⁸
273–438	1.48–2.41 (O ₂ , He)	51.5±5.8	2.82±1.10	1147±101	DF/ESR	LeFevre <i>et al.</i> (LMT) ²
300–830		232	7.11	1020	DF/ESR	Basevich <i>et al.</i> (BKF) ³
301–451	1.00–1.76 (N ₂ , NO)	13.6±0.83	2.41±0.01	1540±144	DF/CL & MS	Owens & Roscoe (OR) ⁴
298	9.25 (Ar)	0.0598			FP/RF	Lalo & Vermeil (LV) ⁹
298–998	2.15–4.41 (O ₂ , He)	5.82±0.54	27.0±5.0	2530±80	DF/RF	Keil <i>et al.</i> (KTSKM) ⁵
329–527	50–400 (Ar), 100–200 (Ar:N ₂ =9:1)				FP/RF	
300–1006			57.0±19.0	2750±150	DF/TOF	Grotheer & Just (GJ) ⁶
297–544	27.2–45.9 (NO, NO ₂)	8.28±0.623	16.3±4.5	2267±111	PM/CL	Failes <i>et al.</i> (FSPI) ⁷
835–1777	1086–1953 (Ar)		229±18 ^c	4210±100 ^c	ST/ABS	this work ^c

^a in units of $\text{cm}^3 \text{ molecule}^{-1} \text{ s}^{-1}$. ^b DF: discharge flow; FP: flash photolysis; PM: phase modulation; ST: shock tube; PCA: product collection and analysis; ESR: electron spin resonance; CL: chemiluminescence; MS: mass spectrometry; RF: resonance fluorescence; TOF: time-of-flight mass; ABS: absorption. ^c $k(T) = (2.74 \pm 0.07) \times 10^{-18} T^{2.25 \pm 0.13} \exp[-(1500 \pm 90)/T] \text{ cm}^3 \text{ molecule}^{-1} \text{ s}^{-1}$ for a combined fit of data from KTSKM and this work

Table II. Reaction models employed to derive rate coefficients of O + CH₃OH

No..	Reaction	Rate expression	Ref.
1a	O + CH ₃ OH → OH + CH ₂ OH	fitted	
1b	O + CH ₃ OH → OH + CH ₃ O	k_{1b}/k_{1a} calculated from theory	
8a	CH ₃ OH (+ M) → CH ₃ + OH (+ M)	$k : 1.9 \times 10^{16} \exp [-(46140/T)]$ $k_0 : 4.9 \times 10^{20} T^{-7.35} \exp [-(48017/T)]$	10 ^{a, b}
8b	CH ₃ OH (+ M) → CH ₂ OH + H (+ M)	$k : 2.96 \times 10^{16} T^{-0.08} \exp [-(49768/T)]$ $k_0 : 3.89 \times 10^{16} T^{-6.33} \exp [-(51860/T)]$	10 ^{a, c}
9	CH ₂ OH + O → H ₂ CO + OH	7.0×10^{-11}	10
10	CH ₃ + O → H ₂ CO + H	1.41×10^{-10}	27
11a	O + SO → S + O ₂	$3.0 \times 10^{-11} \exp [-(6980/T)]$	28
11b	O + SO (+ M) → SO ₂ (+ M)	$3.3 \times 10^{-26} T^{-1.84}$	29
12a	O + SO ₂ (+ M) → SO ₃ (+ M)	$1.21 \times 10^{-33} \exp (3136/T)$	30
12b	O + SO ₂ → O ₂ + SO	$8.3 \times 10^{-12} \exp [-(9800/T)]$	31
21	SO (+ M) → S + O (+ M)	$6.61 \times 10^{-10} \exp (-53885/T)$	32
22	S + O ₂ → SO + O	$9.02 \times 10^{-19} T^{2.11} \exp (730/T)$	33
23	O + SO ₃ → O ₂ + SO ₂	$2.19 \times 10^{-12} \exp (-3070/T)$	30
24	O + O (+ M) → O ₂ (+ M)	$5.21 \times 10^{-35} \exp (900/T)$	34
25	CH ₃ + O ₂ → CH ₃ O + O	$4.9 \times 10^{-11} \exp (-15340/T)$	35
26a	CH ₃ + CH ₃ (+ M) → C ₂ H ₆ (+ M)	$k : 1.5 \times 10^{-7} T^{-1.18} \exp [-(329/T)]$ $k_0 : 8.77 \times 10^{-7} T^{-7.03} \exp [-(1389/T)]$	36 ^{a, d}
26b	CH ₃ + CH ₃ → C ₂ H ₅ + H	$5.25 \times 10^{-11} \exp (-7384/T)$	37
27	CH ₃ + H (+ M) → CH ₄ (+ M)	$k : 2.31 \times 10^{-8} T^{-0.534} \exp [-(270/T)]$ $k_0 : 7.23 \times 10^{-15} T^{-4.76} \exp [-(1227/T)]$	38 ^{a, e}
28a	CH ₃ + OH → CH ₂ OH + H	3.16×10^{-11}	39
28b	CH ₃ + OH → CH ₃ O + H	$3.32 \times 10^{-8} \exp (-13800/T)$	27
29a	CH ₃ + CH ₃ OH → CH ₄ + CH ₂ OH	$5.29 \times 10^{-23} T^{3.2} \exp (-3609/T)$	10
29b	CH ₃ + CH ₃ OH → CH ₄ + CH ₃ O	$2.39 \times 10^{-23} T^{3.1} \exp (-3490/T)$	10
30a	HCO + O → CO + OH	5×10^{-11}	40
30b	HCO + O → CO ₂ + H	5×10^{-11}	40
31	HCO (+ M) → H + CO (+ M)	$1.15 \times 10^{-6} T^{-1} \exp (-8550/T)$	41
32	H ₂ CO + O → HCO + OH	$3.0 \times 10^{-11} \exp [-(1552/T)]$	42
33	H ₂ CO + OH → HCO + H ₂ O	$6.47 \times 10^{-11} \exp [-(705/T)]$	43
34	H ₂ CO + H → HCO + H ₂	$3.62 \times 10^{-16} T^{1.77} \exp [-(1509/T)]$	44
35a	CH ₃ O + O → H ₂ CO + OH	1.0×10^{-11}	34
35b	CH ₃ O + O → CH ₃ + O ₂	$3.55 \times 10^{-11} \exp [-(239/T)]$	45
36	CH ₃ O + OH → H ₂ CO + H ₂ O	3×10^{-11}	34

37	$\text{CH}_3\text{O} + \text{H} \rightarrow \text{H}_2\text{CO} + \text{H}_2$	3×10^{-11}	40
38	$\text{CH}_3\text{O} + \text{CH}_3\text{O} \rightarrow \text{CH}_3\text{OH} + \text{H}_2\text{CO}$	1×10^{-10}	34
39	$\text{CH}_3\text{O} + \text{HCO} \rightarrow \text{CH}_3\text{OH} + \text{CO}$	1.5×10^{-10}	34
40	$\text{CH}_3\text{O} (+ \text{M}) \rightarrow \text{H}_2\text{CO} + \text{H} (+ \text{M})$	$9.04 \times 10^{-11} \exp(-6794/T)$	46
41	$\text{CH}_2\text{OH} + \text{OH} \rightarrow \text{H}_2\text{CO} + \text{H}_2\text{O}$	4×10^{-11}	10
42a	$\text{CH}_2\text{OH} + \text{H} \rightarrow \text{CH}_3 + \text{OH}$	1.6×10^{-10}	10
42b	$\text{CH}_2\text{OH} + \text{H} \rightarrow \text{H}_2\text{CO} + \text{H}_2$	1.66×10^{-11}	47
43	$\text{CH}_2\text{OH} (+ \text{M}) \rightarrow \text{H}_2\text{CO} + \text{H} (+ \text{M})$	$k : 2.8 \times 10^{14} T^{-0.73} \exp[-(16509/T)]$ $k_0 : 9.98 \times 10^9 T^{-5.39} \exp[-(18209/T)]$	$10^{a, f}$
44a	$\text{CH}_2\text{OH} + \text{CH}_2\text{OH} \rightarrow \text{HOCH}_2\text{CH}_2\text{OH}$	1.6×10^{-11}	10
44b	$\text{CH}_2\text{OH} + \text{CH}_2\text{OH} \rightarrow \text{CH}_3\text{OH} + \text{H}_2\text{CO}$	8×10^{-12}	10
45	$\text{CH}_2\text{OH} + \text{CH}_3\text{O} \rightarrow \text{CH}_3\text{OH} + \text{H}_2\text{CO}$	4×10^{-11}	10
46a	$\text{CH}_2\text{OH} + \text{HCO} \rightarrow \text{CH}_3\text{OH} + \text{CO}$	2×10^{-10}	10
46b	$\text{CH}_2\text{OH} + \text{HCO} \rightarrow 2\text{H}_2\text{CO}$	3×10^{-10}	10
47a	$\text{CH}_3\text{OH} + \text{OH} \rightarrow \text{CH}_2\text{OH} + \text{H}_2\text{O}$	$2.39 \times 10^{-18} T^2 \exp(423/T)$	48
47b	$\text{CH}_3\text{OH} + \text{OH} \rightarrow \text{CH}_3\text{O} + \text{H}_2\text{O}$	$1.66 \times 10^{-11} \exp[-(854/T)]$	49
48a	$\text{CH}_3\text{OH} + \text{H} \rightarrow \text{CH}_2\text{OH} + \text{H}_2$	$2.72 \times 10^{-17} T^2 \exp[-(2273/T)]$	48
48b	$\text{CH}_3\text{OH} + \text{H} \rightarrow \text{CH}_3 + \text{H}_2\text{O}$	$3.32 \times 10^{-12} \exp[-(2670/T)]$	50
48c	$\text{CH}_3\text{OH} + \text{H} \rightarrow \text{CH}_3\text{O} + \text{H}_2$	$6.64 \times 10^{-11} \exp[-(3067/T)]$	49
49	$\text{CH}_3\text{OH} + \text{CH}_3\text{O} \rightarrow \text{CH}_2\text{OH} + \text{CH}_3\text{OH}$	$5 \times 10^{-13} \exp[-(2050/T)]$	10
50	$\text{OH} + \text{O} \rightarrow \text{H} + \text{O}_2$	$2.3 \times 10^{-11} \exp(110/T)$	51
51	$\text{O} + \text{H}_2\text{O} \rightarrow 2\text{OH}$	$9.21 \times 10^{-11} \exp[-(9611/T)]$	52

^a k_0 and k refer to low- and high-pressure limits, respectively. The F_c parameters in the Troe equation are listed separately. Unless otherwise noted, all species are assumed to have a third body efficiency of 1.0.

^b $F_c = (1-0.414) \exp[-(T/279)] + 0.414 \exp[-(T/5459)]$.

^c $F_c = (1-0.773) \exp[-(T/693)] + 0.773 \exp[-(T/5333)]$.

^d $F_c = (1-0.619) \exp[-(T/73.2)] + 0.619 \exp[-(T/1180)]$. Enhanced third body coefficient (relative to N_2): $\eta_{\text{Ar}} = 0.7$.

^e $F_c = (1-0.783) \exp[-(T/74)] + 0.783 \exp[-(T/2941)] + \exp[-(6964/T)]$. Enhanced third body coefficient (relative to N_2): $\eta_{\text{Ar}} = 0.7$.

^f $F_c = (1-0.96) \exp[-(T/67.6)] + 0.96 \exp[-(T/1855)] + \exp[-(7543/T)]$.

Table III. Experimental conditions and rate coefficients k_1 for the reaction $O + CH_3OH^a$

P_1 /Torr	P_4 /Torr	M_s	T_5 /K	[SO ₂] /10 ¹⁵	[O] /10 ¹³	[CH ₃ OH] /10 ¹⁴	k_1 /10 ⁻¹²	k_1'/k_1
SO ₂ (302 ppm) + CH ₃ OH (102 ppm), 193 nm								
60.1	2000	2.26	1279	2.99	3.90	10.05	8.43±0.18	1.12
51.1	2000	2.37	1393	2.68	3.46	9.01	12.20±0.26	1.09
45.4	2000	2.46	1485	2.47	2.99	8.30	14.02±0.38	1.09
35.3	2000	2.60	1646	2.03	2.27	6.81	15.78±0.86	2.05
31.1	2000	2.65	1713	1.82	2.28	6.12	18.95±1.40	2.30
30.1	2000	2.70	1766	1.79	2.07	6.01	23.96±2.25	2.12
SO ₂ (500 ppm) + CH ₃ OH (101 ppm), 193 nm								
79.1	2000	2.12	1138	6.01	9.04	12.13	5.52±0.11	1.00
65.1	2000	2.22	1234	5.22	9.28	10.54	8.96±0.15	0.98
50.0	2000	2.38	1404	4.34	7.01	8.77	11.05±0.20	1.09
45.1	2000	2.44	1468	4.02	6.28	8.11	14.14±0.26	0.98
36.0	2000	2.59	1638	3.40	4.55	6.86	16.19±0.55	1.34
35.1	2000	2.59	1640	3.32	5.00	6.70	19.47±0.55	1.64
30.0	2000	2.71	1777	2.95	3.29	5.95	25.55±1.69	2.05
SO ₂ (208 ppm) + CH ₃ OH (151 ppm), 193 nm								
91.3	2000	2.05	1075	2.77	4.21	20.06	5.07±0.11	1.06
80.1	2000	2.07	1092	2.45	3.70	17.80	4.88±0.15	0.98
80.4	2000	2.11	1128	2.52	3.58	18.28	5.47±0.13	1.12
60.3	1800	2.17	1188	1.96	2.62	14.21	6.78±0.26	1.04
70.2	2000	2.20	1212	2.31	3.33	16.78	7.60±0.18	1.05
SO ₂ (300 ppm) + CH ₃ OH (200 ppm), 193 nm								
121.0	2000	1.93	965	4.88	8.50	32.50	3.53±0.08	1.24
80.0	2000	2.13	1145	3.67	5.87	24.44	5.61±0.09	1.27
65.0	2000	2.23	1246	3.15	5.23	21.01	8.17±0.16	0.99
51.2	2000	2.35	1372	2.64	3.94	17.57	8.69±0.17	1.10

40.2	2000	2.51	1550	2.22	3.46	14.78	14.42±0.48	1.39
35.0	2000	2.60	1649	1.99	2.79	13.29	16.60±0.90	1.61
SO ₂ (100 ppm) + CH ₃ OH (300 ppm), 193 nm								
190.2	2000	1.78	835	2.28	3.95	67.95	1.60±0.09	1.31
140.2	2000	1.85	893	1.78	5.56	53.11	2.19±0.05	1.33
113.9	2000	1.96	991	1.58	3.61	47.00	3.03±0.10	1.07
111.1	2000	1.97	995	1.54	3.56	46.01	3.26±0.08	1.05
80.5	2000	2.12	1139	1.23	3.30	36.84	4.94±0.11	0.94
60.0	2000	2.28	1295	1.00	2.75	29.89	8.25±0.20	1.14
50.8	2000	2.42	1446	0.91	1.79	27.03	11.89±0.57	1.24
40.1	2000	2.53	1566	0.75	1.50	22.29	16.38±0.91	1.08
SO ₂ (101 ppm) + CH ₃ OH (500 ppm), 193 nm								
160.1	2000	1.80	849	1.96	4.35	96.51	1.67±0.07	0.98
120.1	2000	1.93	963	1.63	4.66	80.51	3.08±0.07	1.23
100.0	2000	2.02	1039	1.44	3.31	71.17	3.32±0.09	1.06
81.4	2000	2.10	1122	1.24	3.20	61.29	4.66±0.12	1.19
SO ₂ (900 ppm) + CH ₃ OH (136 ppm), 248 nm								
60.2	2000	2.27	1284	8.93	2.71	13.53	7.73±0.36	1.28
50.0	2000	2.30	1315	7.53	1.97	11.40	9.30±0.45	1.13
50.3	2000	2.37	1393	7.84	2.91	11.88	9.54±0.35	1.21
45.3	2000	2.43	1455	7.24	2.08	10.97	10.37±0.64	1.25
41.0	2000	2.48	1513	6.70	2.76	10.14	12.18±0.59	1.24
35.3	2000	2.59	1641	6.02	2.83	9.12	18.11±1.41	1.82
30.3	2000	2.70	1766	5.36	3.18	8.11	23.87±3.83	2.40
30.3	2000	2.71	1775	5.37	2.10	8.13	27.15±3.97	1.63

^a P_1 : pressure of reactant gas mixture; P_4 : pressure of driver gas; M_s : Mach number; T_5 : temperature of reaction. Concentrations are in units of molecule cm^{-3} ; k_1 in $\text{cm}^3 \text{ molecule}^{-1} \text{ s}^{-1}$ are fitted with kinetic modeling and k_1' are derived from pseudo-first-order decays; see text.

Table IV. Total and relative energies^a of reactants, transition states, and products of the reaction O + CH₃OH

Species or reactions	ZPE	B3LYP/ 6-311+G(3df, 2p)	CCSD(T) ^b / 6-311+G(3df, 2p)	$\Delta H_{\text{expt}}^{\text{c}}$
O + CH ₃ OH	0.0511	-190.864006	-190.4686391	
TS1	-2.3	-1.2	6.3	
TS2	-4.7	3.4	10.6	
TS3	-2.4	44.7	52.7	
CH ₂ OH + OH	-3.5	-7.7	-5.5	-6.8±0.8
CH ₃ O + OH	-4.1	-0.5	2.4	1.2±1.1
HO ₂ + CH ₃	-4.5	24.1	28.1	26.3±0.9

^aTotal energies are in a.u. and relative energies are in kcal mol⁻¹.

^bBased on optimized geometries calculated at B3LYP/6-311+G(3df, 2p).

^cAt 0 K, ΔH_f (in kcal mol⁻¹) are as follows: O, 58.98 (Ref. 53); CH₃OH, 45.43 (Ref. 54); OH, 8.85±0.07 (Ref. 55); HO₂, 4.0±0.8 (Ref. 56); CH₃, 35.86±0.07 (Ref. 57); CH₂OH, -2.1±0.7 (Ref. 58); CH₃O, 5.9±1.0 (Ref. 59).

Table V. Vibrational wave numbers and moments of inertia I_i for the reactants, transition states, and products of the reaction $O + CH_3OH$ calculated with B3LYP/6-311+G(3df, 2p)

Species	I_i (a.u.)	Vibrational wave numbers (cm^{-1})
OH	0.0, 3.2, 3.2	3722
HO ₂	2.9, 53.2, 56.1	1171, 1443, 3613
CH ₃	6.3, 6.3, 12.5	539, 1407, 1407, 3108, 3284, 3284
CH ₂ OH	9.3, 60.2, 68.9	411, 528, 1054, 1204, 1356, 1483, 3130, 3272, 3851
CH ₃ O	11.4, 64.1, 64.5	684, 960, 1108, 1355, 1366, 1513, 2885, 2959, 3002
CH ₃ OH	14.0, 72.9, 75.5	288, 1043, 1077, 1174, 1366, 1481, 1500, 1511, 2991, 3038, 3107, 3856
TS1	51.5, 357.3, 392.3	137, 289, 476, 958, 1068, 1137, 1160, 1312, 1380, 1420, 1491, 3026, 3138, 3834, 426 <i>i</i>
TS2	49.1, 285.7, 323.1	142, 167, 189, 616, 1030, 1129, 1150, 1235, 1427, 1435, 1506, 2985, 3043, 3070, 1313 <i>i</i>
TS3	18.0, 360.8, 366.5	86, 216, 257, 427, 607, 669, 983, 1203, 1422, 1434, 3102, 3258, 3274, 3784, 942 <i>i</i>

Caption of Figures

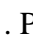
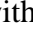


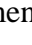
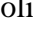
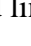
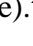
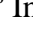
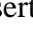
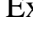
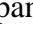
- FIG. 1. Arrhenius plots of k_1 for the reaction $O + CH_3OH$. Our data are shown as symbols . Previous results are shown as lines of various types drawn for the temperature range of study. A combination of first character of each author's last name is used to indicate previous reports, as listed in Table I.
- FIG. 2. A typical temporal profile of $[O]$ observed after irradiation of a sample containing SO_2 (300 ppm) and CH_3OH (200 ppm) in Ar. $T = 1372$ K and total density = 8.79×10^{18} molecule cm^{-3} . The thick solid line represents fitted results using the model described in text.
- FIG. 3. Comparison of total rate coefficient k_1 predicted with theoretical calculations (CVT/SCT, dashed line) with experimental results of this work () , KTSKM ()⁵, GJ ()⁶ and FSPI ()⁷ and recommendation from Tsang (dotted line)¹⁰ and Herron (solid line).²⁶ Insert: Expanded view of our experimental and calculation results.  : $SO_2(302 \text{ ppm}) + CH_3OH(102 \text{ ppm})$;  : $SO_2(500 \text{ ppm}) + CH_3OH(101 \text{ ppm})$;  : $SO_2(208 \text{ ppm}) + CH_3OH(151 \text{ ppm})$;  : $SO_2(300 \text{ ppm}) + CH_3OH(200 \text{ ppm})$;  : $SO_2(100 \text{ ppm}) + CH_3OH(300 \text{ ppm})$;  : $SO_2(101 \text{ ppm}) + CH_3OH(500 \text{ ppm})$;  : $SO_2(900 \text{ ppm}) + CH_3OH(136 \text{ ppm})$, irradiation at 248 nm. Unless otherwise specified, photolysis wavelength is 193 nm.
- FIG. 4. Geometries of reactant CH_3OH , three transition states (TS1, TS2, TS3) and products OH , HO_2 , CH_3 , CH_2OH , CH_3O of the $O + CH_3OH$ system optimized at the B3LYP/6-311+G(3df, 2p) level. Listed bond lengths are in Å and bond angles are in degree.
- FIG. 5. Potential energy diagram for various channels of the reaction $O + CH_3OH$ based on energies calculated with CCSD(T)/6-311+G(3df, 2p)//B3LYP/6-311+G(3df, 2p). Listed energies are in $kcal \text{ mol}^{-1}$.

FIG. 6. Theoretically predicted rate coefficients for the reaction $\text{O} + \text{CH}_3\text{OH}$ in the temperature range 300 - 3000 K. Solid line: CVT with SCT tunneling correction; dotted line: TST; dashed line: CVT; dot dashed line: CVT with ZCT tunneling correction. (A) k_{1a} , (B) k_{1b} , and (C) branching ratios for reactions (1a) and (1b).

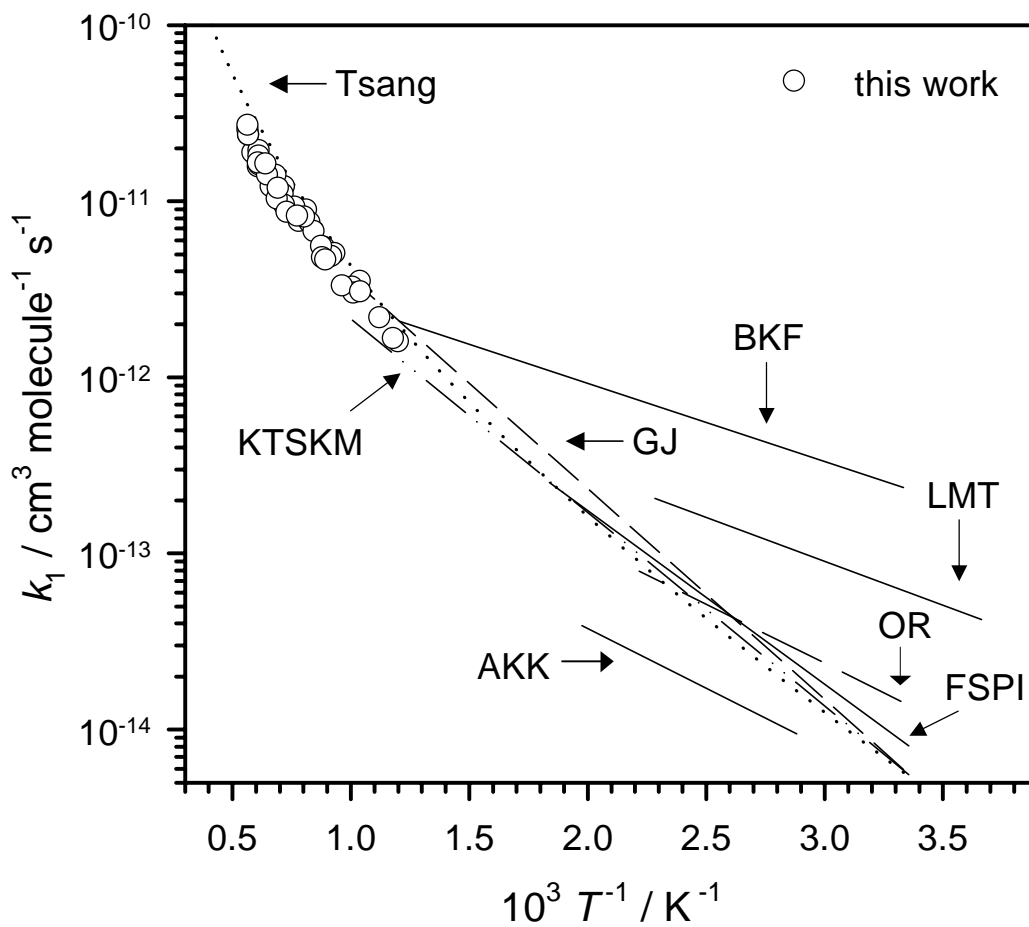


Fig. 1/O+CH₃OH/Lu *et al.*/J. Chem. Phys.

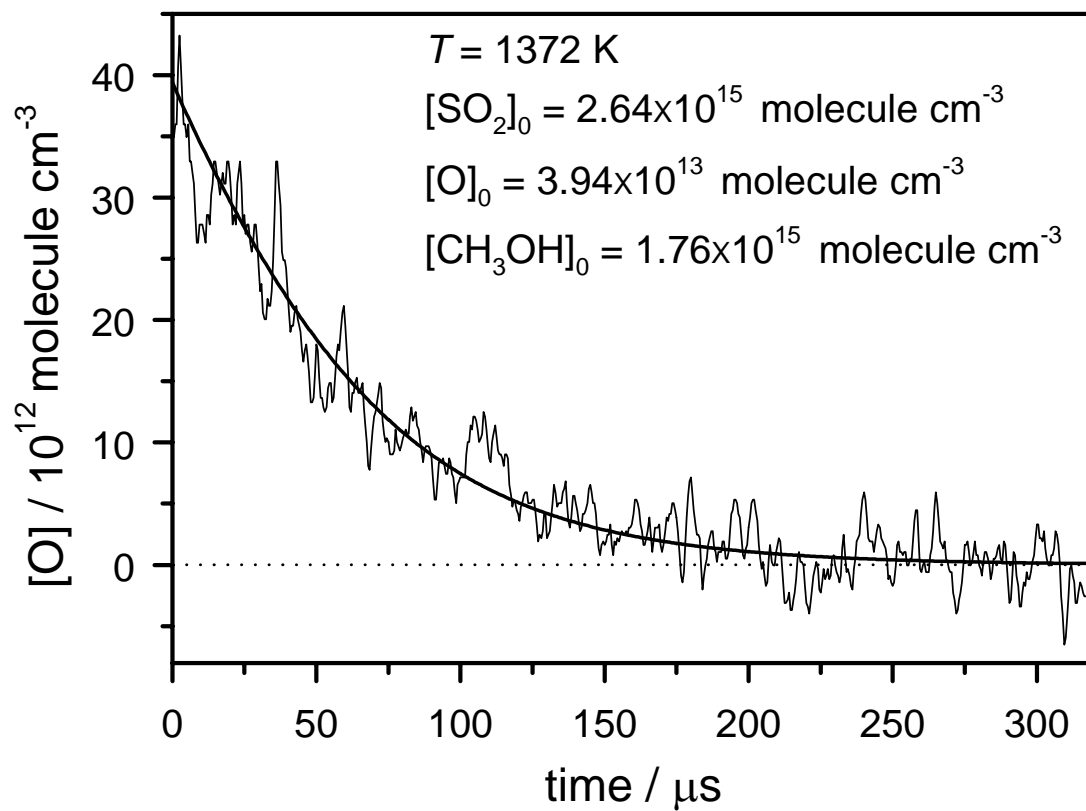


Fig. 2/O+CH₃OH/Lu *et al.*/J. Chem. Phys.

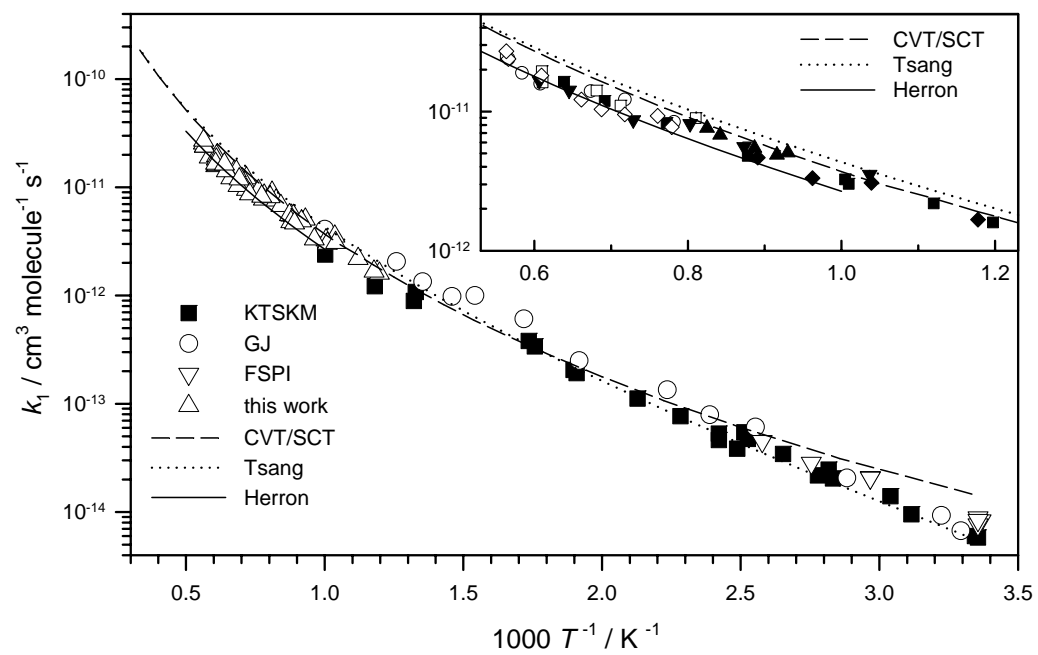


Fig. 3/O+CH₃OH/Lu *et al.*/*J. Chem. Phys.*

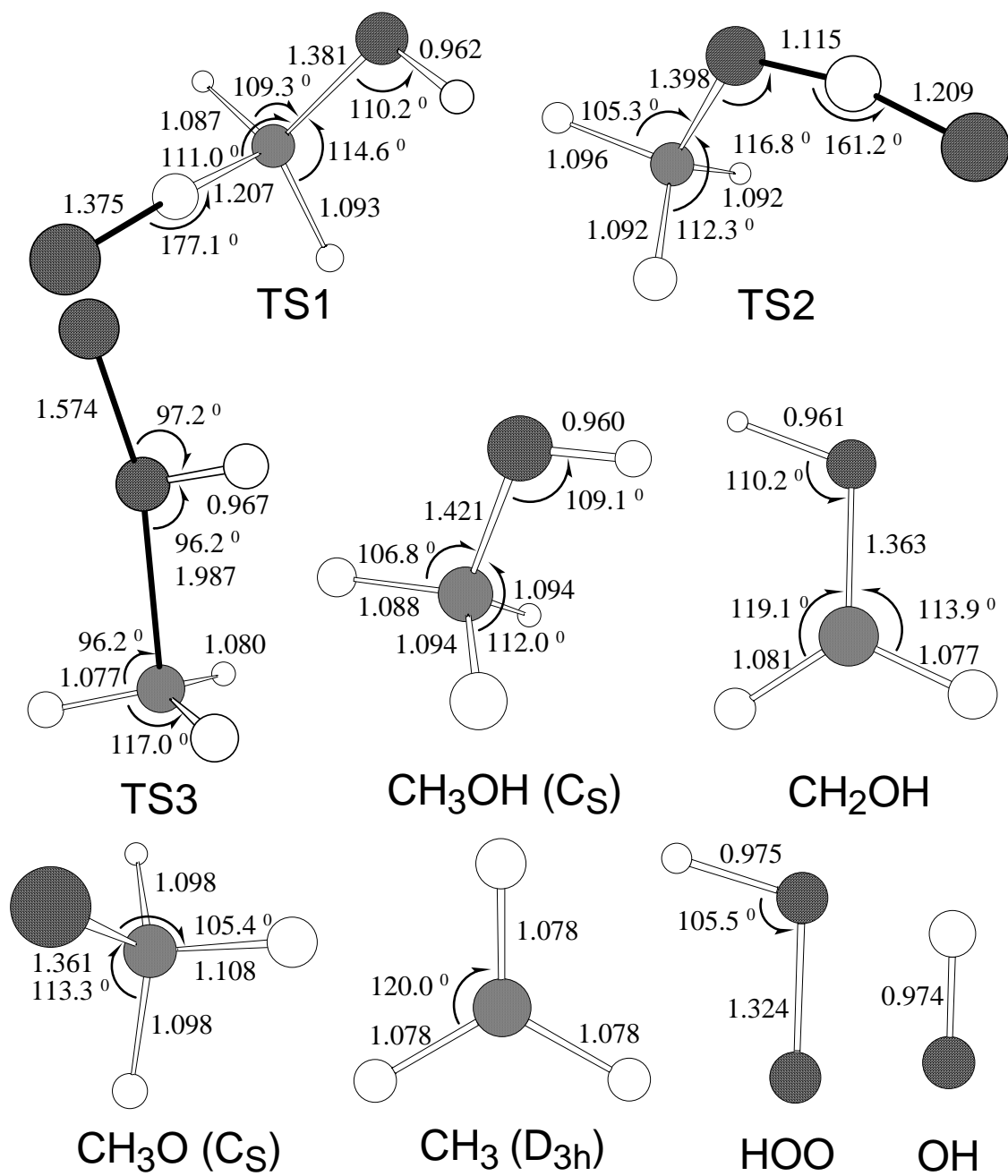


Fig. 4/O+CH₃OH/Lu et al./*J. Chem. Phys.*

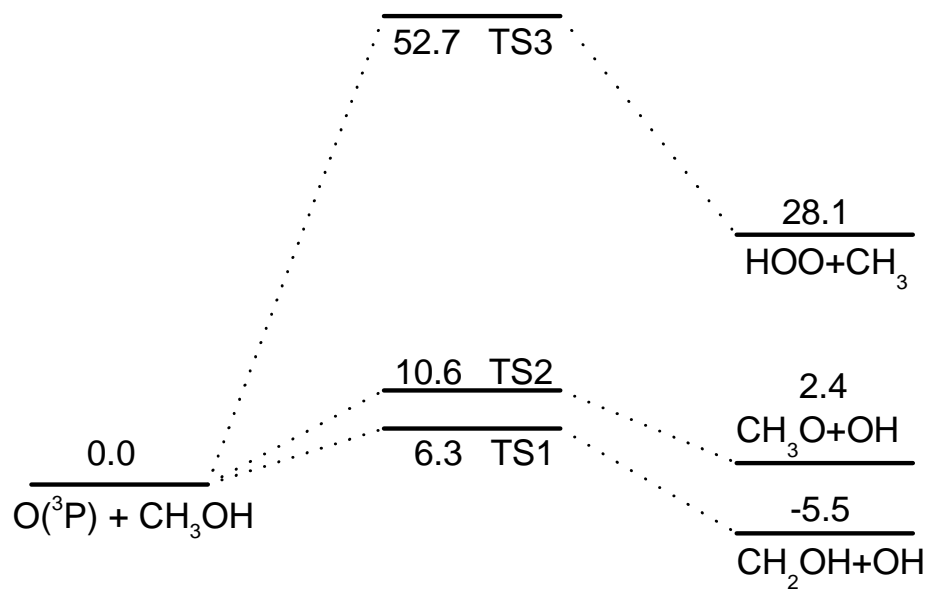


Fig. 5/O+CH₃OH/Lu *et al.*/J. Chem. Phys.

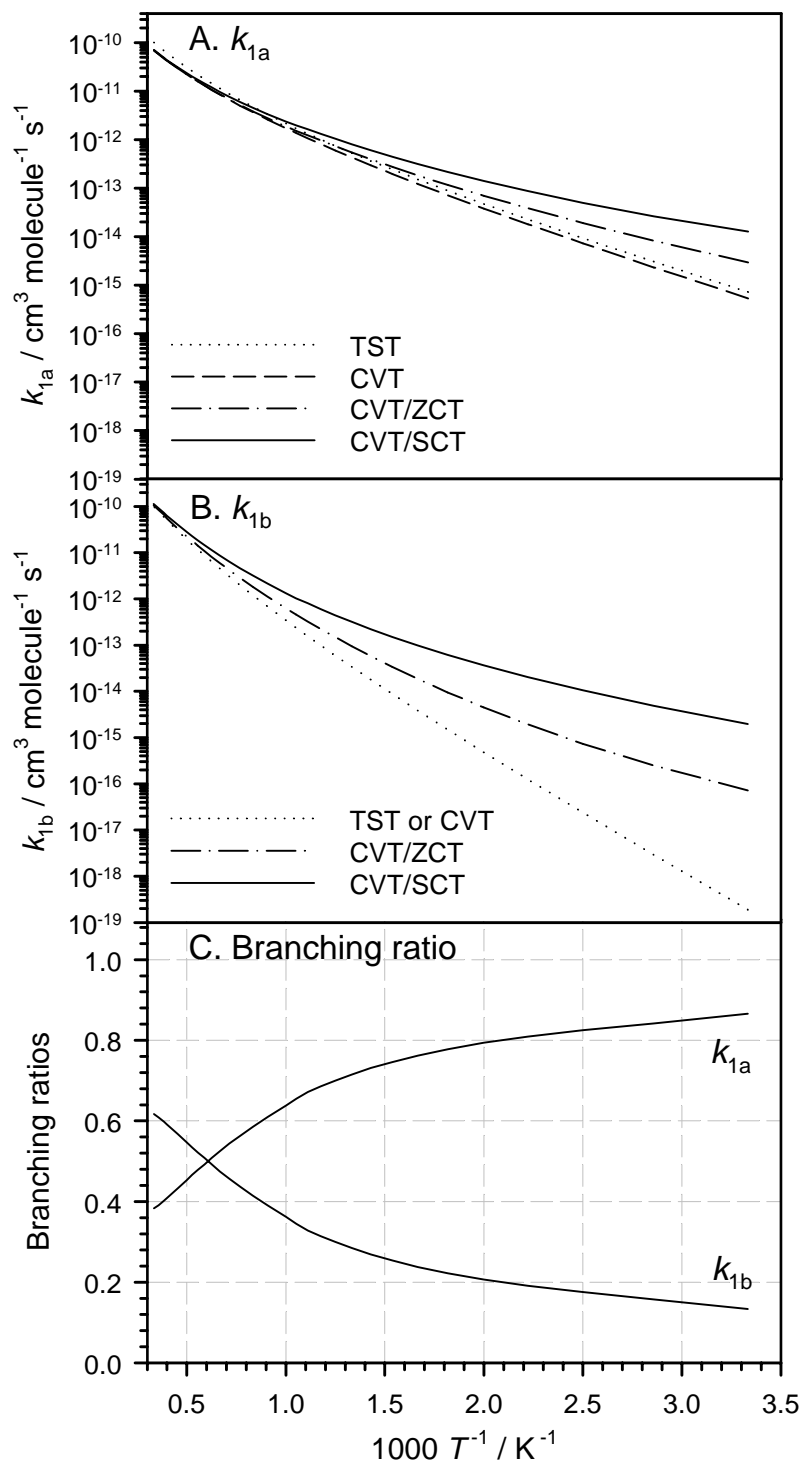


Fig. 6/O+CH₃OH/Lu et al./*J. Chem. Phys.*

References

- ¹ T. J. Held and F. L. Dryer, *Int. J. Chem. Kinet.* **30**, 805 (1998).
- ² H. F. LeFevre, J. F. Meagher, and R. B. Timmons, *Int. J. Chem. Kinet.* **4**, 103 (1972).
- ³ V. Y. Basevich, S. M. Kogarko, and G. A. Furman, *Acad. Sci. USSR, Bull. Div. Chem. Sci.* (Engl. Transl.) 948 (1975); *Izv. Akad. Nauk SSSR, Ser. Khim.* 1035 (1975).
- ⁴ C. M. Owens and J. M. Roscoe, *Can. J. Chem.* **54**, 984 (1976).
- ⁵ D. G. Keil, T. Tanzawa, E. G. Skolnik, R. B. Klemm, and J. V. Michael, *J. Chem. Phys.* **75**, 2693 (1981).
- ⁶ H. H. Grotheer and Th. Just, *Chem. Phys. Lett.* **78**, 71 (1981).
- ⁷ R. L. Failes, D. L. Singleton, G. Paraskevopoulos, and R. S. Iewin, *Int. J. Chem. Kinet.* **14**, 371 (1982).
- ⁸ L. I. Avramenko, R. V. Kolesnikova, and N. L. Kuzentsova, *Iz. Akad. Nauk SSSR Otd. Khim. Nauk* **4**, 599 (1961).
- ⁹ C. Lalo and C. Vermeil, *J. Chim. Phys.* **77**, 131 (1980).
- ¹⁰ W. Tsang, *J. Phys. Chem. Ref. Data* **16**, 471 (1987).
- ¹¹ M. Koshi, M. Yoshimura, K. Fukuda, H. Matsui, K. Saito, M. Watanabe, A. Imamura, and C. Chen, *J. Chem. Phys.* **93**, 8703 (1990).
- ¹² C.-C. Hsiao, Y.-P. Lee, N. S. Wang, J. H. Wang, and M. C. Lin, *J. Phys. Chem. A* **106**, 10231 (2002).
- ¹³ K. Tsuchiya, K. Yokoyama, H. Matsui, M. Oya, and G. Dupre, *J. Phys. Chem.* **98**, 8419 (1994).
- ¹⁴ E. F. Greene and J. P. Toennies, *Chemical Reactions in Shock Waves* (Academic Press: New York, 1964).
- ¹⁵ J. V. Michael, *J. Chem. Phys.* **90**, 189 (1989).
- ¹⁶ J. V. Michael and J. W. Sutherland, *Int. J. Chem. Kinet.* **18**, 409 (1986).

-
- ¹⁷ S. K. Ross, J. W. Sutherland, S.-C. Kuo, and R. B. Klemm, *J. Phys. Chem. A* **101**, 1104 (1997).
- ¹⁸ A. D. Becke, *J. Chem. Phys.* **98**, 5648 (1993), *ibid.* **96**, 2155 (1992), *ibid.* **97**, 9173 (1992).
- ¹⁹ C. Lee, W. Yang, and R. G. Parr, *Phys. Rev.* **37B**, 785 (1988).
- ²⁰ K. Raghavachari, G. J. Trucks, J. A. Pople, and M. Head-Gordon, *Chem. Phys. Lett.* **157**, 479 (1989).
- ²¹ J. C. Corchado, Y.-Y. Chuang, and P. L. Fast *et al.*, POLYRATE Version 8.7, University of Minnesota, Minneapolis, MN, 2001.
- ²² M. J. Frisch, G. W. Trucks, and H. B. Schlegel *et al.*, GAUSSIAN 03 Revision A.7, Gaussian, Inc., Pittsburgh, PA, 2003.
- ²³ S. Satyapal, J. Park, R. Bersohn, and B. Katz, *J. Chem. Phys.* **91**, 6873 (1989).
- ²⁴ B. M. Cheng, M. Bahou, W. C. Chen, C.-H. Yu, Y.-P. Lee, and L. C. Lee, *J. Chem. Phys.* **117**, 1633 (2002).
- ²⁵ FACSIMILE is a computer software for modeling process and chemical reaction kinetics released by AEA technology, Oxfordshire, United Kingdom.
- ²⁶ J. T. Herron, *J. Phys. Chem. Ref. Data* **17**, 967 (1988).
- ²⁷ K. A. Bhaskaran, P. Frank, and Th. Just, *Proc. Int. Symp. Shock Tubes Waves* **12**, 503 (1980).
- ²⁸ C.-W. Lu, Y.-J. Wu, Y.-P. Lee, R. S. Zhu, and M. C. Lin, *J. Phys. Chem. A* **107**, 11020 (2003).
- ²⁹ A. Grillo, R. Reed, and M. W. Slack, *J. Chem. Phys.* **70**, 1634 (1979).
- ³⁰ O. I. Smith, S. Tseregounis, and S-N. Wang, *Int. J. Chem. Kinet.* **14**, 679 (1982).
- ³¹ D. L. Singleton and R. J. Cvetanovic, *J. Phys. Chem. Ref. Data* **17**, 1377 (1988).
- ³² H. J. Plach and J. Troe, *Int. J. Chem. Kinet.* **16**, 1531 (1984).
- ³³ C.-W. Lu, Y.-J. Wu, Y.-P. Lee, R. S. Zhu, and M. C. Lin, *J. Chem. Phys.* **121**, 8271 (2004).

-
- ³⁴ W. Tsang and R. F. Hampson, *J. Phys. Chem. Ref. Data* **15**, 1087 (1986).
- ³⁵ C. L. Yu, C. Wang, and M. Frenklach, *J. Phys. Chem.* **99**, 14377 (1995).
- ³⁶ A. F. Wagner and D. M. Wardlaw, *J. Phys. Chem.* **92**, 2462 (1988).
- ³⁷ K. P. Lim and J. V. Michael, *Symp. Int. Combust. Proc.* **25**, 713 (1994).
- ³⁸ C. T. Bowman, R. K. Hanson, D. F. Davidson, W. C. Gardiner, Jr., V. Lissianski, G. P. Smith, D. M. Golden, M. Frenklach, and M. Goldenberg,
http://www.me.berkeley.edu/gri_mech/index.html
- ³⁹ I. T. Woods and B. S. Haynes, *Symp. Int. Combust. Proc.* **25**, 909 (1994).
- ⁴⁰ D. L. Baulch, C. J. Cobos, R. A. Cox, C. Esser, P. Frank, Th. Just, J. A. Kerr, M. J. Pilling, J. Troe, R. W. Walker, and J. Warnatz, *J. Phys. Chem. Ref. Data* **21**, 411 (1992).
- ⁴¹ Y. Hidaka, T. Taniguchi, T. Kamesawa, H. Masaoka, K. Inami, and H. Kawano, *Int. J. Chem. Kinet.* **25**, 305 (1993).
- ⁴² A. M. Dean, R. L. Johnson, and D. C. Steiner, *Combust. Flame* **37**, 41 (1980).
- ⁴³ J. Vandooren and P. J. Van Tiggelen, *Symp. Int. Combust. Proc.* **16**, 1133 (1977).
- ⁴⁴ Y. Hidaka, T. Taniguchi, H. Tanaka, T. Kamesawa, K. Inami, and H. Kawano, *Combust. Flame* **92**, 365 (1993).
- ⁴⁵ C. J. Cobos and J. Troe, *J. Chem. Phys.* **83**, 1010 (1985).
- ⁴⁶ T. K. Choudhury, Y. He, and W. A. Sanders, *J. Phys. Chem.* **94**, 2394 (1990).
- ⁴⁷ P. H. Gribb, J. E. Dove, and S. Yamazaki, *Combust. Flame* **88**, 169 (1992).
- ⁴⁸ S. C. Li and F. A. Williams, *Symp. Int. Combust. Proc.* **26**, 1017 (1996).
- ⁴⁹ W. C. Gardiner, Jr. in *Combustion Chemistry*, J. Warnatz, ed. (Springer-Verlag, NY, 1984).
- ⁵⁰ Y. Hidaka, T. Oki, and H. Kawano, *J. Phys. Chem.* **93**, 7134 (1989).
- ⁵¹ R. Atkinson, D. L. Baulch, R. A. Cox, R. F. Hampson, Jr., J. A. Kerr, M. J. Rossi, and J. Troe, *J. Phys. Chem. Ref. Data* **26**, 1329 (1997).
- ⁵² J. W. Sutherland, P. M. Patterson, and R. B. Klemm, *Symp. Int. Combust. Proc.* **23**, 51

(1991).

- ⁵³ M. W. Chase, Jr., C. A. Davies, J. R. Downey, Jr., D. J. Frurip, R. A. McDonald, and A. N. Syverud, *J. Phys. Chem. Ref. Data* **14**, Suppl. 1 (1985). See also: M. W. Chase, Jr., *J. Phys. Chem. Ref. Data, Monograph* **9** (1998).
- ⁵⁴ (a) D. D. Wagman, W. H. Evans, V. B. Parker, R. H. Schumm, I. Halow, S. M. Bailey, K. L. Churney, and R. L. Nuttall, *J. Phys. Chem. Ref. Data* **11**, Suppl. 2 (1982). (b) H. M. Rosenstock, K. Draxl, B. W. Steiner, and J. T. Herron, *J. Phys. Chem. Ref. Data* **6**, Suppl. 1 (1977).
- ⁵⁵ B. Ruscic, A. F. Wagner, L. B. Harding, R. L. Asher, D. Feller, D. A. Dixon, K. A. Peterson, Y. Song, X. Qian, C.-Y. Ng, J. Liu, W. Chen, and D. W. Schwenke, *J. Phys. Chem. A* **106**, 2727 (2002).
- ⁵⁶ M. Litorja and B. Rustic, *J. Elec. Spectro. Relat. Pheno.* **97**, 131 (1998).
- ⁵⁷ B. Rustic, M. Litorja, and R. L. Asher, *J. Phys. Chem. A* **103**, 8625 (1999).
- ⁵⁸ B. Rustic and J. Berkowitz, *J. Phys. Chem.* **97**, 11451 (1993).
- ⁵⁹ B. Rustic, E. H. Appelman, and J. Berkowitz, *J. Chem. Phys.* **95**, 7957 (1991).